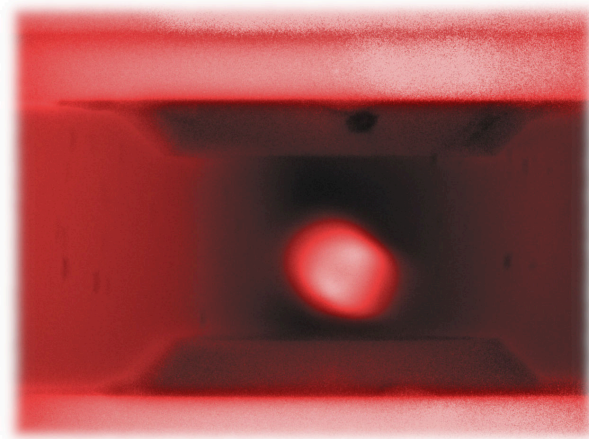


A Novel Fermionic Quantum Gas Microscope: Concept, Design and Construction.



Dissertation
zur Erlangung des Doktorgrades
an der Fakultät für Mathematik, Informatik und Naturwissenschaften
Fachbereich Physik
der Universität Hamburg

vorgelegt von

Phillip Wieburg

Hamburg

2019

Phillip Wieburg: *A Novel Fermionic Quantum Gas Microscope: Concept,
Design and Construction.*

© January 2019

Gutachter/innen der Dissertation:

Prof. Dr. Henning Moritz
Prof. Dr. Klaus Sengstock

Vorsitzender des Fach-Promotionsausschusses Physik:

Prof. Dr. Michael Potthoff

Leiter des Fachbereichs Physik:

Prof. Dr. Wolfgang Hansen

Dekan der Fakultät MIN:

Prof. Dr. Heinrich Graener

Zusammenfassung

In dieser Arbeit wird ein neuer experimenteller Aufbau zur ortsauflösenden Untersuchung von Systemen aus ultrakalten, fermionischen ^{40}K Atomen vorgestellt. Der Aufbau ist darauf ausgelegt, sowohl Versuche mit einzelnen Atomen in optischen Pinzetten als auch solche mit quantenentarteten Ensembles durchzuführen. Um kurze Zykluszeiten zu ermöglichen werden dabei ausschließlich Laserkühlverfahren verwendet. Ziel dieses neuen Aufbaus sind Untersuchungen welche auf ein besseres Verständnis von stark korrelierten fermionischen Vielteilchensystemen hinwirken. Ein herausragendes Beispiel für solche Systeme liegt in Hochtemperatursupraleitern, wie YBCO und ähnlichen keramischen Verbindungen, vor. Für das ungewöhnliche Verhalten dieser Materialien werden allgemein isolierte Ebenen in der Kristallstruktur verantwortlich gemacht, welche aus Kupferoxid gebildet sind. Die Dynamik in diesen zweidimensionalen Gittersystemen kann mittels unterschiedlicher Hubbard-Modelle beschrieben werden und stellt einen attraktiven Untersuchungsgegenstand für Quantensimulationen mit ultrakalten Atomen dar.

Die Kernkomponente unseres neuen Apparates ist die ultrahochvakuumtaugliche Mikroskopobjektiv-Baugruppe, welche aus zwei Objektiven besteht und sich im Inneren der bei 1×10^{-11} mbar betriebenen Vakuumkammer befindet. Jedes dieser Objektive ist auf unendlich korrigiert, besteht aus sechs sphärischen Linsen und besitzt eine numerische Apertur von 0.75. Sie werden sowohl zur Abbildung der Atome als auch zur Erzeugung von optischen Potentialen verwendet. Indem wir die Objektive im Inneren der Vakuumkammer benutzen und die Objektive relativ zueinander perfekt justiert sind, können wir die volle Auflösung mit einem Minimum an Justageaufwand erzielen.

Wir benutzen eine 2D-MOT um einen ^{40}K -Atomstrahl zu erzeugen aus welchem wir 1×10^7 Atome pro Sekunde in eine MOT, welche auf dem D2-Übergang operiert, laden. Anschließend benutzen wir eine blau verstimmete graue Melasse auf dem D1-Übergang um die Atome auf eine Temperatur in der Größenordnung von $10 \mu\text{K}$ zu kühlen, bevor sie mittels eines magnetischen Transportes in das Sichtfeld der Mikroskopobjektive gebracht werden. Dort werden sie, je nach angestrebtem Experiment, in unterschiedliche fernverstimmete, optische Dipolfallen umgeladen. Momentan kann dabei entweder ein optisches Gitter oder eine optische Pinzette verwendet werden. Nach dem Umladen werden die Atome in den Grundzustand des jeweiligen Potentials gekühlt, wobei wir Raman-Seitenbandkühlen verwenden. Für den Fall eines eindimensionalen optischen Gitters konnten wir bislang eine Besetzungswahrscheinlichkeit des Grundzustandes von über 80 % erzielen. Wir haben die Fähigkeit die optische Pinzette mit einem Atom zu beladen und den Nachweis darüber mittels Fluoreszenz auf dem D1-Übergang zu führen. Momentan arbeiten wir darauf hin, Raman-Seitenbandkühlen auch mit einem einzelnen Atom zu realisieren.

Abstract

This thesis describes a new quantum gas microscope working with ultracold fermionic ^{40}K atoms. Using all-optical cooling techniques, the apparatus is designed to perform experiments with individual atoms in optical tweezers or ensembles cooled to quantum degeneracy. The purpose of the experiment is to gain a better understanding of strongly correlated fermionic many-body systems. One outstanding goal is to conduct experiments revealing the underlying microscopic mechanisms in high- T_c superconductors like YBCO and similar materials. Generally, planes of copper oxide are considered to be responsible for the superconductivity in these ceramic materials. The dynamics in the copper oxide planes is governed by Hubbard-type Hamiltonians that are an ideal subject for quantum simulations with ultracold atoms.

The key component of the new apparatus is a microscope objective assembly located inside a vacuum chamber operating at 1×10^{-11} mbar. The assembly consists of two infinity-corrected microscope objectives with a numerical aperture of 0.75, each containing 6 spherical lenses. With these in-vacuo microscope objectives we achieve single-site resolution for both imaging and imprinting with a minimum of optical alignment.

The experiment uses a 2D-MOT atom source to collect approximately 1×10^7 atoms per second in a MOT on the D2 line. After an intermediate cooling step using a Λ -enhanced grey molasses on the D1 line reaching a temperature on the order of $10 \mu\text{K}$, we magnetically transport the atoms into the field of view of the microscope objectives. Here, the atoms are loaded into far detuned optical dipole traps - optical lattices or a small number of optical tweezers - before cooling them to the motional ground state using Raman sideband cooling. For atoms confined in a one-dimensional lattice, we have achieved ground state fractions above 80%. We are able to load single atoms into an optical tweezer and detect them via D1 fluorescence and are working towards Raman cooling.

Contents

1	Introduction	2
2	Fermi-Hubbard systems and high-T_C superconductivity	4
2.1	Superconductivity, high- T_C and d-wave	5
2.1.1	Phenomenology	5
2.1.2	BCS theory and the gap equation	6
2.1.3	BCS experiments in cold atoms	8
2.1.4	Pairing in unconventional superconductors	9
2.1.4.1	Crystal structure and parametrization	10
2.1.4.2	High- T_c superconductors and Hubbard models	11
2.1.5	The pseudogap	13
2.2	Experimental manifestations of the d-wave order parameter	15
2.3	d-wave physics in plaquette systems	20
2.3.1	Identifying d-wave symmetry	20
2.3.2	Selected plaquette states	23
2.3.3	The gap operator	25
2.3.4	Future plaquette experiments	26
3	The state of the art in quantum gas microscopes	28
3.1	Optical fundamentals	28
3.2	Design aspects of quantum microscopes	30
3.3	Currently operating quantum microscopes	31
4	Our new quantum gas microscope	37
4.1	General experiment design	37
4.1.1	Choice of atomic species	37
4.1.2	Key design features of the apparatus	38
4.1.3	Experimental geometry	38
4.2	Vacuum system	40

4.2.1	Requirements	40
4.2.1.1	Pressure requirements	40
4.2.1.2	Geometrical requirements	41
4.2.1.3	Additional requirements	41
4.2.2	Final design	42
4.2.2.1	2D-MOT chamber	42
4.2.2.2	Main chamber	45
4.2.2.3	Pumps	49
4.2.2.4	Arrangements for in-vacuo devices	51
4.2.3	Manufacturing and commissioning	52
4.2.3.1	Vacuum cleaning procedures	52
4.2.3.2	Pumping and leak testing	53
4.2.3.3	2D-MOT rectangular viewports	53
4.2.3.4	Preparing the main chamber vacuum	54
4.2.3.5	Installing the chamber interior except micro- scope assembly	55
4.2.3.6	Microscope installation	58
4.3	Magnet systems	59
4.3.1	Functional requirements	59
4.3.2	Technical requirements	59
4.3.3	Resulting coil structure	60
4.3.4	Water-cooled high current coils	61
4.3.5	Coil mounting structure	66
4.3.6	High current electronics	68
4.3.7	Predominant eddy currents	69
4.3.8	Additional field coils	70
4.3.9	Permanent magnet 2D-MOT field	70
4.4	High resolution imaging system	72
4.4.1	Optical design of the microscope objectives	72
4.4.2	Measures taken to ensure UHV compatibility	75
4.4.3	Microscope manufacturing	76
4.5	Lasers and optics	78
4.5.1	Laser systems	78
4.5.1.1	D2 laser system	79
4.5.1.2	D1 laser system	81
4.5.1.3	850 nm laser system	86
4.5.1.4	Raman laser system	86

4.5.2	Optical assemblies around the experiment	88
4.5.2.1	2D-MOT optics	88
4.5.2.2	MOT and molasses optics	88
4.5.2.3	Lattice optics	90
4.5.3	Beams passing through the microscope assembly	91
4.5.4	Auxiliary absorption imaging systems	94
5	On the pathway to tweezer-plaquette physics	96
5.1	MOT loading	96
5.2	Grey molasses	101
5.3	Optical pumping	102
5.4	Capturing and transporting atoms magnetically	103
5.5	Loading of lattice and tweezers	105
5.5.1	Alignment of atom traps	105
5.5.2	Loading procedure	108
5.6	Lattice	110
5.6.1	Trap frequencies	111
5.6.2	Lifetimes	113
5.7	Preparations for Raman sideband cooling	114
5.7.1	Microwave spectra	114
5.7.1.1	Microwave generation	114
5.7.1.2	Resolving m_F -spectra	115
5.7.1.3	Rabi oscillations and compensation of magnetic field fluctuations	118
5.7.2	Raman spectra	123
5.8	Atoms in the tweezer	129
6	Conclusions and Outlook	131
	Nomenclature	135
	Bibliography	137

Chapter 1

Introduction

In 1981 R. P. Feynman [1] pointed out that it is very ineffective to compute quantum mechanical problems on classical computers. Instead, he proposed solving them with quantum mechanical methods. The idea is to perform experiments with one easily controllable quantum system in order to understand the properties of different, less controllable, less pure but mathematically equivalent quantum systems. At this time, experimental physics was neither sufficiently advanced to reliably provide well isolated quantum systems like trapped ions or atoms nor capable of coherent manipulation procedures required for initializing the desired quantum state. I will describe how we designed and constructed a novel apparatus for trapping, cooling and manipulating individual fermionic atoms. In the near future, the apparatus will be capable of performing quantum simulations on well-isolated fermionic systems with single-site resolution and single-atom sensitivity. Creating, manipulating and measuring such samples is an endeavor full of problems. Some of them have been solved only recently.

Over the past 40 years, experimental progress in the preparation and manipulation of ultracold atoms paved the way to realizing Feynman's idea. Five Nobel Prizes have been awarded for pioneering techniques and experiments which are directly relevant for our research. Now, the methods are highly developed and enable us to observe the dynamics in many-body quantum systems on a single atom level. This is possible as the length scales of these systems are large enough to employ imaging techniques at optical wavelengths. The dynamics are much slower than in corresponding solid-state systems, so it is easy to follow their time evolution. In addition, we have the freedom to choose tunneling and interaction parameters at will. Quantum simulation is a very general approach and the number of possible applications is almost unlimited. There exist numerous review articles about the current status of the field and its future prospects [2, 3, 4, 5, 6, 7].

For ultracold atom experiments with fermions, a detailed review has been

given by Ketterle and Zwierlein in [8]. In particular with respect to these experiments, there has been very exciting progress recently. In 2015 five groups published their single-site resolved images of fermionic atoms trapped in optical lattices [9, 10, 11, 12, 13]. In contrast to these five quantum gas microscopes, the apparatus described here is specialized to the study of small systems with potentials drawn using optical tweezers to approach the investigation of strongly correlated many-body problems relevant for solid-state systems in a bottom-up approach. We are aiming at understanding the nature of these systems at the level of their smallest building blocks.

The idea of trapping single atoms in optical tweezers and cooling them to the motional ground state by Raman sideband cooling has been pioneered in C. Regal's [14, 15, 16, 17, 18, 19] and M. Lukin's group [20] using rubidium atoms. Recently, the same scheme has been adapted to the bosonic earth-alkaline atom ^{88}Sr with its narrow transitions useful for direct sideband cooling [21, 22]. A common problem of these experiments using light-driven ground-state cooling is that light-assisted collisions usually limit the loading probability to 50 % for each tweezer. For experiments with larger tweezer arrays, this is certainly not adequate. Two possible ways to avoid this problem and reach loading fidelities close to unity rely on "blue shielding" [23, 17, 24] or atom sorting [25, 26].

The apparatus described here is versatile and combines the capabilities of usual quantum gas microscopes with the ability to generate flexible potentials using optical tweezers. Later, we plan to extend the experiment to produce quantum degenerate Fermi gases using optical cooling techniques. So far, this rapid way of achieving quantum degeneracy has only been demonstrated for bosons [27, 28].

This thesis is structured as follows:

In Chapter 2, I will motivate why we decided to build a fermionic tweezer apparatus: I will give a short overview over high- T_c superconductivity and the unresolved problems in understanding the underlying microscopic mechanisms. I will outline how our experiments might help to get a better understanding of this striking and technologically relevant phenomenon.

In Chapter 3, an overview of the state of the art of quantum gas microscopy is presented with a focus on the different ways of achieving sufficiently high resolution for imaging and imprinting of optical potentials. Pros and cons of the different designs are discussed.

In Chapter 4, the design and construction of our quantum gas microscope is presented in detail.

A description of our current experimental sequence as well as characterization measurements are given in Chapter 5.

Finally, in Chapter 6, the current status is summarized followed by an outlook on future experiments.

Chapter 2

Fermi-Hubbard systems and high- T_C superconductivity

One century after its discovery by H.K. Onnes in 1911, superconductivity is not only a striking macroscopic quantum phenomenon and a subject of ongoing scientific research, but also a relevant tool in physics and technology. So far, the most important use of superconductivity is to create static magnetic fields. One application is nuclear magnetic resonance (NMR) [29] and its use in imaging biologic material in health care and life sciences [30, 31]. Among others, particle accelerators [32] and nuclear fusion experiments [33] belong to the most prominent scientific applications of superconducting electromagnets. In particle physics, high sensitivity detectors rely on superconductivity [34]. On the other end of the energy scale, superconducting devices are exploited for precision measurement techniques: Magnetic measurement devices based on SQUIDs (superconducting quantum interference devices) [35, 36, 37] enabled microscopic precision magnetic flux measurements - a very important tool in solid-state physics. All examples listed so far are typically based on conventional superconductors, not high-temperature superconductors. The first technical field in which high-temperature superconductors have led to an industry product is in telecommunications. Here, advanced microwave filters used in cellular phone ground stations use nitrogen cooled superconductors [38]. Superconducting power transmission lines for electric energy supply is one potential application. Today, technical feasibility has been proven for distances up to some hundred meters [39].

There are many good reasons for achieving a better understanding of superconductivity. The key to more technological use lies primarily in pushing the critical temperature T_C to higher values. Due to insufficient understanding of the microscopic mechanisms governing high-temperature superconductivity, this development was - to large extent - based on trial and error. The most striking event in the history of the field since the formulation of the Bardeen-

Cooper-Schrieffer (BCS) theory was the discovery of copper oxide (=cuprate) superconductors in 1986/1987 [40, 41]. These superconductors feature critical temperatures at which the electron pairing required by the BCS theory can no longer be explained as mediated by phonons. It was suspected shortly after the discovery of cuprate high- T_c s that the new - yet unknown - pairing mechanism should manifest in a gap function $\Delta(k)$ with different symmetry than the one known from conventional superconductors - where the gap is a spherically symmetric function in momentum space. By now it is established that the gap in cuprate superconductors has d-wave symmetry instead of s-wave, but other symmetries like p-wave have been considered as well. The nomenclature of the gap symmetries has been adopted from atomic orbitals.

In this chapter, I will summarize some key aspects concerning conventional and high-temperature superconductivity. A brief explanation of the BCS mechanism, the physical meaning of the superconducting gap function and how this gap is governed by the pairing interaction are presented to clarify the terminology. Afterwards, I will give an overview of the current status in the highly controversial topic of understanding the high- T_c pairing mechanism before presenting some beautiful experimental verification of the pairing symmetry obtained in solid-state systems. Wherever necessary, related experiments in the field of ultracold atoms are mentioned. Finally I will motivate how quantum simulators like the one described in Chapters 4 and 5 might contribute to a better microscopic theory.

2.1 Superconductivity, high- T_C and d-wave

For completeness, I begin with a short phenomenological summary of the macroscopic properties before coming to the microscopic theory of superconductivity. I won't give a full description of BCS theory though, but limit myself to understanding the role of the electron pairing mechanism, the superconducting gap and its geometries.

2.1.1 Phenomenology

Superconductors enter a new state of matter when cooled below the critical temperature T_c . Macroscopically, this state is characterized by a vanishing electric resistivity. In addition, magnetic fields are expelled from inside the superconductor. This is called the Meissner-Ochsenfeld-effect.

Above a certain critical value for the applied magnetic field H_c , superconductivity breaks down. For so-called type I superconductors this breakdown happens abruptly and the material is then in its normal state. For type-II superconductors the material remains superconducting for fields $H_c < H < H_{c2}$ where H_{c2} is a second critical field. In this intermediate regime, the magnetic

field can partially enter the superconductor. The Meissner-Ochsenfeld-effect was discovered 22 years after the discovery of the infinite electrical conductivity. It is important that the perfect diamagnetic behavior occurs regardless whether or not the magnetic field was present prior to cooling the superconductor below its critical temperature.

2.1.2 BCS theory and the gap equation

Starting in the late 1940s, the theoretical understanding of the microscopic nature of superconductivity began to evolve. In 1957, Bardeen, Cooper and Schrieffer published their theory of superconductivity [42] that is now known as BCS theory and they received a Nobel prize in 1972. This theory describes superconductivity as a state of Bose-condensed pairs of electrons. In the case that no current is flowing through the superconductor, pairs are predominantly formed by electrons of opposite momentum and spin, such that the total momentum of the pair is zero. “Pairing” means that the state $|k, \uparrow\rangle$ is always occupied if $| -k, \downarrow\rangle$ is occupied. If instead there is a net current flow in the superconductor, the pairs have a non-vanishing total momentum $k_1 + k_2 = q$. As the paired electrons occupy a small region around the Fermi surface, the phase space available is reduced in the case of non-vanishing total momentum. This is illustrated in Fig. 2.1.

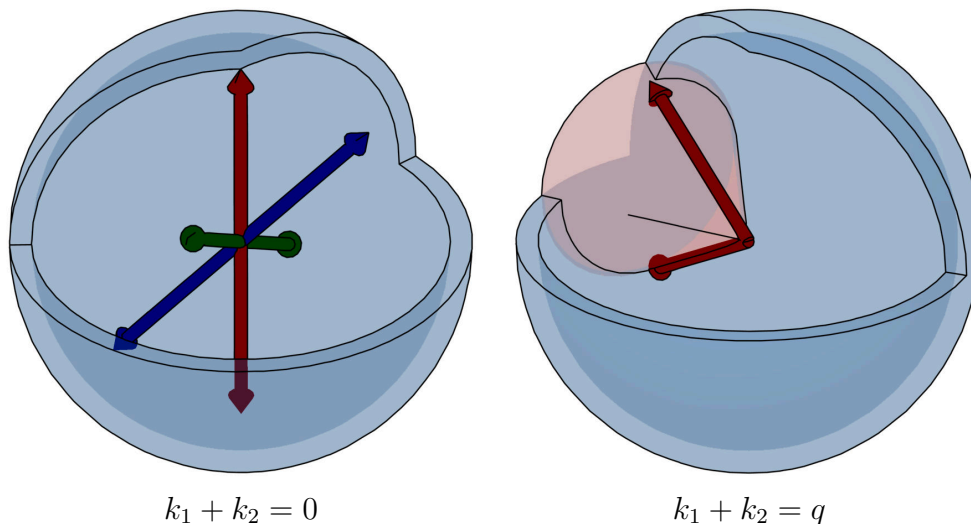


Figure 2.1: Possible Cooper pairs for different total momenta and a spherical Fermi surface. Pair formation is allowed within a finite region from the Fermi surface as indicated by the thickness of the shell. Arrows of same color represent paired electrons. For the case of non-vanishing total momentum, possible pairs are restricted to the overlap of a corresponding cone with the Fermi surface. The available phase-space is reduced.

The usual representation of the BCS state is

$$|\Psi_{BCS}\rangle = \prod_k \left(u_k + v_k c_{k\uparrow}^\dagger c_{-k\downarrow}^\dagger \right) |0\rangle \quad (2.1)$$

which means that for every momentum k there exists a certain amplitude $|v_k|^2$ that the state is occupied by a Cooper pair.

For BCS theory it is not important what exact mechanism leads to pair formation. But to understand why different superconductors exhibit different critical temperatures, the strength and nature of the pairing mechanism is relevant. In the case of conventional superconductivity, the pairing of electrons is mediated by phonons. For high- T_c superconductivity, the critical temperatures are associated with energies well above phonon energies. Nonetheless, it could be experimentally verified shortly after the discovery of these materials that the superconducting phase consists of a condensate of electron pairs [43, 44]. Commonly, pairing in these superconductors is considered to be mediated primarily by charge or spin based physics. Nonetheless, mechanisms where phonons play some assisting role in the pairing process are not generally excluded.

The parameter that characterizes the electron pairing is the so-called “superconducting gap” $\Delta(k)$. It separates the energy spectra of paired and unpaired electrons and can be understood as the binding energy of a Cooper-pair. The nature of the superconducting gap is the key to understanding superconductivity. Experimentally, the superconducting gap manifests itself most obviously as a threshold voltage for superconducting current flow [45].

From theory, one can derive a self-consistent equation that relates the superconducting gap to the pair mediating interaction $V(k, k')$. In the $T \rightarrow 0$ limit, this famous “gap equation” has the simple form

$$\Delta(k) = - \sum_{k'} \frac{1}{2E(k')} V(k, k') \Delta(k') \quad (2.2)$$

with the quasiparticle excitation energy

$$E(k) = \sqrt{(\epsilon_k)^2 + |\Delta(k)|^2}$$

and the single electron energy

$$\epsilon_k = \frac{\hbar^2 k^2}{2m} - \mu$$

For details on the underlying formalism, I can recommend M. Zwierlein’s doctoral thesis [46].

Though the gap equation’s solution is certainly not trivial even in the $T \rightarrow 0$ case, some useful symmetry arguments follow directly from this self-consistency equation:

- If the pairing interaction is momentum-independent and attractive, $V(k, k') = V_0 < 0$, the gap must have the same sign everywhere.
- If the pairing interaction is momentum-independent and repulsive, $V(k, k') = V_0 > 0$, a solution requires that $\Delta(k)$ changes the sign somewhere or that trivially $\Delta(k) = 0$.
- For more sophisticated pairing interactions like the ones that are suspected to lead to high- T_c , the interaction is often peaked around certain momentum values Q , in the sense that for $V(k, k') = V(k - k')$, $|V(Q)|$ is large and these terms dominate the gap equation. In this case, when $V(Q) < (>) 0$, $\Delta(k)$ and $\Delta(k + Q)$ tend to have the same (opposite) signs. This argument follows [47].

As stated above, the density of states involved in pair formation is crucial for the superconducting nature. To illustrate this, let us consider the ‘‘Cooper approximation’’¹, where a constant, positive pairing term is assumed for energies below a certain cutoff energy $\hbar\omega_c$ and vanishing pairing above

$$V(k, k') = \begin{cases} \text{const} & |\epsilon_k|, |\epsilon_{k'}| < \hbar\omega_c \\ 0 & \text{otherwise} \end{cases}$$

The gap loses its k -dependence and the gap equation can be solved analytically by replacing the sum with an integral

$$1 = \frac{1}{2} V_0 \mathcal{N}(0) \int_{-\hbar\omega_c}^{+\hbar\omega_c} \frac{1}{\sqrt{\epsilon^2 + |\Delta|^2}} d\epsilon$$

where $\mathcal{N}(0)$ is the density of states at the Fermi surface. After some further mathematical approximations, the gap is then given by

$$\Delta \approx 2\hbar\omega_c \exp(-1/\mathcal{N}(0) V_0)$$

Hence, the gap depends exponentially on the density of states at the Fermi surface.

2.1.3 BCS experiments in cold atoms

For the usual s-wave pairing case, fermionic quantum gas apparatus have been able to probe BCS states from early on. These experiments rely crucially on the ability to tune the atomic interaction via Feshbach resonances. Using

¹The Cooper approximation is included in the original BCS publication [42]. With the terminology used here, it is presented in different textbooks, for example [48].

this, the fermionic system can be forced to form a state of tightly bound, bosonic molecules² or a BCS state. These regimes are smoothly connected by a strongly interacting regime which is not well understood in many-body theory. Many experiments have investigated this BEC-BCS crossover and observed condensation in different interaction regimes, for example [49, 50, 51, 52]. Using radio-frequency excitations, the pairing gap could be probed without [53] and with angular sensitivity [54]. The effect of spin-imbalance on superfluidity has been investigated experimentally as well [55, 56].

2.1.4 Pairing in unconventional superconductors

The key to understand high- T_c superconductivity is buried in the pairing mechanism that leads to pair formation. Only a few months after the first cuprate superconductor, theoretical attempts were published that approached this topic. As the most prominent one, P. W. Anderson put forward his resonating valence bond (RVB) theory [57, 58, 59]. Around the same time, D. J. Scalapino investigated how spin-fluctuations might mediate d-wave symmetry electron pairing [60, 61].

The research field of high- T_c superconductivity certainly does not suffer from deficit of exciting publications: 32 years after the groundbreaking publication by Bednorz and Müller [40], this paper has been cited - according to Google Scholar - about 17 000 times. This can be taken as a benchmark for the enormous size of the field. To put it into the words of an experienced theorist: “Taking into account the enormous number of researchers involved in this field, one can assume that almost all possible ideas were expressed and that the main problem is just to select the basic simple concepts from the pile of available theoretical results.” [62]

There have been several review articles on the pairing mechanism. Despite all these attempts to present the field’s status in a coherent way, the current situation is still rather confusing. This confusion has been compounded by the discovery of different high- T_c superconductors where it is expected that the microscopic pairing mechanisms will also differ substantially. I will discuss cuprate superconductors as these systems are the ones where we expect to be able to perform useful quantum simulations. Specifically, I will discuss the material YBCO as a generic example for cuprate superconductors. For readers interested in a wider overview in pairing mechanisms in unconventional superconductors, I can recommend Scalapino’s review article [63] as well as [64, 65, 66].

²Typically referred to as BEC state, as these molecules are cold enough to Bose-condense.

2.1.4.1 Crystal structure and parametrization

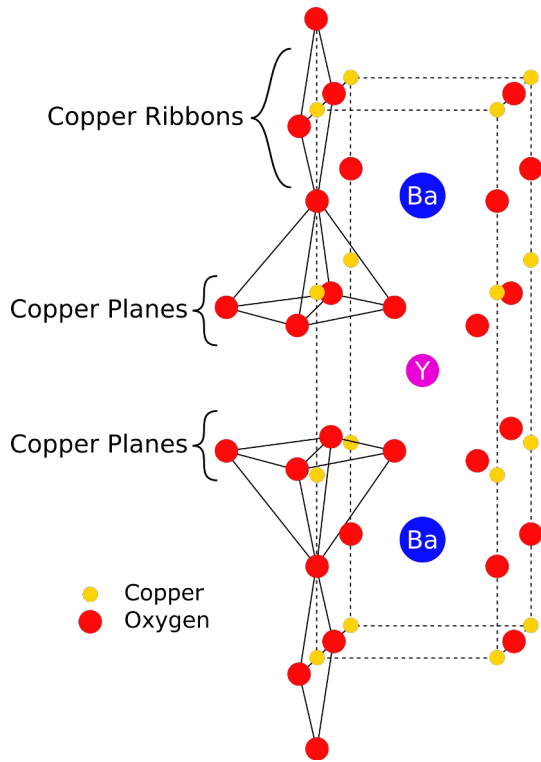


Figure 2.2: YBCO structure.
 File: Ybco002.svg, by Rswarbrick, [CC-BY-SA-3.0], via Wikimedia Commons

The crystal structure referred to as YBCO is $\text{YBa}_2\text{Cu}_3\text{O}_{7-x}$ where x denotes some doping that will turn out to be crucial for the crystal's physical properties. A sketch of the YBCO crystal structure is shown in Fig. 2.2. Its decisive feature are planes of copper oxide CuO_2 which have a cubic structure. These planes are generally considered to be responsible for the unconventional superconductivity. With each unit cell containing two copper atoms located inside copper oxide planes and one copper atom which is not part of a plane, the doping x on a unit cell is not to be confused with the resulting doping of an in-plane copper atom. In real crystals, the cuprate planes are not perfectly flat, as the copper atoms are pulled towards the barium atoms. Each copper plane has one neighboring plane, other planes are much farther away. One of the big questions with respect to the copper planes is,

whether or to what extent tunneling dynamics between neighboring planes is relevant.

Let us consider the electronic structure of the cuprate layers in a little more detail: Copper, atomic number 29, has the electron configuration $[\text{Ar}] 3d^{10}4s^1$. In the YBCO crystal, copper is found as Cu^{2+} with one electron removed from the 4s-shell and one from the 3d shell. For the oxygen with atomic number 8, the electron configuration is $1s^2 2s^2 2p^4$. As a part of the YBCO crystal, each oxygen accepts 2 electrons and has a fully occupied 2p-shell. With one hole in the copper 3d-shell, this hole can occupy five different orbitals as shown in Fig. 2.3. In the YBCO crystal, the hole typically favors the $3d_{x^2-y^2}$ orbital with lobes pointing towards the oxygen ions, see for example [67]. In a simplified picture, the p-orbital of the oxygen ion is aligned along the Cu-O-Cu bond direction as well and forms an overlap with the d-orbitals of the copper ions³. In the early days of high- T_c theory, controversy about the role of oxygen in the

³Of course, one has to consider the hybridization of these orbitals for quantitative analysis.

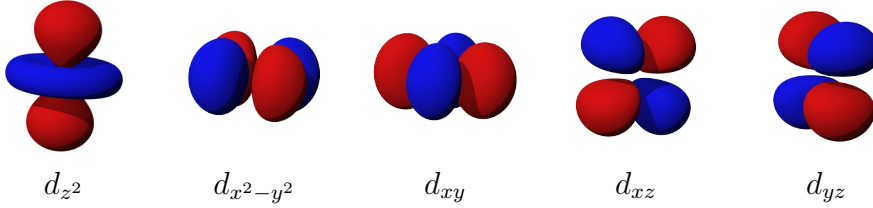


Figure 2.3: For the hole in the Cu 3d-shell, five different orbitals are possible. With x and y axis chosen along the Cu-O bonds, the hole will primarily occupy the $d_{x^2-y^2}$ shell. by Dhatfield, files D3M0.png/Dx2-y2_orbital.png/Dxy_orbital.png/Dxz_orbital.png/Dyz_orbital.png, [CC BY-SA 3.0], via Wikimedia Commons

pairing mechanism arose. Now, the usual notion is that the cuprate planes can be appropriately described as a square lattice with single atomic basis. In this sense, the oxygen ions do alter the transport characteristics along the Cu-O-Cu bonds, but this simply modifies the tunneling parameter. A pioneering work on how to transform the cuprate system into a single-band effective Hamiltonian was presented by Zhang and Rice in 1988 [68].

At this point, it is important to notice that the d-wave symmetry found in the orbital of the copper electron-hole does not necessarily have anything to do with the crystal as a whole showing d-wave symmetry in the gap function. This will become obvious when constructing d-wave symmetric functions in the framework of the Hubbard-model in Sec. 2.3. However, the crystalline structure is relevant when defining the parameters used in Hubbard-type Hamiltonians.

2.1.4.2 High- T_c superconductors and Hubbard models

The Hubbard model was introduced by J. Hubbard in 1963 [69]. It is the simplest microscopic solid-state theory covering both metal and insulator regimes. On a lattice, it reduces the possible processes to electron tunneling between sites and electron-electron (Coulomb) repulsion if two electrons occupy the same site. It is a single-band model in the sense of having only one orbital per lattice site that can be occupied by two electrons of opposite spin. In the original form, the model has the following Hamilton operator:

$$H = - \sum_{i,j,\sigma} t_{ij} c_{i\sigma}^\dagger c_{j\sigma} + U \sum_i n_{i\uparrow} n_{i\downarrow}$$

Here, the indices i and j denote the lattice sites and $\sigma \in \{\uparrow, \downarrow\}$ the spin. t_{ij} is the tunneling coefficient between sites i and j . In the simplest approximation, this term takes the same value for all possible nearest-neighbour tunneling connections and zero for all higher order tunnelings. The operator $n_{i\sigma} = c_{i\sigma}^\dagger c_{i\sigma}$ counts the number of σ -spins on site i . If nearest and next-nearest neighbor

tunneling is taken into account, this model is sometimes called the t, t' -Hubbard model. Recent theoretical publications on the high- T_c mechanism making use of this Hamiltonian include [62]. The Hubbard Hamiltonian has been studied intensively using ultracold atoms in optical lattices using bosons, fermions and different parameter regimes. There exist numerous publications on such experiments, I list some particularly relevant ones here: In 2005, the Esslinger group reported on the observation of the formation of a band-insulating state of ^{40}K atoms in an optical lattice [70]. Few years later, experiments were able to investigate the transition between metallic and Mott-insulating state by preparing ^{40}K atoms in an optical lattice with repulsive interactions [71] and [72]. After the advent of fermionic quantum gas microscopes, the Mott insulating state [73] as well as the antiferromagnetic state [74] could be probed in-situ.

In 1977, J. Spalek formulated a strong coupling version of the Hubbard model, the so-called t - J model [75, 76]. In the regime covered by this model, on-site interactions are strong enough to avoid double occupation of lattice sites. Now, an exchange interaction mediated by second order virtual hopping becomes relevant. The resulting Hamilton operator

$$H = - \sum_{i,j,\sigma} t_{ij} c_{i\sigma}^\dagger c_{j\sigma} + \sum_{i,j} \frac{4t_{ij}^2}{U} \left(\vec{S}_i \cdot \vec{S}_j - \frac{n_i n_j}{4} \right)$$

includes a spin-dependent exchange interaction term and a spin-independent on-site interaction term with number operators $n_i = \sum_\sigma n_{i\sigma}$. Often, the last term is insignificant and can be omitted. The exchange term is not necessarily restricted to nearest neighbors. This Hamiltonian serves as the foundation for the RVB theory. Since the discovery of high- T_c , this theoretical approach had been modified several times, for example regarding the question whether inter-layer processes play a significant role. The latest version of the theory is presented in [67] which is instructive to read as it also includes historical and biographical perspectives on how things developed. Resonating valence-bond states had been proposed by Anderson long before - in 1973 - as a quantum state that might be useful for estimating the ground state energy of antiferromagnetic fermions in low dimensions at half filling [77]. The basic idea is to have a singlet pair formation among the electrons at positions i and j with a singlet pair creation operator⁴

$$s_{ij}^\dagger = \frac{1}{\sqrt{2}} \left(c_{i\uparrow}^\dagger c_{j\downarrow}^\dagger - c_{i\downarrow}^\dagger c_{j\uparrow}^\dagger \right) \quad (2.3)$$

Anderson states that “[The electrons] regain some of the lost antiferromagnetic exchange energy by resonating quantum mechanically among different pairing configurations.” [78]. Thus, the antiferromagnetic system should favor such a

⁴This singlet wavefunction describes a valence bond in solids.

RVB state. After the discovery of high- T_c materials, Anderson realized that his RVB state can be obtained from the well known BCS superconducting state (2.1) by performing a so-called Gutzwiller projection

$$P = \prod_i (1 - n_{i\uparrow}n_{i\downarrow})$$

deleting all double site occupations from the wavefunction:

$$|\Psi_{RVB}\rangle = P \prod_k (u_k + v_k c_{k\uparrow}^\dagger c_{-k\downarrow}^\dagger) |0\rangle$$

Furthermore, the evolution is assumed to be subject to a modified t-J Hamiltonian

$$H = -P \sum_{i,j,\sigma} t_{ij} c_{i\sigma}^\dagger c_{j\sigma} P + \sum_{i,j} \frac{4t_{ij}^2}{U} \vec{S}_i \cdot \vec{S}_j$$

which restricts the state to the single-occupancy Hilbert subspace.

When the RVB state is sufficiently doped, it describes - in terms of a mean-field theory - a superconductor [57, 58] that does indeed favor a d-wave symmetry for the order parameter [79, 80]. Though the projection technique applied in RVB is rather crude and therefore debated, considering cuprate superconductors as doped antiferromagnetic Mott insulators is nowadays the common approach. The idea of singlet pair formation has been adopted by later theoretical attempts - see Sec. 2.3 - and there has been some experimental evidence supporting the assumption of the cuprate planes being dominated by singlet pairs [81, 82, 83]. With respect to Hubbard plaquettes filled with ultracold polar molecules, there exist detailed predictions for different parameter regimes of a generalized t-J Hamiltonian [84] that might suggest new cold atom experiments.

An up-to-date review on Hubbard models in optical lattices is given in [85].

2.1.5 The pseudogap

A common property of high- T_c superconductors is the existence of a so-called “pseudogap” phase. It occurs (in the case of hole-doped cuprates) in the regime of underdoping, i.e. too small hole doping. This phase exists for temperatures up to room temperature (in real solid-state systems), exhibits unusual electronic properties and shows precursors of Cooper-pair formation. Where to find this phase in the parameter space of temperature and doping is illustrated in Fig. 2.4. All kinds of experiments conducted to investigate the gap in the superconducting phase made unexpected discoveries in the pseudogap regime. These experiments have been reviewed in [86]. From the perspective of constructing similar systems made of optically-trapped cold atoms, it is very

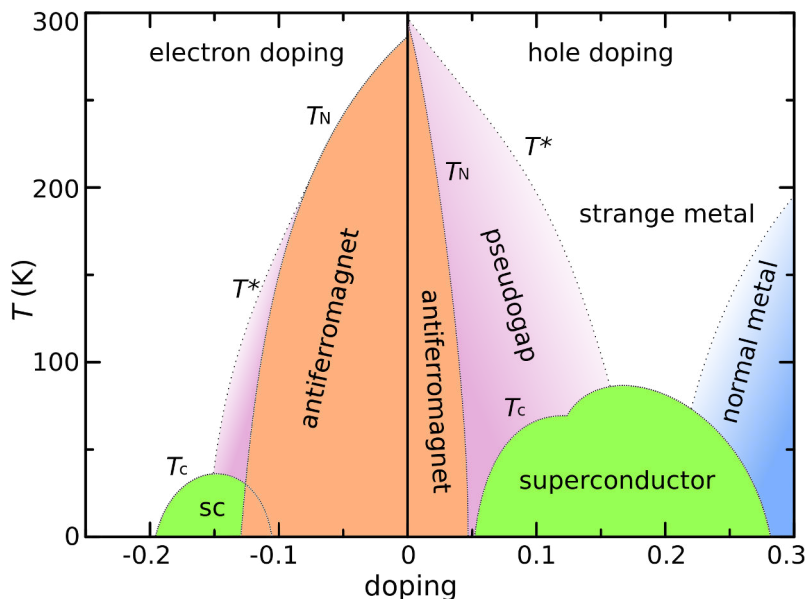


Figure 2.4: A typical phase diagram for cuprate superconductors. Here, the doping parameter refers to the doping of a single copper atom in the cuprate plane. In the undoped material, the relevant copper orbital is half filled - one hole per site. For example, with a doping of 0.25, there is one additional hole per four copper sites. One might then as well speak of 3/8 filling. by Holger Motzkau, [CC BY-SA 3.0], https://commons.wikimedia.org/wiki/File:Cuprates_phasedigagram_en.svg, via Wikimedia Commons

exciting to see that a spatial modulation of electron density appearing alongside of the pre-formation of Cooper pairs in the pseudogap phase has been imaged using scanning tunneling microscopy [87]. A theory [88] described this as a formation of d-wave Cooper pairs without global phase coherence.

The questions of how this pseudogap phase works and how it is linked to the superconducting phase is still one of the more controversial topics, with the idea of preformed pairs not being favored by everyone. Experiments with fermionic quantum gas microscopes might be helpful for a better understanding of the pseudogap phase - the relevant regime should not be too difficult to reach. At first, one could reproduce and image the density-wave formation. Next, one could investigate the k-space formation of pairs by analyzing correlations after free expansion, as proposed in [89] and previously demonstrated in [90]. Recently, the Jochim group used a single-atom sensitive time-of-flight imaging scheme to study momentum correlations of fermions in small Hubbard-type systems based on optical tweezers [91].

2.2 Experimental manifestations of the d-wave order parameter

In this section, I will introduce two important experiments which provide evidence for the d-wave order parameter in cuprate superconductors.

The d-wave symmetry of the order parameter is characterized by a direction dependence in both amplitude and phase. Both have been measured experimentally. Here, I will restrict myself to a more detailed presentation of the phase dependent measurements. These are more impressive and more expressive than the amplitude measurements: A direction dependent amplitude alone could also be due to a special type of s-wave symmetry. An experimental technique successfully used for measuring the direction dependence of the amplitude of the order parameter is angle-resolved photoemission spectroscopy [92, 93].

For readers interested in details going beyond this little summary, I recommend the very accessible review article [94] as a starting point. Here, I will introduce two phase-sensitive experiments that delivered evidence for the order parameter in the high- T_c superconductor YBCO being d-wave symmetric. Both experiments are based on special types of superconducting quantum interference devices (SQUID). SQUIDS are composed of superconducting loops containing Josephson junctions. The electrical properties are strongly influenced by the magnetic flux through the superconducting loop. As it is a quantum device, it is sensitive to single magnetic flux quanta. Generally, one distinguishes DC SQUIDS which contain two and RF SQUIDS containing one Josephson junction. Both SQUID types can be used to explore the symmetry of the order parameter - here I restrict myself to the conceptually easier case with two junctions. For d-wave symmetries, this kind of experiment was proposed by M. Sigrist and T.M. Rice in [96]. First experimental results were published only one year later by Wollman et al. [95].

A schematic of the SQUID structure used by Wollman et. al. for detecting the d-wave symmetry in YBCO is shown in Fig. 2.5: A YBCO crystal (orange) is connected to an ordinary

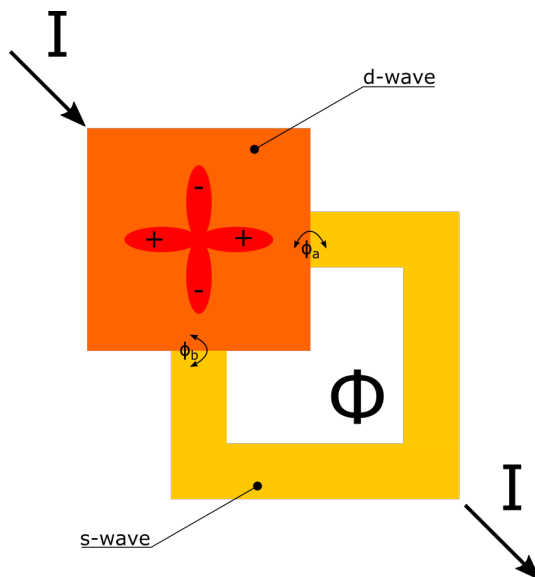


Figure 2.5: Schematic of a SQUID used for proving the existence of a sign change in the YBCO order parameter, adopted from [95].

s-wave superconductor (lead, drawn in yellow) via two perpendicular Josephson junctions. The crystal is oriented such that the lobes of the order parameter face towards the junctions. As the tunneling through the junction depends strongly on the thickness of the isolating material, the process is very sensitive to the direction of the tunneling current. This direction selectivity is crucial for probing the symmetry of the superconducting order parameter, as it is a function in momentum space.

The superconducting structure made from d-wave and s-wave materials forms a loop and the magnetic flux through this loop is denoted by Φ . It will be shown that this magnetic flux strongly influences the current I driven through the system.

At a Josephson junction, the current flow depends on the relative phase of the order parameter on both sides on the junction. This effect had been predicted by B. D. Josephson in 1962 [97] and was clearly identified in experiment by P. W. Anderson in 1963 [98]. In 1960, the effect had already been observed by I. Giaever [99], who received a Nobel prize together with Josephson in 1974 [100, 101]. In the structure introduced above, the total current I driven through the assembly splits up and crosses the two junctions. With the order parameter phase differences across the junctions ϕ_a and ϕ_b and the critical currents I_a and I_b , the total current is given by

$$I = I_a \sin \phi_a + I_b \sin \phi_b$$

With δ_{ab} being the intrinsic phase shift of the YBCO crystal and respecting the Aharonov-Bohm-effect [102], the phases have to fulfill the constraint

$$\phi_a - \phi_b + 2\pi \frac{\Phi}{\Phi_0} + \delta_{ab} = 0$$

where Φ_0 denotes the magnetic flux quantum.

Here, the magnetic flux Φ is composed of an externally applied component and the one that would emerge from a ring current J flowing around the SQUID. Assuming that the inductivity of the SQUID L is small, one can neglect the ring current contribution:

$$\Phi = \Phi_{ext} + LJ = \Phi_{ext}$$

Assuming $I_a = I_b = I_0$ and combining these relations using a sine addition theorem, one obtains a simple expression for the current as a function of ϕ_a ,

ϕ_b , Φ_{ext} and δ_{ab} :

$$\begin{aligned}
I &= I_0 (\sin \phi_a + \sin \phi_b) \\
&= 2I_0 \sin \frac{\phi_a + \phi_b}{2} \cos \frac{\phi_a - \phi_b}{2} \\
&= 2I_0 \sin \frac{\phi_a + \phi_b}{2} \cos \left(\pi \frac{\Phi_{ext}}{\Phi_0} + \frac{\delta_{ab}}{2} \right)
\end{aligned}$$

This expression can not be tested experimentally in a reasonable way, as there are still phases involved. Fortunately, the maximum value of this expression is identical to the critical current of the SQUID device. This observable

$$I_c(\Phi_{ext}) = 2I_0 \left| \cos \left(\pi \frac{\Phi_{ext}}{\Phi_0} + \frac{\delta_{ab}}{2} \right) \right|$$

can be measured by increasing the current I until the superconducting state breaks down. In the case of d-wave superconductivity, the intrinsic phase shift is $\delta_{ab} = \pi$, when the two junctions are connected to orthogonal crystal surfaces. This phase shift could be confirmed in experiments by evaluating the critical current for different externally applied magnetic fluxes. The experiment was also conducted for the case of both junctions being connected to the same edge of the YBCO crystal such that $\delta_{ab} = 0$. Wollman et. al. could also produce the expected result for this cross-check. Schematically, the function $I_c(\Phi_{ext})$ is shown in Fig. 2.6.

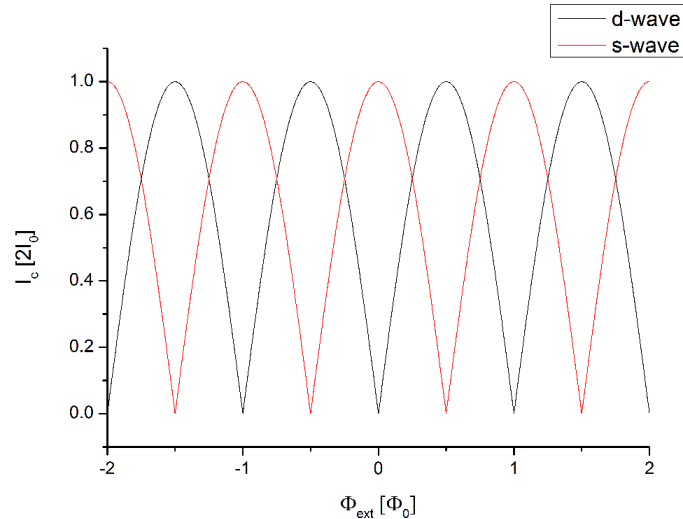


Figure 2.6: Calculation of the expected critical currents for the SQUID structure shown in Fig. 2.5 with different externally applied magnetic fluxes. The plot was created using [94].

Shortly after the results of these SQUID experiments had been published, new evidence for d-wave symmetry in the order parameter arose from another type of experiment [103, 104]. This experiment is also based on the proposal [96] by Sigrist and Rice but here YBCO crystals with different orientations were joined to form ring structures.

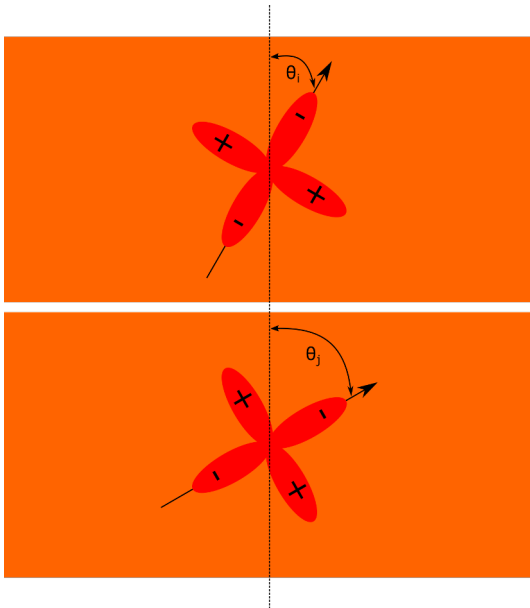


Figure 2.7: Illustration of the geometry at a junction of two differently oriented d-wave superconductors.

At such a junction, see Fig. 2.7, the supercurrent I_s not only depends on the phase of the order parameter across the junction, but also on its orientation with respect to the crystallographic axes [103]

$$\begin{aligned} I_s^{ij} &= A^{ij} \cos 2\theta_i \cos 2\theta_j \sin \Delta\phi_{ij} \\ &= I_c^{ij} \sin \Delta\phi_{ij} \end{aligned} \quad (2.4)$$

The different possible crystal geometries around the junction can then be classified in so-called “0-junctions” where $I_c^{ij} > 0$ and “ π -junctions” where $I_c^{ij} < 0$. For illustration, the limiting cases of these different junction types are shown in Fig. 2.8. To interpret these illustrations correctly, one should keep in mind that the d-wave orbitals drawn are features in k-space, not real space. Due to the highly directional coupling through a

junction, the tunneling is direction selective to the pair momentum.

When a closed superconducting loop with junctions having different orientations as shown in Fig. 2.9 is considered, one can construct geometries where the order parameter phase acquires an odd-numbered multiple of π each time the loop is circulated. This requires the number of π -junctions to be odd. Alternatively, the phase change can be 0.

Beautiful experiments showed that in superconducting rings, where a phase difference of π per cycle is collected, a supercurrent builds up spontaneously on cooling the sample below the critical temperature. The magnetic flux connected to this supercurrent was measured using a scanning SQUID device as a magnetic field sensor and had a value of $\Phi_0/2$.

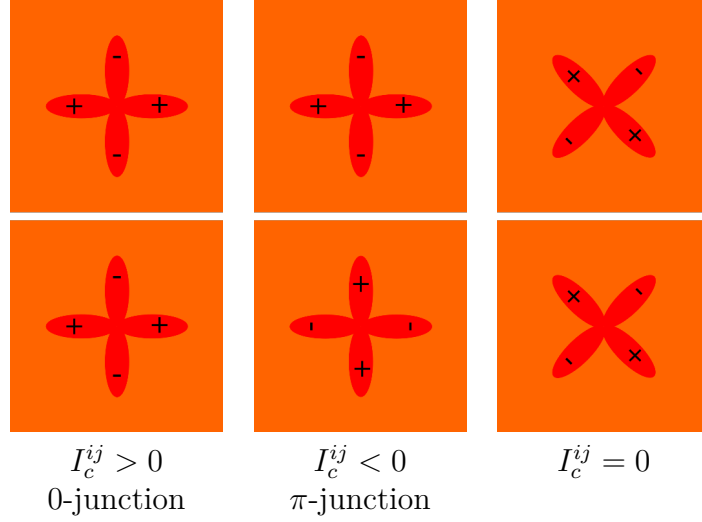


Figure 2.8: Simplest examples for different kinds of junctions between d-wave superconducting crystals.

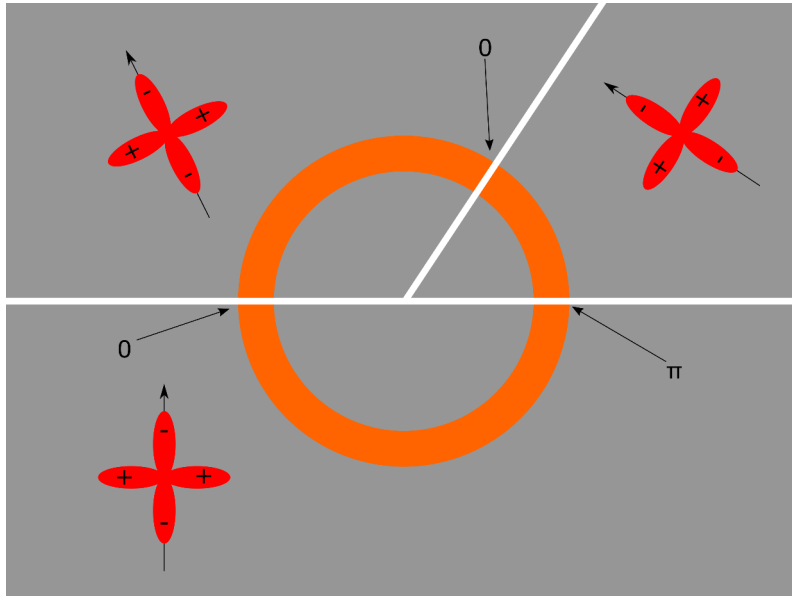


Figure 2.9: Three YBCO ring segments are grown epitaxially on the surfaces of three differently oriented crystals. Thus, the order parameter in the ring segments has different orientations as well. According to (2.4), the three junctions can be classified as 0- or π -junctions. As the ring consists of two 0-junctions and one π -junction, the order parameter picks up a phase of π when going around the loop once. This phase is connected with an intrinsic supercurrent that builds up spontaneously when cooling the sample below the critical temperature.

2.3 d-wave physics in plaquette systems

Despite the conceptual simplicity of Hubbard models, the Hilbert space needed to describe them grows exponentially with the number of sites rendering both exact diagonalization and numerical studies difficult. In 2007, D. Scalapino wrote a chapter in the “Handbook of High-Temperature Superconductivity” [105] that might serve as a starting point for getting familiar with the most important techniques. The simplest 2D-Hubbard system with d-wave states is a 2x2 plaquette. This is particularly interesting, as it is exactly solvable and can be studied experimentally with quantum microscopes. This section is intended

- to explain how to identify d-wave symmetry plaquette states.
- to make the reader familiar with such states by presenting some important plaquette basis states in the subspace of a fixed number of spins.
- to clarify the meaning of the gap function in the context of plaquettes.
- to pick up on theoretical studies that might suggest interesting experiments to be conducted with single plaquettes or superlattices of plaquettes.

2.3.1 Identifying d-wave symmetry

Later in this thesis, quantum states featuring $d_{x^2-y^2}$ symmetry are of central importance. To identify the d-wave symmetry, let us consider the group theoretic foundation of what d-wave symmetry means. Consider a $d_{x^2-y^2}$ -orbital with coordinates chosen as shown in Fig. 2.10a.

The orbital is invariant under the following operations:

- π rotations around the z-axis
- π rotations around the x- and y-axes

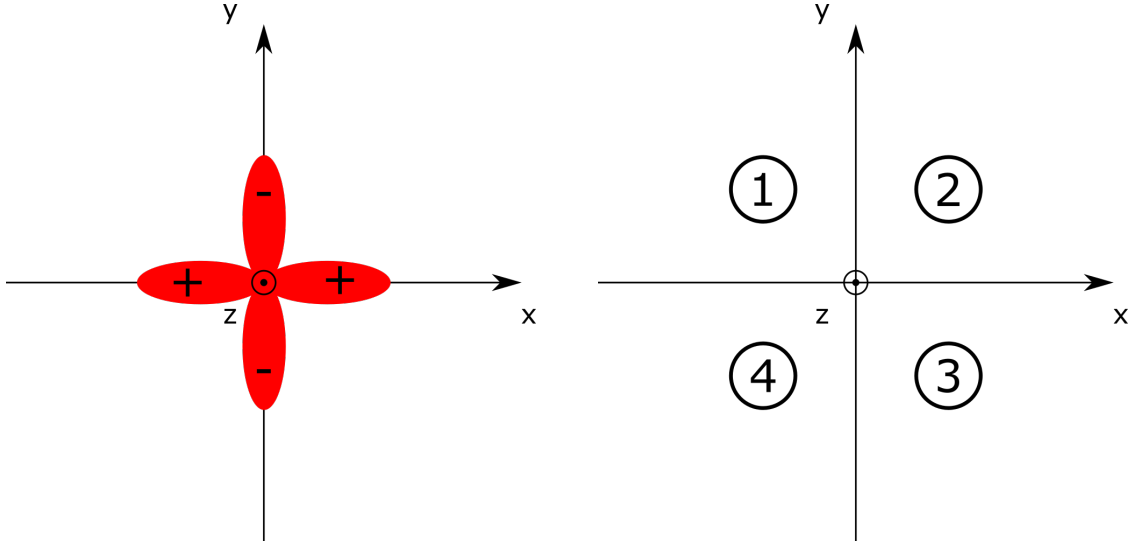
The sign of the wavefunction changes under

- clockwise and counterclockwise $\pi/2$ rotations around the z-axis.
- π rotations around the diagonals $x = y$ and $x = -y$.

A quantum state obeying these symmetries will be called d-wave symmetric. Now let’s consider what this implies for the states on a four-site plaquette where the sites are numbered as in Fig. 2.10b.

Applying the operations given above to the plaquette, the quantum state must not change under the following site replacements⁵:

⁵The $i \rightarrow j$ notation means: Replace i with j .



(a) The d-orbital's symmetries are considered with a choice of coordinates as shown in this figure.

(b) The plaquette sites are labeled according to the numbering shown here.

Figure 2.10: Definition of the coordinates and site indices used here.

- π rotations around the z -axis: $1 \leftrightarrow 3, 2 \leftrightarrow 4$
- π rotations around the x -axis: $1 \leftrightarrow 4, 2 \leftrightarrow 3$
- π rotations around the y -axis: $1 \leftrightarrow 2, 3 \leftrightarrow 4$

The quantum state must change its sign under the site replacements:

- clockwise $\pi/2$ rotations around the z -axis: $1 \rightarrow 4, 2 \rightarrow 1, 3 \rightarrow 2, 4 \rightarrow 3$
- counterclockwise $\pi/2$ rotations around the z -axis: $1 \rightarrow 2, 2 \rightarrow 3, 3 \rightarrow 4, 4 \rightarrow 1$
- π rotation around the diagonal $x = y$: $1 \leftrightarrow 3$
- π rotation around the diagonal $x = -y$: $2 \leftrightarrow 4$

Now the question is which plaquette states do exhibit d-wave symmetry? Fortunately, a list of d-wave symmetric basis states (as well as the same for other symmetries) for different total numbers of spin-ups and spin-downs is provided in [84].

The notation goes as follows: To create a σ spin on site i of the plaquette, we use a creation operator $c_{i\sigma}^\dagger$. To describe a plaquette state, we list the spins in

the order of the lattice sites. For example, a state with only a spin up on the third site is represented by

$$|00 \uparrow 0\rangle = c_{3\uparrow}^\dagger |0\rangle$$

When there is more than one creation operator involved, like

$$|\uparrow 0 \uparrow 0\rangle = c_{1\uparrow}^\dagger c_{3\uparrow}^\dagger |0\rangle$$

it does matter how the operators are ordered as they obey the fermionic anti-commutation relation $\{c_{i\sigma_i}^\dagger, c_{j\sigma_j}^\dagger\} = 0$.

The following procedure is used to analyze the symmetry of a plaquette state:

1. Write the state $|\Psi\rangle$ in terms of creation operators acting on the vacuum. Arrange the operators with ascending site indices.
2. Switch the indices according to the replacement rules presented above.
3. Restore the ascending site index order by swapping the creation operators accordingly while respecting the anticommutation relations.
4. End up with either $|\Psi\rangle$, $-|\Psi\rangle$ or something completely different.

As an example, consider the ferromagnetic state $|\uparrow\uparrow\uparrow\uparrow\rangle = c_{1\uparrow}^\dagger c_{2\uparrow}^\dagger c_{3\uparrow}^\dagger c_{4\uparrow}^\dagger |0\rangle$. A naive experimentalist might be tempted to call this an isotropic state, but instead we will prove that it has d-wave symmetry. The symmetry operations follow the order presented above.

π rotations around the z-axis:

$$\begin{aligned} c_{1\uparrow}^\dagger c_{2\uparrow}^\dagger c_{3\uparrow}^\dagger c_{4\uparrow}^\dagger |0\rangle &\rightarrow c_{3\uparrow}^\dagger c_{4\uparrow}^\dagger c_{1\uparrow}^\dagger c_{2\uparrow}^\dagger |0\rangle \\ &= -c_{3\uparrow}^\dagger c_{1\uparrow}^\dagger c_{4\uparrow}^\dagger c_{2\uparrow}^\dagger |0\rangle \\ &= c_{3\uparrow}^\dagger c_{1\uparrow}^\dagger c_{2\uparrow}^\dagger c_{4\uparrow}^\dagger |0\rangle \\ &= -c_{1\uparrow}^\dagger c_{3\uparrow}^\dagger c_{2\uparrow}^\dagger c_{4\uparrow}^\dagger |0\rangle \\ &= c_{1\uparrow}^\dagger c_{2\uparrow}^\dagger c_{3\uparrow}^\dagger c_{4\uparrow}^\dagger |0\rangle \end{aligned}$$

π rotations around the x-axis:

$$\begin{aligned} c_{1\uparrow}^\dagger c_{2\uparrow}^\dagger c_{3\uparrow}^\dagger c_{4\uparrow}^\dagger |0\rangle &\rightarrow c_{4\uparrow}^\dagger c_{3\uparrow}^\dagger c_{2\uparrow}^\dagger c_{1\uparrow}^\dagger |0\rangle \\ &= -c_{3\uparrow}^\dagger c_{4\uparrow}^\dagger c_{2\uparrow}^\dagger c_{1\uparrow}^\dagger |0\rangle \\ &= c_{3\uparrow}^\dagger c_{2\uparrow}^\dagger c_{4\uparrow}^\dagger c_{1\uparrow}^\dagger |0\rangle \\ &= -c_{3\uparrow}^\dagger c_{2\uparrow}^\dagger c_{1\uparrow}^\dagger c_{4\uparrow}^\dagger |0\rangle \\ &= c_{3\uparrow}^\dagger c_{1\uparrow}^\dagger c_{2\uparrow}^\dagger c_{4\uparrow}^\dagger |0\rangle \\ &= -c_{1\uparrow}^\dagger c_{3\uparrow}^\dagger c_{2\uparrow}^\dagger c_{4\uparrow}^\dagger |0\rangle \\ &= c_{1\uparrow}^\dagger c_{2\uparrow}^\dagger c_{3\uparrow}^\dagger c_{4\uparrow}^\dagger |0\rangle \end{aligned}$$

π rotations around the y-axis:

$$\begin{aligned}
c_{1\uparrow}^\dagger c_{2\uparrow}^\dagger c_{3\uparrow}^\dagger c_{4\uparrow}^\dagger |0\rangle &\rightarrow c_{2\uparrow}^\dagger c_{1\uparrow}^\dagger c_{4\uparrow}^\dagger c_{3\uparrow}^\dagger |0\rangle \\
&= -c_{1\uparrow}^\dagger c_{2\uparrow}^\dagger c_{4\uparrow}^\dagger c_{3\uparrow}^\dagger |0\rangle \\
&= c_{1\uparrow}^\dagger c_{2\uparrow}^\dagger c_{3\uparrow}^\dagger c_{4\uparrow}^\dagger |0\rangle
\end{aligned}$$

Clockwise $\pi/2$ rotations around z-axis:

$$\begin{aligned}
c_{1\uparrow}^\dagger c_{2\uparrow}^\dagger c_{3\uparrow}^\dagger c_{4\uparrow}^\dagger |0\rangle &\rightarrow c_{4\uparrow}^\dagger c_{1\uparrow}^\dagger c_{2\uparrow}^\dagger c_{3\uparrow}^\dagger |0\rangle \\
&= -c_{1\uparrow}^\dagger c_{4\uparrow}^\dagger c_{2\uparrow}^\dagger c_{3\uparrow}^\dagger |0\rangle \\
&= c_{1\uparrow}^\dagger c_{2\uparrow}^\dagger c_{4\uparrow}^\dagger c_{3\uparrow}^\dagger |0\rangle \\
&= -c_{1\uparrow}^\dagger c_{2\uparrow}^\dagger c_{3\uparrow}^\dagger c_{4\uparrow}^\dagger |0\rangle
\end{aligned}$$

Counterclockwise $\pi/2$ rotations around z-axis:

$$\begin{aligned}
c_{1\uparrow}^\dagger c_{2\uparrow}^\dagger c_{3\uparrow}^\dagger c_{4\uparrow}^\dagger |0\rangle &\rightarrow c_{2\uparrow}^\dagger c_{3\uparrow}^\dagger c_{4\uparrow}^\dagger c_{1\uparrow}^\dagger |0\rangle \\
&= -c_{2\uparrow}^\dagger c_{3\uparrow}^\dagger c_{1\uparrow}^\dagger c_{4\uparrow}^\dagger |0\rangle \\
&= c_{2\uparrow}^\dagger c_{1\uparrow}^\dagger c_{3\uparrow}^\dagger c_{4\uparrow}^\dagger |0\rangle \\
&= -c_{1\uparrow}^\dagger c_{2\uparrow}^\dagger c_{3\uparrow}^\dagger c_{4\uparrow}^\dagger |0\rangle
\end{aligned}$$

π rotation around the diagonal $x = y$:

$$\begin{aligned}
c_{1\uparrow}^\dagger c_{2\uparrow}^\dagger c_{3\uparrow}^\dagger c_{4\uparrow}^\dagger |0\rangle &\rightarrow c_{3\uparrow}^\dagger c_{2\uparrow}^\dagger c_{1\uparrow}^\dagger c_{4\uparrow}^\dagger |0\rangle \\
&= -c_{3\uparrow}^\dagger c_{1\uparrow}^\dagger c_{2\uparrow}^\dagger c_{4\uparrow}^\dagger |0\rangle \\
&= c_{1\uparrow}^\dagger c_{3\uparrow}^\dagger c_{2\uparrow}^\dagger c_{4\uparrow}^\dagger |0\rangle \\
&= -c_{1\uparrow}^\dagger c_{2\uparrow}^\dagger c_{3\uparrow}^\dagger c_{4\uparrow}^\dagger |0\rangle
\end{aligned}$$

π rotation around the diagonal $x = -y$:

$$\begin{aligned}
c_{1\uparrow}^\dagger c_{2\uparrow}^\dagger c_{3\uparrow}^\dagger c_{4\uparrow}^\dagger |0\rangle &\rightarrow c_{1\uparrow}^\dagger c_{4\uparrow}^\dagger c_{3\uparrow}^\dagger c_{2\uparrow}^\dagger |0\rangle \\
&= -c_{1\uparrow}^\dagger c_{3\uparrow}^\dagger c_{4\uparrow}^\dagger c_{2\uparrow}^\dagger |0\rangle \\
&= c_{1\uparrow}^\dagger c_{3\uparrow}^\dagger c_{2\uparrow}^\dagger c_{4\uparrow}^\dagger |0\rangle \\
&= -c_{1\uparrow}^\dagger c_{2\uparrow}^\dagger c_{3\uparrow}^\dagger c_{4\uparrow}^\dagger |0\rangle
\end{aligned}$$

Accordingly, $|\uparrow\uparrow\uparrow\uparrow\rangle$ is actually a d-wave state.

2.3.2 Selected plaquette states

Referring to the more general basis state overview presented in [84], I list some important basis states of the four-site plaquette up to half-filling classified by

the total numbers of spin ups n_\uparrow and spin downs n_\downarrow . This includes states of different symmetry. In the following, we label such states $|n_\uparrow, n_\downarrow, (symmetry)\rangle$. For some spin numbers and symmetries, more than one basis state exists.

For the singly-occupied plaquette $|1, 0\rangle$ as well as the doubly-occupied, spin polarized case $|2, 0\rangle$, no d-wave symmetric states exist. The simplest d-wave plaquette state has two spins and is described by

$$|1, 1, d\rangle = \frac{1}{2\sqrt{2}} (|\uparrow 00 \downarrow\rangle - |\downarrow 00 \uparrow\rangle + |0 \uparrow \downarrow 0\rangle - |0 \downarrow \uparrow 0\rangle \\ + |\downarrow \uparrow 00\rangle - |\uparrow \downarrow 00\rangle + |00 \downarrow \uparrow\rangle - |00 \uparrow \downarrow\rangle)$$

This state can be expressed in a simpler way by using the singlet pair creation operator s_{ij}^\dagger introduced in (2.3):

$$|1, 1, d\rangle = \frac{1}{2} (s_{14}^\dagger + s_{23}^\dagger - s_{12}^\dagger - s_{34}^\dagger) |0\rangle \quad (2.5)$$

Within the $n_\uparrow = 1, n_\downarrow = 1$ subspace, there exist two different s-wave basis states that can be expressed in terms of valence bonds:

$$|1, 1, s^1\rangle = \frac{1}{2} (s_{14}^\dagger + s_{23}^\dagger + s_{12}^\dagger + s_{34}^\dagger) |0\rangle \\ |1, 1, s^2\rangle = \frac{1}{\sqrt{2}} (s_{13}^\dagger + s_{24}^\dagger)$$

These states are particularly important as, according to [84], the $n_\uparrow = 1, n_\downarrow = 1$ ground state is a superposition of $|1, 1, s^1\rangle$ and $|1, 1, s^2\rangle$. For a plaquette with this filling, one can also think about it as being occupied by two paired holes.

For plaquettes with a total filling of three spins, the subspace $n_\uparrow = 2, n_\downarrow = 1$ is primarily relevant. It features a variety of basis states of all different symmetries, including p-waves. This subspace is considered to be very important for dynamics on plaquettes, as its structure influences how plaquettes go from $n_\uparrow = 2, n_\downarrow = 2$ to $n_\uparrow = 1, n_\downarrow = 1$ when being coupled - a process that can be interpreted as a traveling hole-pair.

In the $n_\uparrow = 2, n_\downarrow = 2$ subspace, two d-wave basis states exist

$$|2, 2, d^1\rangle = \frac{1}{2} (|\downarrow \downarrow \uparrow \uparrow\rangle + |\uparrow \downarrow \downarrow \uparrow\rangle + |\downarrow \uparrow \uparrow \downarrow\rangle + |\uparrow \uparrow \downarrow \downarrow\rangle) \\ |2, 2, d^2\rangle = \frac{1}{\sqrt{2}} (|\downarrow \uparrow \downarrow \uparrow\rangle + |\uparrow \downarrow \uparrow \downarrow\rangle)$$

which form the ground state. So, this ground state is d-symmetric.

2.3.3 The gap operator

For an s-wave ground state of the doubly-occupied plaquette $|2\rangle$ and a d-wave ground state of the plaquette populated by four spins $|4\rangle$, the operator connecting these two states must have d-wave symmetry. Here, one should not forget: The gap function we know from solid-state theory and experiments exists in momentum space $\Delta(k)$ and of course the d-wave symmetry is also in momentum space. The earliest publication known to me that gives an explicit expression for the manifestation of this k-space symmetry in real space is by Scalapino [66] where the operator for adding a d-wave symmetric pair of holes is given by

$$\hat{\Delta}_d = \frac{1}{N} \sum_p \Delta_d(p) c_{p,\uparrow} c_{-p,\downarrow}$$

with the d-wave momentum dependence being hidden in

$$\Delta_d(p) = \Delta_0 (\cos p_x - \cos p_y)$$

This gap operator can be expanded in real space by summing over all lattice sites l with lattice vectors x and y :

$$\begin{aligned} \hat{\Delta}_d &= \frac{1}{N} \sum_l \frac{\Delta_0}{4} [(c_{l+x,\uparrow} c_{l,\downarrow} - c_{l+x,\downarrow} c_{l,\uparrow}) - (c_{l+y,\uparrow} c_{l,\downarrow} - c_{l+y,\downarrow} c_{l,\uparrow}) \\ &\quad (c_{l-x,\uparrow} c_{l,\downarrow} - c_{l-x,\downarrow} c_{l,\uparrow}) - (c_{l-y,\uparrow} c_{l,\downarrow} - c_{l-y,\downarrow} c_{l,\uparrow})] \\ &= \frac{1}{N} \sum_l \frac{\Delta_0}{2\sqrt{2}} [s_{l+x,l} - s_{l+y,l} + s_{l-x,l} - s_{l-y,l}] \end{aligned}$$

In the last step, the operator $s_{r,r'}$ creates a singlet pair of holes between site r and r' . Inside the sum, this expression has the same form as the operator in (2.5) which creates a d-wave pair of spins. Here, holes are created instead.

When reducing our system from a lattice to a plaquette, the pair of holes creation operator simplifies to

$$\hat{\Delta}_d = \frac{1}{2} (s_{12} + s_{34} - s_{14} - s_{23})$$

Applying this operator to a d-wave $|4\rangle$ state turns it into an s-wave $|2\rangle$ state.

As an illustrative example, I will show how it acts on the basis state $|2, 2, d^2\rangle$:

$$\begin{aligned}
\hat{\Delta}_d |2, 2, d^2\rangle &\propto (s_{12} + s_{34} - s_{14} - s_{23}) (|\downarrow\uparrow\downarrow\uparrow\rangle + |\uparrow\downarrow\uparrow\downarrow\rangle) \\
&= (s_{12} + s_{34} - s_{14} - s_{23}) (c_{1\downarrow}^\dagger c_{2\uparrow}^\dagger c_{3\downarrow}^\dagger c_{4\uparrow}^\dagger + c_{1\uparrow}^\dagger c_{2\downarrow}^\dagger c_{3\uparrow}^\dagger c_{4\downarrow}^\dagger) |0\rangle \\
&= (c_{1\uparrow} c_{2\downarrow} - c_{1\downarrow} c_{2\uparrow} + c_{3\uparrow} c_{4\downarrow} - c_{3\downarrow} c_{4\uparrow} \\
&\quad - c_{1\uparrow} c_{4\downarrow} + c_{1\downarrow} c_{4\uparrow} - c_{2\uparrow} c_{3\downarrow} + c_{2\downarrow} c_{3\uparrow}) (c_{1\downarrow}^\dagger c_{2\uparrow}^\dagger c_{3\downarrow}^\dagger c_{4\uparrow}^\dagger + c_{1\uparrow}^\dagger c_{2\downarrow}^\dagger c_{3\uparrow}^\dagger c_{4\downarrow}^\dagger) |0\rangle \\
&= (-c_{3\uparrow}^\dagger c_{4\downarrow}^\dagger + c_{3\downarrow}^\dagger c_{4\uparrow}^\dagger - c_{1\uparrow}^\dagger c_{2\downarrow}^\dagger + c_{1\downarrow}^\dagger c_{2\uparrow}^\dagger + c_{2\downarrow}^\dagger c_{3\uparrow}^\dagger - c_{2\uparrow}^\dagger c_{3\downarrow}^\dagger + c_{1\downarrow}^\dagger c_{4\uparrow}^\dagger - c_{1\uparrow}^\dagger c_{4\downarrow}^\dagger) |0\rangle \\
&= -|00 \uparrow\downarrow\rangle + |00 \downarrow\uparrow\rangle - |\uparrow\downarrow 00\rangle + |\downarrow\uparrow 00\rangle \\
&\quad + |0 \uparrow\downarrow 0\rangle - |0 \downarrow\uparrow 0\rangle + |\uparrow 00 \downarrow\rangle - |\downarrow 00 \uparrow\rangle \\
&\propto |1, 1, s^1\rangle
\end{aligned}$$

Within this calculation, the anticommutator $\{c_\alpha, c_\beta^\dagger\} = \delta_{\alpha\beta}$ is used.

2.3.4 Future plaquette experiments

At the time this theses is being written, it is not completely clear yet which kind of experiment is going to be conducted once we are able to initialize the plaquette state reliably. The different options include:

- Studying the properties of a single plaquette by coupling it to a bath. Such a system has been studied theoretically in [62]. Based on a single-band Hubbard Hamiltonian with nearest and next-nearest neighbor hopping, this paper predicts the existence of a configuration with equal ground state energies for plaquette occupations of 2, 3 or 4 fermions. It is suggested that this quantum degeneracy plays a crucial role for the formation of d-wave superconductivity. Furthermore, the next-nearest neighbor hopping is considered to be an important ingredient: With t being the nearest and t' being the next-nearest neighbor hopping coefficients, the degenerate point occurs for $t'/t = -0.3$.
- Prepare two adjacent plaquettes with occupations $|2\rangle$ and $|4\rangle$ in their ground states and provide adequate tunnel coupling between the plaquettes. The system is proposed to exhibit Rabi oscillation between $|2, 4\rangle$ and $|4, 2\rangle$. The Rabi frequency would be a measuring tool for the binding energy of hole pairs. This experiment was proposed in [106].
- On a superlattice of plaquettes, in the pseudogap regime, observe the formation of pairs and their local ordering similar to what has been observed in solids [87]. From there, it should be feasible to reach a d-wave superfluid state. This was also suggested in [106] and this proposal does include some thoughts on experimental techniques and difficulties.

- In [107], the dynamics of plaquettes prepared in the RVB state has been studied using bosonic atoms in a superlattice to obtain a better understanding of the nature of the RVB state. One could repeat this experiment with fermions on a set of plaquettes. Upon enabling appropriate coupling between the plaquettes and choosing the doping correctly, such a doped RVB state is expected to form a d-wave superfluid.

Actually realizing these experiments where theoretical predictions exist will not be easy, but the goal is to extend the scheme to a level of complexity where things are less well understood. As an ultimate goal, one should think about experiments that are able to mimic phase-sensitive solid-state experiments like the ones described in Sec. 2.2. A superconducting ring made from plaquettes with appropriately chosen order parameters exhibiting a spontaneous supercurrent would be really impressive.

Chapter 3

The state of the art in quantum gas microscopes

In this chapter, I will give a brief overview of existing quantum gas microscopes and optical tweezer experiments, focusing on the different strategies of achieving single-site optical resolution and single atom sensitivity. Primarily, this serves to motivate our novel experimental approach with its in-vacuo objective presented in Chapter 4.

3.1 Optical fundamentals

There are many things that need to be specified for a full description of a lens system. Here, the terminology used to specify quantum gas microscope objective designs is introduced:

1. Numerical aperture (NA): This dimensionless number characterizes the range of angles (or k-vectors) accepted by a lens system. Assuming lenses in vacuum or air, it is given by

$$NA = \sin(\alpha) \tag{3.1}$$

where α is the maximum half-angle of a cone of light that can enter the lens. The NA determines the resolution and the light-gathering power of an imaging system.

2. Spherical lens systems: It is convenient to use spherical lenses as optical components as they can be manufactured accurately with very good surface qualities. Their drawback is that they suffer from spherical aberration and the effect becomes worse for larger NA. To reduce these aberrations, different combinations of spherical lenses have to be employed.

Usually, the lens combination is additionally optimized to achieve achromaticity over the desired wavelength range by combining positive and negative lenses made from different glasses.

3. Aspheric lens (AL): The spherical aberration introduced by spherical lenses can be compensated by shaping the lens surface aspherically instead. This allows for diffraction limited resolution up to high NA. The fabrication of non-spherical optical surfaces is more difficult than for spherical surfaces and the resulting surface qualities are generally poorer. Today, custom-made aspheric lenses with sufficient surface perfection are available. AL are good for local focusing of a single wavelength laser but they can neither provide a good field compensation nor color compensation without additional lenses.
4. Solid-immersion lens (SIL): In traditional light microscopy, the NA of the imaging system is often increased by putting an immersion liquid like water or oil in between objective and sample. The same effect can be achieved by inserting a hemispherical lens. As a side effect, the sample is required to be located very close to the surface of the SIL.
5. Infinity-corrected lens: A lens - or a system of lenses - is called “infinity-corrected” if it is optimized to focus collimated light. It can be thought of as a lens that images a point in the focal plane at an infinite distance.
6. Effective focal length (EFL): The introduction of an EFL is useful for lens systems that can not be approximated as a thin lens. It is the relevant focal length for determining the magnification of an imaging system.
7. Working distance: This is the distance from the object plane to the first part of the microscope objective.
8. Imaging system resolution: When considering two point-like light sources spaced by some distance d , the resolution of an imaging system is the minimum distance for which the two points can be distinguished.
9. Point spread function (PSF): The image of a point-like object is called the PSF.
10. Diffraction limit: If the aberrations introduced by a lens are small, the resolution is limited by diffraction. According to the Rayleigh-criterion, for given wavelength λ and NA , the resolution is given by

$$d = \frac{0.61\lambda}{NA} \quad (3.2)$$

11. Different criteria are used to specify whether aberrations are small enough for diffraction-limited imaging:

- (a) Rayleigh: Concerning spherical aberration, a lens is diffraction limited if the resulting peak-valley wavefront deviation is less than 0.25λ .
 - (b) Maréchal: Generalizing (a) to higher-order aberrations, a lens is diffraction limited if the RMS wavefront deviation is below 0.07λ .
 - (c) Strehl: This figure of merit is defined via the PSF of the system. It is given by the ratios of the maxima in the PSF with and without aberrations. Accordingly, a perfect lens has a Strehl ratio of 1. Other lenses are considered to be diffraction limited for values $S \geq 0.8$.
12. Field of view (FOV) : For an object that is not located on the optical axis, diffraction-limited imaging is only possible up to some maximum distance from the axis. The area defined by this radial distance is called FOV.
 13. Depth of field (DOF) : The maximum tolerable object displacement along the optical axis is called the DOF given by λ/NA^2 .

3.2 Design aspects of quantum microscopes

For objectives in quantum gas microscopes, it is particularly important to have a high NA, as it determines both the maximum resolution and atom detection efficiency. If the objective is used for imprinting light potentials as well - as in our case - the resolution is more important than in lattice-based experiments: With higher resolution, one can generate optical tweezers with higher trap frequencies which simplifies cooling schemes. In addition, one can reduce the tweezer spacing to provide higher tunneling rates between the individual traps. As a side effect of a high NA, the DOF is small. This is perfectly fine if flat systems are investigated. The FOV is important, but depends on the size of the physical system of interest. For a quantum gas microscope, a large FOV is more important than for a tweezer apparatus. Nonetheless, having an imaging system with large FOV is generally attractive, as it simplifies adjustments. Achromaticity at imaging and trapping wavelengths is helpful but not strictly required, as the different wavelengths generally follow different paths in the optics system and small focal shifts can be easily compensated.

Commercially available optical microscope objectives like the ones used in the life sciences are very good and provide a large NA with a large FOV and excellent color correction. But typically, they do not provide a large WD. The optical medium in between objective lens and object is crucial in this high-NA regime. The aberrations that are introduced by a vacuum window have to be compensated, either by taking the windows thickness and refractive

index into account when designing the objective lens, or by compensating the aberrations with some additional element. Different strategies to solve this problem have been developed, as described in Sec. 3.3. Another reason for requiring - compared to other light microscope applications - longer WDs is that trapping and cooling of our atomic samples typically relies on the ability to illuminate the atoms with laser beams not only through the objective lens, but also along perpendicular axes. For some applications, for example trapping the atoms in pancake-like two-dimensional traps, a non-negligible NA is required for these additional optical access ports. In principle, considerations of the NAs along different experimental axes do not put size constraints on the structure or in particular on the WD of the objective lens, as the NA is an angle-dependent figure. Practically, such constraints do arise from the complex arrangements comprising optical, vacuum and magnetic assemblies.

3.3 Currently operating quantum microscopes

In the last decade, we have seen tremendous progress of in-situ manipulation and probing of cold-atom systems. Different approaches have been demonstrated for both cooling and imaging techniques. A chronological list of quantum gas microscopes (sorted by publication date) including information on the key techniques is given in Tab. 3.1. For bosonic species, quantum gas microscopy was realized about five years earlier than for fermionic species as bosons can be cooled easily to form a BEC prior to lattice loading. Most of these experiments employ custom microscope objectives consisting of several spherical lenses. In some cases, the NA is boosted by using a solid-immersion lens (SIL). By this technique, the WD is drastically reduced, sometimes to just a few microns. The close spacing of the atoms to the surface of the SIL complicates perpendicular optical access, but can be exploited for trapping the sample in an evanescent light field. The fluorescence light used for in-situ imaging is generated as part of a laser-cooling process or by heating the atoms in a sufficiently deep lattice.

The apparatus used for optical tweezers are similar in most respects but they are typically not able to prepare sufficiently large atom numbers and densities for efficient evaporative cooling. Possible cooling processes include different polarization-gradient cooling (PGC) and Raman-sideband cooling (RSC) schemes as well as side-band Doppler-cooling using a sufficiently narrow transition. These all-optical cooling approaches pave the way to very short experimental cycle times as required for good statistics. A list of tweezer apparatus is presented in Tab. 3.2. As opposed to the apparatus presented in this thesis, all known tweezer apparatus with all-optical cooling techniques use bosonic species. Nonetheless, there does exist a fermionic tweezer apparatus in the group of S. Jochim and it produced groundbreaking results, in particular with

Group	Species	Cooling	Imaging $\lambda [nm]$	NA	WD	Realization	Reference
Greiner	^{87}Rb	Evaporation + molasses (in pinning lattice)	780	0.8	few microns	NA 0.55 objective + in-vacuo SIL	[108, 109]
Bloch	^{87}Rb	Evaporation + molasses (in pinning lattice)	780	0.68	< 13 mm	NA 0.68 objective	[110, 111]
Kozuma	^{174}Yb	Evaporation	399	0.81	few microns	NA 0.55 objective + SIL	[112, 113]
Zwierlein	^{40}K	RSC	770	0.87	8 μm	NA 0.6 objective + SIL	[9, 114]
Greiner	^6Li	RSC	671	0.87	10 μm	NA 0.6 objective + SIL	[10]
Kuhr	^{40}K	EIT cooling	770	0.68	< 13 mm	NA 0.68 objective	[11, 115]
Thywissen	^{40}K	EIT cooling	770	0.8	0.8 mm	NA 0.8 objective + thin window	[12, 116]
Gross	^6Li	Evaporation + RSC (in pinning lattice)	671	0.5	\approx 15 mm	NA 0.5 objective	[13, 117]
Takahashi	^{174}Yb	Evaporation + narrow-line Doppler	399	0.75	5.5 mm	NA 0.75 objective	[118, 119]
Meschede	^{133}Cs	Microwave Sideband Cooling	852	0.92	150 μm	Asphere + SIL, both in-vacuo	[120, 121]

Table 3.1: An overview of quantum gas microscopes that have published results with single-site resolution. For apparatus without in-vacuo imaging optics, the WD is measured from the vacuum window.

respect to the fermionic double-well [122]. The preparation technique applied in this apparatus is different: First, a degenerate Fermi gas of ^6Li is prepared by evaporation in an optical dipole trap, then 1064 nm tweezers are loaded with a small number of atoms. This procedure fills the tweezer ground state with a probability of almost unity but higher states are filled as well. To clear all states except for the ground state, a spilling technique is applied.

The different lens systems for quantum gas microscopes as well as tweezer apparatus are illustrated in Fig. 3.1 (apparatus without in-vacuo optics) and Fig. 3.2 (apparatus with in-vacuo optics). The optics arrangement presented in this thesis with the microscope objective inside the vacuum chamber is shown in Fig. 3.2d. This new approach is versatile as full flexibility concerning the optical specifications and a long WD combined with easy alignment is achieved. The fluorescence light collected from the atoms is collimated before

Group	Species	Cooling	Imaging λ [nm]	Tweezer λ [nm]	NA	Realization	Tweezer geometries	Reference
Jochim	^6Li	Evaporation	671	1064	0.6	NA 0.6 objective	1x1, 1x2, 1x3	[91, 122, 123, 124]
Regal	^{87}Rb	RSC, PGC	780	852	0.6	NA 0.6 objective	1x1, 1x2, 2x2, 10x10	[14, 15, 16, 19, 17, 18, 24]
Lukin	^{87}Rb	RSC	780	815	0.5	Asphere DW(780 nm) as vacuum window	1x1	[20, 125]
Lukin	^{87}Rb	PGC	780	809	0.5	NA 0.5 objective	1x50	[25]
Andersen	^{85}Rb	PGC, RSC	780	828	0.55	in-vacuo asphere	1x1	[126]
Kaufman	^{88}Sr	narrow- line Doppler	461	515	>0.65	NA >0.65 objective	3x3, 4x4	[21]
Endres	^{88}Sr	narrow- line Doppler	461	515	0.5	NA 0.5 objective	11x11	[22, 21]

Table 3.2: An overview of apparatus with optical tweezers. Except for the Regal apparatus ($WD \approx 15$ mm), figures on the WD are not known.

passing through the vacuum window, so the orientation of the microscope with respect to the window is not critical.

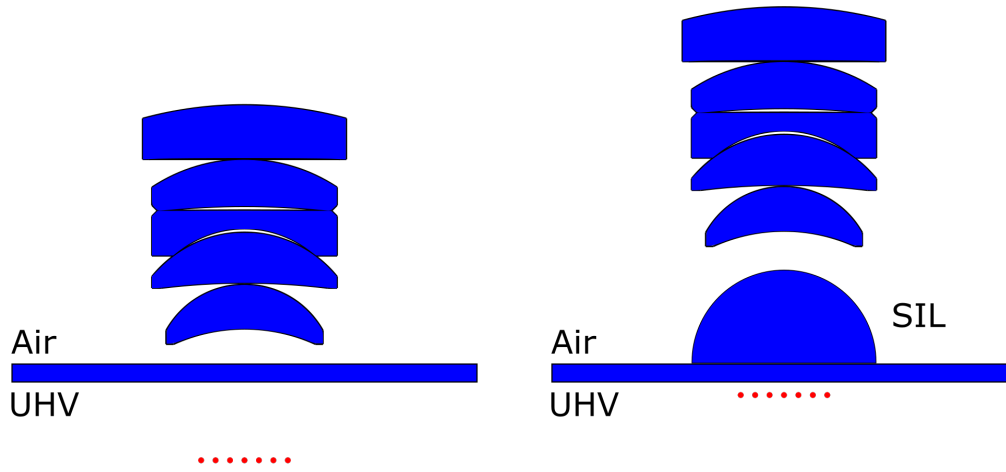
Three early tweezer experiments that are technically relevant should be mentioned:

- The first known work featuring a single atom in an optical tweezer has been performed in the Meschede group [127]. They trapped Cs atoms in a 1064 nm tweezer and used an in-vacuo lens¹ for focusing and detection. The loading procedure this experiment applied is very peculiar: A MOT containing a small number of atoms - down to one - is loaded from a very low background pressure. This MOT uses a large magnetic gradient to have the atoms reasonably well localized for reliable transfer to the optical tweezer.
- Around 2001 P. Grangier investigated the loading behavior of an optical tweezer and discovered that it is either empty or occupied by one atom but never occupied by more than one atom [128, 129, 130]. From the perspective of our new experiment, the apparatus Grangier used is particularly interesting, as it included two in-vacuo objective lenses (spherical

¹The lens type is not specified in the paper. Most likely, they used an asphere.

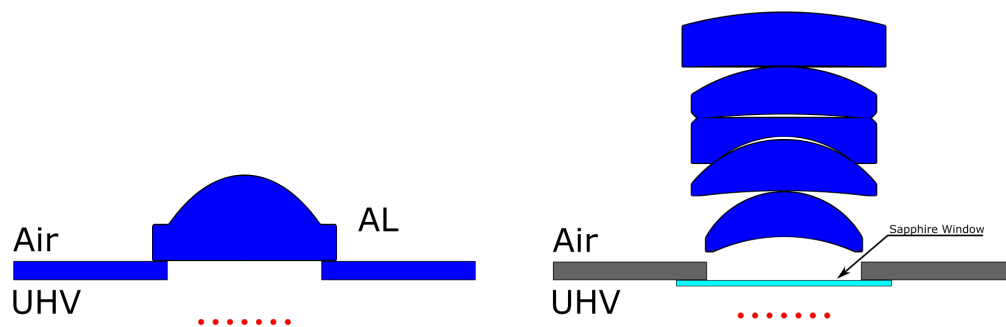
system) for creating the tweezer and imaging the fluorescence. As opposed to our apparatus, these objectives were used in a vacuum around 1×10^{-9} mbar. The apparatus used ^{87}Rb and 810 nm trapping light focused with a $NA = 0.7$ objective. Unfortunately, the publications cited above do not give many technical details, but some can be extracted from the doctoral thesis [131].

- Another early tweezer experiment in the group of M.F. Andersen around 2010 discussed studies on light-assisted collision-induced losses and how to exploit them to increase the probability of loading a tweezer with exactly one atom [23, 132, 133, 134]. It is very likely that we will be trying to adopt this loading technique. Andersen used an in-vacuo aspheric lens to achieve a high NA.



(a) Spherical lens system with long WD, often used in combination with glass-cell chambers.

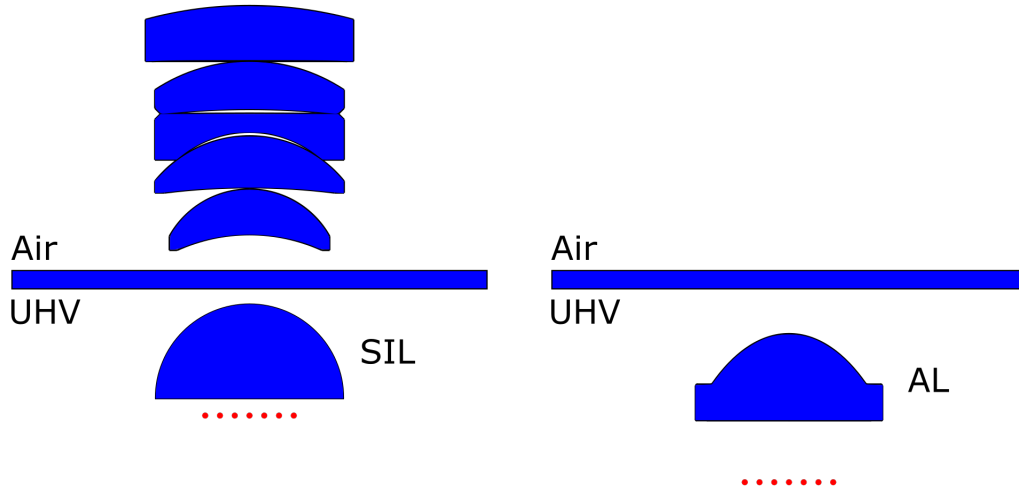
(b) Spherical lens system with NA-enhancement with a SIL optically contacted to the vacuum window. In this design, the atomic samples have to be located very close to the vacuum window. To bring the atoms to this location, some transport protocol is required.



(c) Aspheric lens glued to vacuum chamber serving as a vacuum window. This solution is rather simple if an adequate AL is available. Manufacturing a custom AL is expensive and the optical performance may be limited, in particular if a large FOV is required.

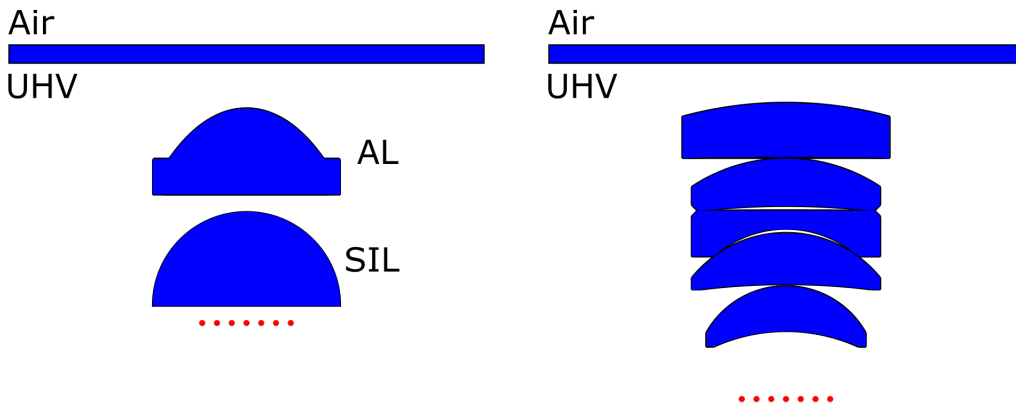
(d) A very thin vacuum window made from sapphire introduces fewer aberrations, reduces objective lens requirements and adjustment effort. In principle, this design is compatible with objective lenses for standard light microscopy.

Figure 3.1: Technical solutions for high-resolution imaging of atomic samples without in-vacuo optics. The object plane is indicated by red dots.



(a) A SIL located inside the chamber is used to increase the NA of an objective located outside the vacuum chamber.

(b) An aspheric lens located inside the chamber is an easy solution to achieve high NA at a single wavelength with a limited FOV.



(c) In [120], a NA of 0.92 is achieved using an aspheric lens and a SIL, both custom made and in-vacuo.

(d) The design presented in this thesis is based on objective lenses made up from spherical lenses inside the UHV chamber. This enables wide-range field and color correction without any necessity to ensure good alignment with respect to a vacuum viewport.

Figure 3.2: Technical solutions for high-resolution imaging of atomic samples with in vacuo optics. The object plane is indicated by red dots.

Chapter 4

Our new quantum gas microscope

In this chapter, the key concepts of the new apparatus are described. Selected technical details concerning important components are presented.

It begins with a short specification and a presentation of the experimental layout. Subsequently, the technical subsystems are presented. The different topics are ordered according to the chronology of the design and manufacturing process but they are strongly interconnected. Beyond providing a technical documentation of our apparatus, this is supposed to define design guidelines for future developments.

4.1 General experiment design

4.1.1 Choice of atomic species

Today, physicists are able to trap and laser-cool many atomic species, including ones with more exotic electronic structures. In our research group we concentrate on understanding the nature of fermionic quantum systems. The only species that combine fermionic quantum statistics with simple, hydrogen-like energy levels - favorable for laser cooling schemes - are ${}^6\text{Li}$ and ${}^{40}\text{K}$. Each of them has pros and cons: ${}^6\text{Li}$ is light, which means that it can tunnel easily through potential barriers, and can - in a magnetically controllable way - form bosonic molecules. ${}^{40}\text{K}$ is heavier and can be cooled more easily using laser cooling. It has a large nuclear spin and a rich hyperfine structure. Regarding technological difficulty, there exist no significant differences between the isotopes. The low natural abundance of ${}^{40}\text{K}$ is a problem in the sense that quite expensive enriched samples are required. In my opinion, the latter is more than compensated by the high vapor pressure of potassium. So unlike lithium, potassium atom sources can be operated at temperatures closer to

room temperature. This simplifies the design of the atomic sources and vapor cells.

We decided to develop a ^{40}K experiment because the use of laser cooling techniques instead of evaporation is crucial to us, as it enables short cycle times and does not rely on expensive high power laser systems.

4.1.2 Key design features of the apparatus

Considering the technical complexity of modern cold atom experiments, the actual specification of what we planned to build was not very detailed:

- The apparatus was supposed to be versatile and extensible.
- It should be suitable for performing experiments with fermions in optical tweezers. In addition, it should be capable of cooling samples of several 1000 atoms to quantum degeneracy.
- Imaging atomic quantum systems in real space requires single-site optical resolution. The optical resolution of the imaging system must be sufficient to place tweezers at small distances to achieve adequate tunneling rates.
- In measurements with only a small number of atoms, high cycle rates are essential to obtain good statistics.

4.1.3 Experimental geometry

Some general design considerations follow directly from the choice of the atomic species and the desired features. These particularly affect the choice of atomic source as well as the decision of whether to conduct the entire experimental sequence at a single location or to split it with the preparation at one location and the experiments at another. With some kind of transport being required, the latter introduces complexity and might slow down the sequence. On the other hand, this solution introduces flexibility and improves the optical access. With the decision for ^{40}K atoms, it was rather clear to use a 2D-MOT system as the atomic source. If adequate differential pumping is available between the 2D-MOT section and the rest of the vacuum system, a 2D-MOT can supply a sufficiently clean beam of ^{40}K atoms that can be captured in a MOT with adequate loading rates.

After capturing the atomic beam in a MOT, we aim to manipulate and image the atoms with high optical resolution. A microscope objective with high numerical aperture is required close to the atomic sample. In addition, applying a homogeneous magnetic field with some 100 G along the imaging axis is an

important feature for future experiments. These two constraints are incompatible with having the high resolution imaging system at the same position as a MOT with normally-sized MOT beams. In principle one pair of MOT beams could pass through the high resolution imaging system and be collimated at the trap position. But the size of these beams would be limited as would the MOT's capacity and the fraction of atoms collected from the 2D-MOT beam.¹ A small MOT would be tolerable in an apparatus designed for nothing more than experiments with optical tweezers. However, we do not want to be restricted to these kinds of experiments. Accordingly, we decided to have separate positions for the MOT stage and the rest for the experimental cycle, as shown in Fig. 4.1. The transport distance of 4 cm was chosen as the shortest

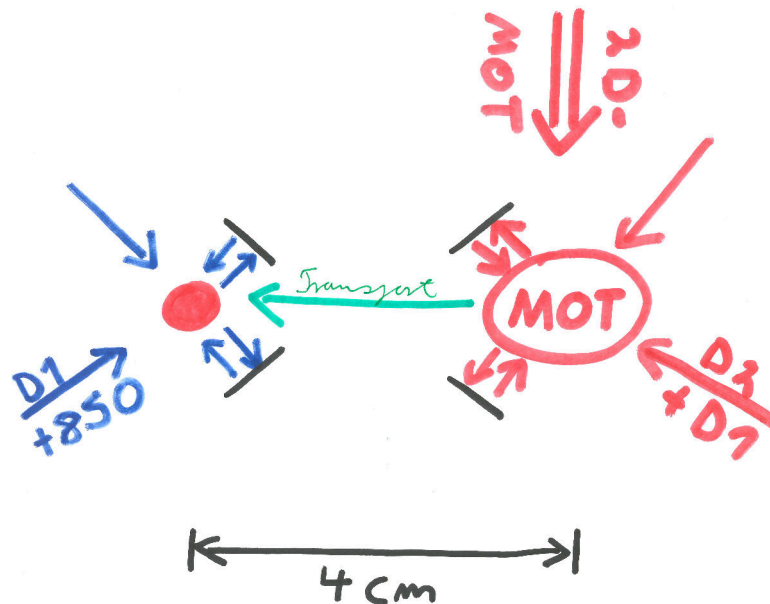


Figure 4.1: Basic idea of the experiment: An atomic beam enters from the 2D-MOT (not shown). The atoms are trapped in a MOT, sub-Doppler cooled using a D1 molasses scheme and afterwards transported to the position for experiments with high optical resolution. Here, D1 light is applied to load the atoms into far-detuned optical traps at 850 nm.

possible distance between the MOT position with $\varnothing 25$ mm and the microscope position with $\varnothing 35$ mm beams.²

It was decided at an early stage to locate the imaging optics inside the vacuum system. This decision is a trade-off: It adds some constraints to the design of the vacuum system and complicates the commissioning, but it makes the

¹A different solution to have a MOT at the position of the microscope had been developed in the Grangier group around 2000. They constructed a MOT with two pairs of beams meeting under 20° instead of 90° [131].

²These figures are given by the maximum beam diameters when using elliptical 1"-mirrors and circular 2"-mirrors.

adjustment of the optical system to achieve high resolution imaging much easier.

4.2 Vacuum system

Most modern physics experiments have to solve the problem of isolating the physical system of interest inside a vacuum system with a sufficiently low residual gas pressure. The development of vacuum technology is slow but still ongoing. Most of the vacuum equipment used in the field of ultracold atoms can be considered to be standard technology. Nonetheless, designing and manufacturing the vacuum systems for ultracold atom experiments often leads to problems and delays, as the typical requirements concerning base pressure, geometric constraints and optical access are at the limit of what is technically possible.

4.2.1 Requirements

4.2.1.1 Pressure requirements

The background pressure in the region where experiments take place has to be sufficiently low that collisions between cold atoms and residual gas molecules are unlikely on the relevant time scale. From experience gathered in other ultracold gas experiments, we know that an atom lifetime of about 100 s defines good operational conditions. Such a lifetime corresponds to pressures around 1×10^{-11} mbar, residual gas densities of about $1 \times 10^5 \text{ cm}^{-3}$ and mean free paths of some 1000 km. The connection between measured pressure and measured atomic lifetime is not easy to understand in detail, as both the technical pressure measurement and the effect of the residual gas on the atomic sample strongly depend on the chemical composition of the residual gas. Usually, the residual gas in a clean, baked UHV system is mainly hydrogen. In our apparatus, we were not able to measure the mass spectrum of the residual gas due to lack of corresponding instrumentation.

A challenge for achieving the required low pressures is that in the first step of each experimental cycle, the atoms are loaded from a thermal potassium source. To achieve an acceptable loading rate, one needs a relatively high partial pressure inside the potassium source section. Hence, the source must be well separated from the UHV experiment section via a differential pumping stage.

4.2.1.2 Geometrical requirements

It follows from general design considerations that the vacuum system has to fulfill the following requirements:

- The volume inside the chamber must be sufficient for a MOT with up to 1" beams, a high resolution imaging system, a radio-frequency antenna and a microwave antenna.
- Good optical access to MOT position as well as the experiment position. Light entering the chamber from one side should be able to leave on the other side. Hence, each viewport has a partner on the other side of the chamber.
- The height of the chamber has to be minimized to locate the main magnetic coils as close as possible to the atoms.
- The diameter of the chamber should not be too large so that auxiliary imaging systems and dipole traps with adequate resolution can be used.
- The distance from the 2D-MOT atomic source to the MOT position should roughly fit to the expected divergence of the atomic beam and the size of the MOT beams.
- Vacuum equipment attached to the chamber should not limit the possibilities for manipulating and observing the atoms.

From vacuum considerations, the following additional conditions arise:

- The internal surface area of the chamber should be small.
- The surface coated by the titanium sublimation pump (TSP) should be as large as possible.
- The vacuum conductivities except for the differential pumping connection between the main chamber and the 2D-MOT should be maximized.

4.2.1.3 Additional requirements

- All components, especially in the region close to atoms, should be non-magnetic.
- Baking the UHV components at 200 °C should be facilitated.
- As the microscope lens assembly is not fully bakeable, it should be possible to easily insert the lens while flooding the chamber with pure argon.

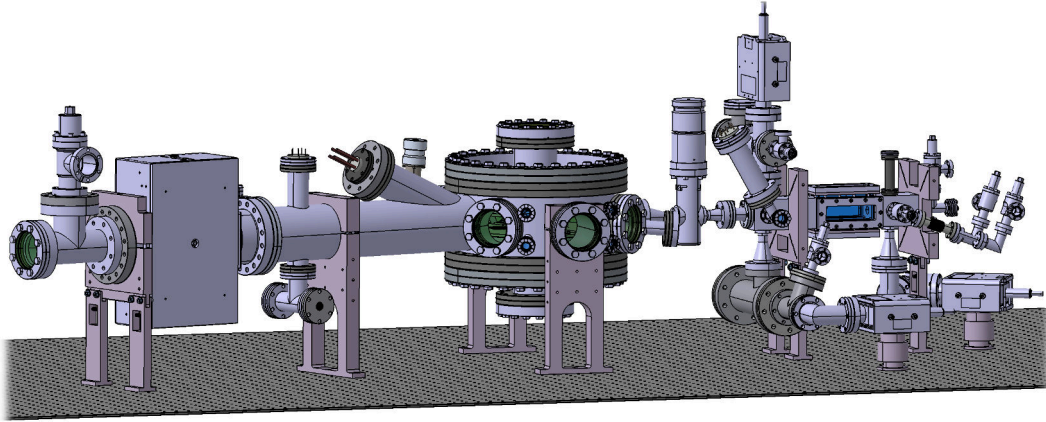


Figure 4.2: The complete vacuum system on a $3.6\text{ m} \times 1.5\text{ m}$ optical table. From left to right: Pump section with ion pump, pressure gauge and TSP - main chamber with in-vacuo objective lens - valve, shutter and differential pumping stage - 2D-MOT section.

4.2.2 Final design

The complete vacuum system shown in Fig. 4.2 has three sections:

- 2D-MOT source with a differential pumping stage and an atomic beam shutter
- Main vacuum chamber, with the optical imaging system
- Pumping stage to achieve UHV conditions in the main chamber

2D-MOT section and main chamber are connected via an all-metal gate valve³ to allow maintenance on the 2D-MOT part without venting the entire system.

4.2.2.1 2D-MOT chamber

We decided to use an improved version of the 2D-MOT that was developed by Thomas Ühlinger in Zurich some years ago [135]. The chamber⁴ consists of a steel frame to which four rectangular windows are attached with indium wire seals. As potassium atoms prefer to stick to stainless steel walls, we have aimed at reducing the steel surface inside the chamber. That was achieved by reducing the chamber's size compared to [135]. CF16 instead of CF40 flanges were used.

Ports are necessary for

³VAT 48124-CE01

⁴The complete 2D-MOT vacuum system is shown in Fig. 4.8.

- pumping.
- attaching potassium samples.
- inserting an in-vacuo shutter to interrupt the atomic beam.
- attaching the 2D-MOT to the main chamber.

The corresponding flanges have been machined directly in one large piece of stainless steel including the differential pumping section as well as a mirror surface that was intended for use in a 2D⁺-MOT configuration. By producing the interior of the chamber monolithically, the risk of virtual leaks is reduced. To achieve a sufficiently high vapor pressure in the 2D-MOT chamber without

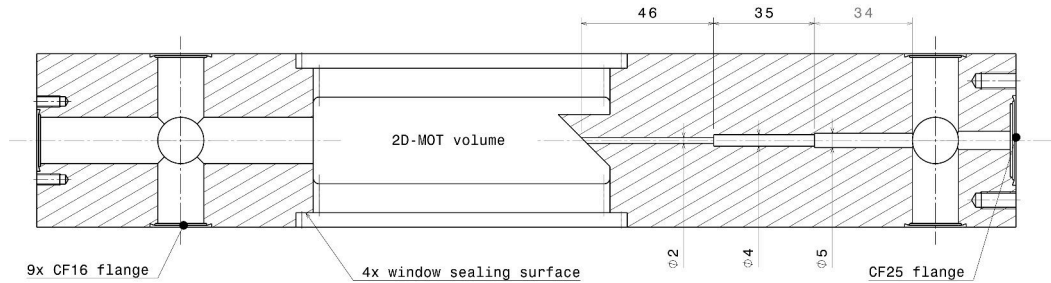


Figure 4.3: A section view through the monolithic steel 2D-MOT chamber. Several CF16 flanges can be used for attaching pumps, metallic samples and auxiliary equipment. Large rectangular viewports provide optical access to the 2D-MOT volume. The diameters of the differential pumping section are indicated.

impairing the vacuum in the main chamber, the differential pumping section has to be considered carefully. For air at room temperature, the conductivity of a straight pipe with diameter d and length l is - in the molecular flow regime - approximately given by

$$C = 120 \text{ m/s} \frac{d^3}{l}$$

Like other physical conductivities, the reciprocals are added:

$$\frac{1}{C} = \frac{1}{C_1} + \frac{1}{C_2} + \frac{1}{C_3}$$

With the dimensions given in Fig. 4.3, the conductivity of the differential stage is $C = 1.8 \times 10^{-5} \text{ m}^3 \text{ s}^{-1}$. This conductivity can be used for calculating the pressure ratio between the vapor cell side of the 2D-MOT and the UHV side given by

$$\frac{P_{2D}}{P_{UHV}} = \frac{S}{C}$$

where S is the pumping speed applied on the UHV side. In this estimate, the vapor cell is only pumped through the differential pumping stage. All other

pumps are disabled, which is also valid during normal machine operation. It is not easy to give an accurate figure for the pumping speed S . The UHV side of the 2D-MOT chamber is equipped with two 10 L s^{-1} ion pumps and a TSP. In addition, this part of the chamber is also pumped from the main chamber. If one assumes $S = 20 \text{ L s}^{-1}$, the pressure ratio is

$$\frac{P_{2D}}{P_{UHV}} \approx 1000$$

To estimate the potassium vapor pressure required for achieving sufficiently high MOT loading rates, knowledge of the capture rates of both 2D-MOT and MOT and the probability for an atom being transported successfully through the differential pumping tube would be needed. However, such an estimate would not be very practical, as we are not able to measure the potassium partial pressure. But we can extract the information that it is possible to have a useful potassium 2D-MOT with vapor pressures of about $1 \times 10^{-7} \text{ mbar}$ from [135]. As can be seen in the vapor pressure curve Fig. 4.4, the vapor pressure is only about $1 \times 10^{-8} \text{ mbar}$ at room temperature.

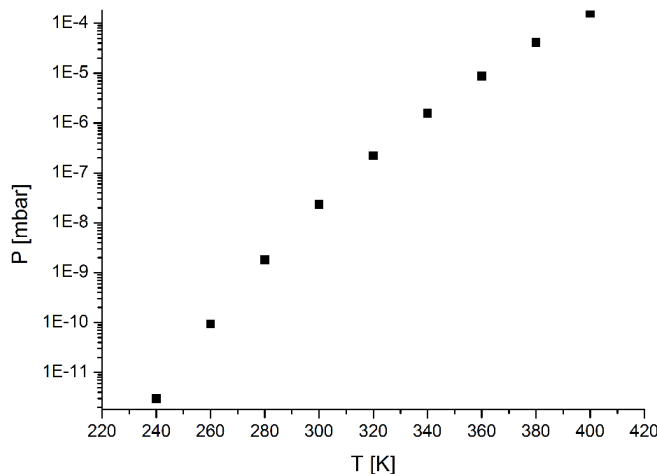


Figure 4.4: Vapor pressure of potassium in the relevant temperature range based on data taken from [136].

From these figures one might conclude that the differential pumping is insufficient to diminish the potassium vapor down to the $1 \times 10^{-11} \text{ mbar}$ range within the main chamber. But the estimate did not take into account the reduced conductivity for potassium due to its greater atomic weight (compared to air) and the property that this metal likes to stick to cold surfaces.

In the vacuum section between the differential pumping stage and the gate valve, we have included a mechanical shutter to be able to block the atomic

beam reliably. This might be useful if one should ever do experiments at the MOT position that rely on long lifetimes. We did not use this shutter so far in our experimental cycle, but it works and is technically interesting, because it uses a vacuum-compatible stepper motor⁵. It is shown in Fig. 4.5. Usual techniques for atomic beam shuttering employed in cold atom apparatus are based on “wobble sticks” or rotational feedthroughs that transmit the rotation magnetically.

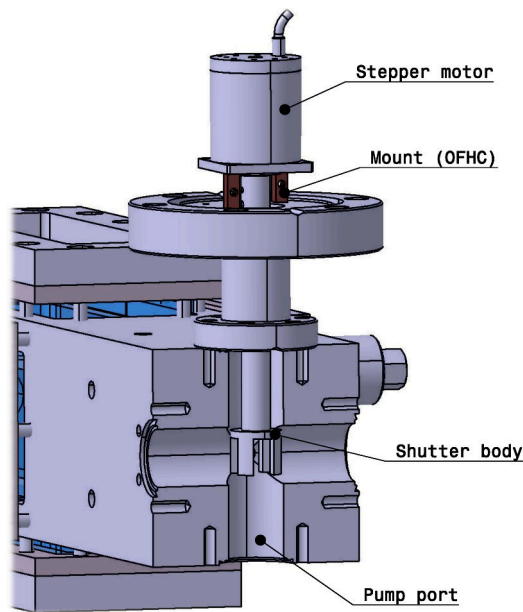


Figure 4.5: Section view of the shutter in the 2D-MOT chamber. The stainless steel shutter body is attached to the shaft of the in-vacuo stepper motor. The stepper motor is attached to a CF40 flange with vented screws.

4.2.2.2 Main chamber

It was decided that stainless steel and CF flanges should be used for the main vacuum chamber. This choice was closely connected to the decision to have two objective lenses inside the vacuum chamber and a MOT loading position which is spatially separated from the measurement position.

This approach has the following advantages:

- CF sealed steel chambers are standard technology.
- CF seals as well as viewports and electric feedthroughs with standard glass-to-metal and ceramic-to-metal connections are reliable and comparably insensitive to mechanical stress and thermal cycling.

⁵Phytron VSS 25.200.1,2-UHVG-4Lp

- Viewports with high optical quality are available.
- Mounting components inside the chamber is easy.
- The imaging optics can be easily installed after bakeout by removing one of the viewports.

Disadvantages associated with stainless steel chambers include:

- The chamber must be baked to reduce outgassing.
- Stainless steels can become permanently magnetized. This is usually not specified in material datasheets, as it depends on the microstructure of the material which can be changed by mechanical or heat treatment.
- When using standard viewports the optical coating is imperfect close to the edge of the glass. The full aperture of the window can not be used.
- Stainless steel has a specific resistance of typically $0.75 \Omega \text{ mm}^2 \text{ m}^{-1}$. Copper - which is used as gasket material - has only about $0.02 \Omega \text{ mm}^2 \text{ m}^{-1}$. Accordingly, eddy currents will be induced when magnetic fields are altered. These can exist for over 10 ms (more detailed analysis given in 4.3.7 on page 69).
- CF flanges take up space. Since metal gaskets are used, the flanges must withstand significant forces without deformation. Bolt heads consume additional space. Smaller viewport to atom distances could be achieved by employing other sealing techniques.

The lithium experiments used in Zurich [137] and Hamburg [138] served as a starting point for the main chamber design, as their geometry is very similar to what is needed in this potassium experiment. These chambers have a base flange size of CF250 (12"CF). In the horizontal plane, optical access is mainly provided by three axes with CF40 (2.75"CF) viewports. Essentially, the new chamber described here is an enlarged version of the lithium chamber. The components we used, in particular the viewports, pumps, gauges and valves, are equivalent. This approach was chosen to reduce the risk of incurring time-consuming vacuum problems.

In the following paragraph, I will explain how the chamber had to be scaled to provide enough space inside the chamber as well as suitable outer dimensions for positioning the magnetic coils: The base diameter of the chamber is primarily determined by the size of the magnetic coils that have to be placed around the chamber and are in re-entrant flanges to be close to the atoms. We had decided to use a magnetic transport of about 40 mm between the MOT and the experiment position. As this transport should be performed in a rather

high magnetic gradient of about 100 G cm^{-1} , this could only be achieved by using two large pairs of quadrupole coils which are displaced by the transport distance.⁶ Accordingly, our chamber size had to be increased from CF250 to CF300 (14"CF). This is illustrated in Fig. 4.6. For MOT beams, imaging sys-

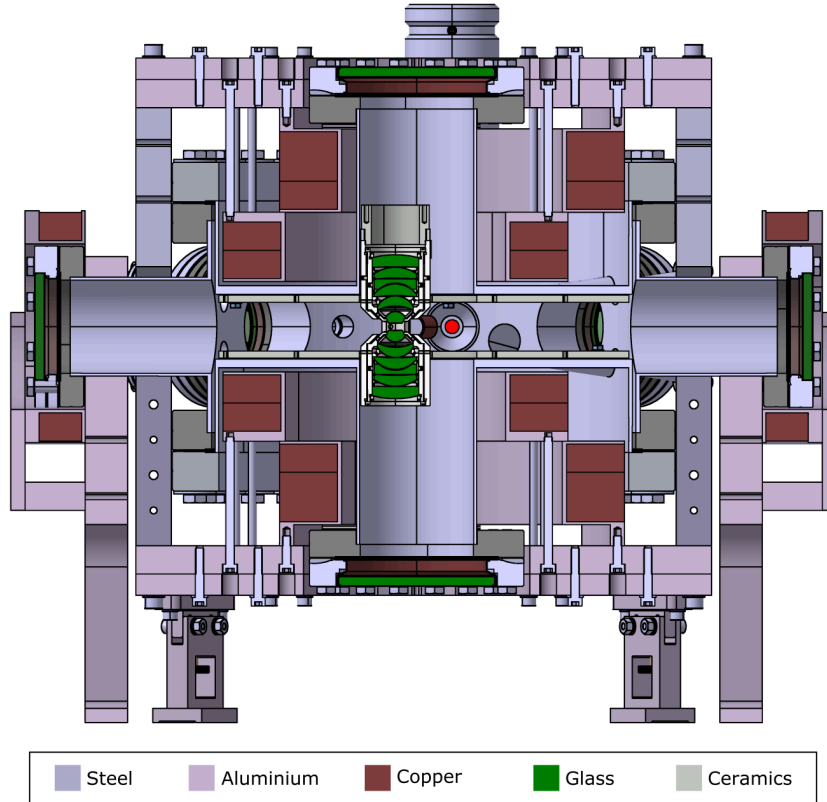


Figure 4.6: Cross-sectional view of the key experiment components. The experiment has two pairs of large hollow-wire coils. One is an almost perfect Maxwell coil (providing a quadrupole field with vanishing higher-order derivatives) centered around the MOT position, the other pair is in an almost perfect Helmholtz configuration centered around the microscope assembly. This illustrates the need for a large diameter vacuum chamber with re-entrant flanges.

tems, lattices, etc. good optical access in the horizontal plane at both MOT and experiment position is essential. In the axes oriented at 45° to the transport axis, the center distance between the beams addressing the MOT and the experiment position is about 30 mm. Hence, the maximum diameter of the respective beams at the viewport is about 20 mm and a CF63 (4.5"CF) viewport is a good choice for these axes. Along the vertical axis, one has MOT light as well as the light passing through the microscope assembly. The spacing of both is 40 mm and the diameter of the beams passing through the lens assembly was chosen to be about 30 mm so that 2" mirrors could be used. Accordingly, one

⁶Alternative options are discussed in 4.3.3 on page 60.

needs to have CF100 (6"CF) viewports along the vertical axis. The resulting flange geometry in the horizontal plane is shown in Fig. 4.7.

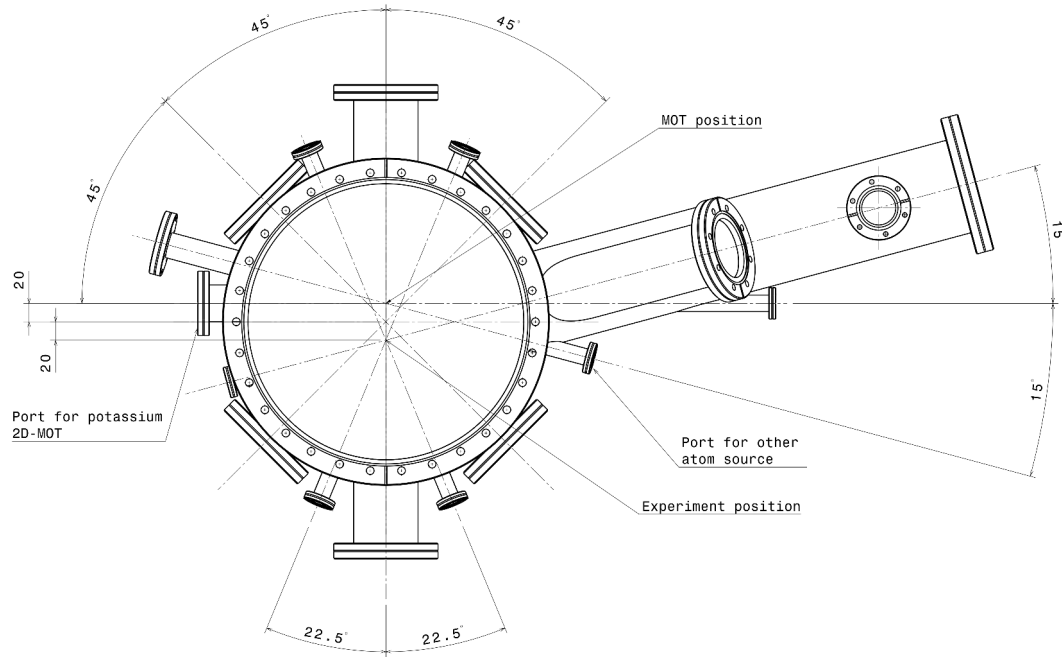


Figure 4.7: Flanges of our vacuum chamber. The base flange is CF300. Six CF63 flanges provide good optical access in the horizontal plane. The 100 mm pipe is for vacuum pumping.

In principle, it is possible to estimate the base pressure of a vacuum system if one has knowledge about the surface areas, outgassing rates of the materials, pumping speed and conductances. I will present such an estimate in 4.2.2.3. Nonetheless, I regard such an estimate to be rather unreliable. Outgassing rates are not that well known as they strongly depend on the treatment of the material and in addition the pumping rate is not well-defined as it depends on the residual gas composition and the area coated by the TSP. What we did instead prior to building the chamber was a very rough comparison between our vacuum system and others that are known to reach a sufficiently low pressure: The surface area inside the vacuum system scales with the second power of its size. The ratio of the surface areas inside the chamber used in this new experiment (K) compared to the one in the lithium experiment (Li) is approximately given by the sizes of the base flanges

$$\frac{A_K}{A_{Li}} \approx \left(\frac{300}{250}\right)^2 = 1.44$$

Even if one would consider our ^{40}K chamber to be pumped exactly like the ^6Li chamber, a pressure increase by a factor of 1.44 would not be catastrophic. In

fact, our chamber will have a higher pumping speed as the conductance to the ion pump and the area of the titanium-coated surface are both larger.

4.2.2.3 Pumps

In the final state, the entire vacuum chamber is pumped by four ion pumps and two TSPs. The 2D-MOT chamber has three small ion pumps⁷. They have a nominal pumping speed of 10 L s^{-1} and are equipped with conventional titanium pumping elements. As the ion pumps use neodymium magnets, they are relatively compact. One has to remove the magnets when baking, as neodymium magnets lose magnetization above 80°C . The three ion pumps fulfill the following tasks:

- Pump the vapor pressure part of the chamber prior to breaking the potassium ampule. The ion pump is attached to the chamber via a metal seal valve. Normally the valve is closed to avoid losing valuable potassium.
- The conductance between the part of the chamber where the stepper motor is located and the rest of the shutter section is very small due to the shutter blocking most of the aperture of the CF40 connection. This part of the chamber has its own ion pump.
- One ion pump pumps the shutter section.

The vapor cell and shutter section ion pumps are connected to the chamber with conical reducer nipples⁸ having a conductance of about 11 L s^{-1} . A standard CF40-CF16 straight reducer nipple has a length of 7 cm and a conductance for air in the molecular flow regime of only 7 L s^{-1} , so they would limit the pumping speed.

Figure 4.8 shows the locations of the pumps and the other components of the 2D-MOT .

To ensure sufficient pumping in the shutter section, we placed a TSP directly underneath the shutter. This TSP coats the surfaces of the shutter and the vacuum chamber around it as well as the complete surface inside the conical reducer nipple with titanium.

The main chamber is pumped by an ion pump with a nominal speed of 100 L s^{-1} equipped with “differential” pumping elements⁹ and with a TSP with three filaments. The main task of the ion pump is to reduce the partial pressure of noble gases, as these are not pumped at all by the TSP. “Differential” ion pump elements have an improved capacity for noble gases and reduced risk of

⁷Gamma Vacuum 10ST-CV-2H-SC-N-N

⁸Lesker CRN275X133

⁹Gamma Vacuum 100L-DI-6D-SC-N-N

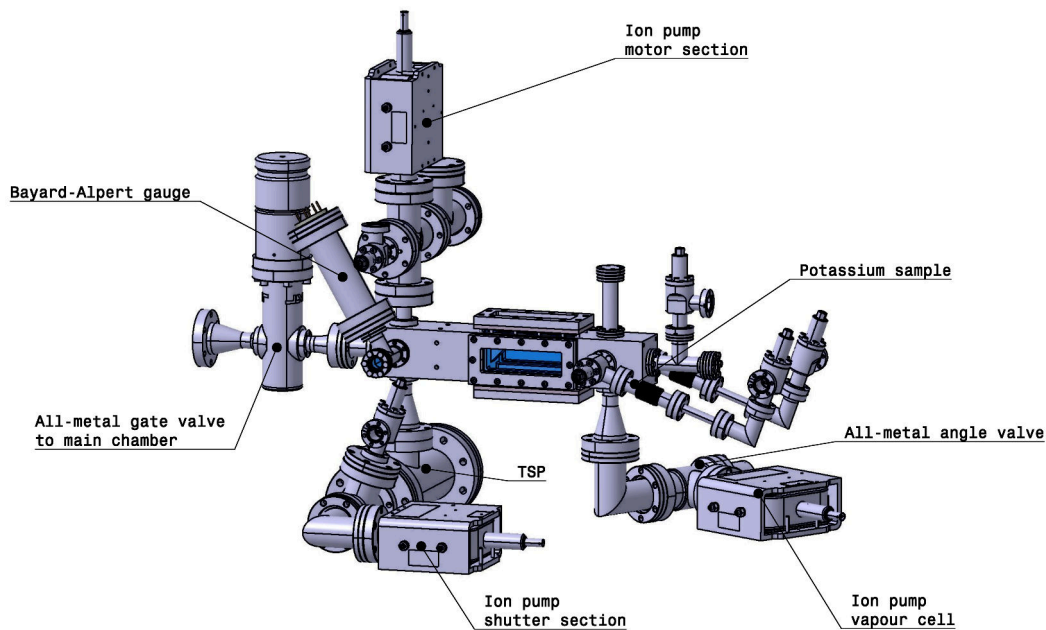


Figure 4.8: Illustration of the 2D-MOT vacuum system.

“argon instability”. As a trade-off, their pumping speed is reduced to about 80% compared to “conventional” elements. “Conventional” pump elements are 100 % titanium, whereas “differential” elements have 50 % titanium and 50 % tantalum. Tantalum has a reactivity similar to titanium, but larger atomic weight and different scattering properties enabling the pump to trap noble gases more reliably.

The TSP coats a surface of about 1000 cm^2 . The typical pumping speed per surface area for molecular hydrogen at room temperature is $2 \text{ L s}^{-1} \text{ cm}^{-2}$. Accordingly, the pumping speed for molecular hydrogen is about 2000 L s^{-1} . As the TSP defines the largest pumping speed in our vacuum system, it was a crucial design criterion to maximize the surface area coated with titanium. The solution is shown in Fig. 4.9. We have mated a CF63 pipe and a CF100 pipe under an angle of 25° so that in the vicinity of the TSP both pipes are coated with titanium. In addition, we have chosen the position of the TSP such that it has a straight line of sight to parts of the lower re-entrant flange while avoiding the risk of coating parts of the microscope assembly with titanium.

The main chamber has a steel surface of about 7500 cm^2 . Giving figures on expected outgassing rates is hard, as these depend on exact surface and temperature treatment. But the topic is technologically relevant and has been studied quantitatively. In [139], the outgassing rate for molecular hydrogen for a 304L stainless steel chamber without further surface treatment (such as electropolishing) after baking to 400°C , venting, re-evacuating and baking to 150°C is about $1.5 \times 10^{-13} \text{ mbarL/s/cm}^2$. The vacuum preparation and

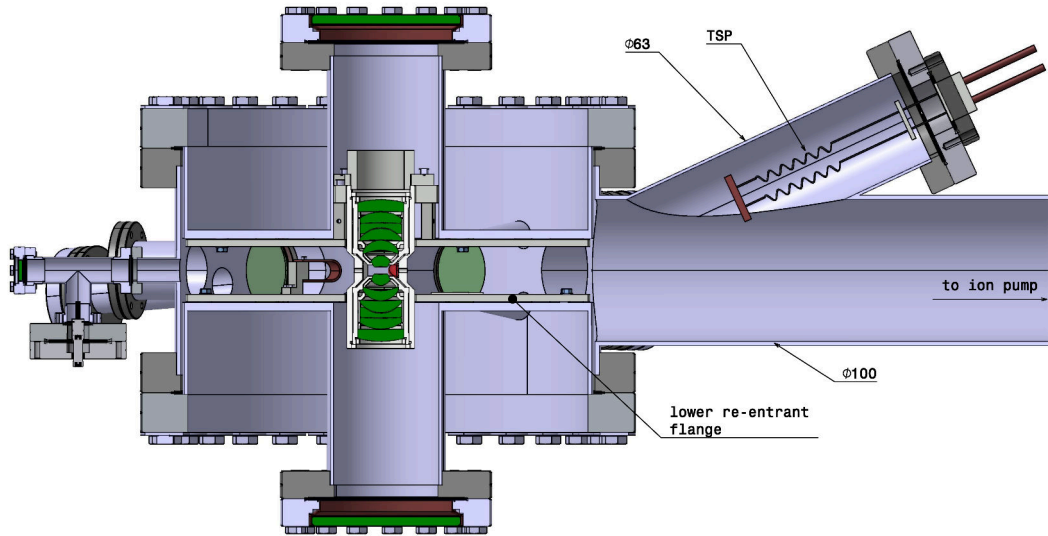


Figure 4.9: Cross-sectional view along the “pump” axis of the main chamber. The position and orientation of the TSP filaments have been optimized to maximize the area coated with titanium.

bakeout described in this paper is very similar to what we have been doing. Besides stainless steel, the vacuum system contains large amounts of fused silica and MACOR[®] ceramics. Both materials have low outgassing rates and zero porosity. So provided they are clean, they can be neglected.

With the assumed pumping speed for the TSP and the outgassing rate from the steel surface area, one obtains a base pressure in the chamber of

$$P = \frac{\text{OutgassingRate}}{\text{PumpRate}} = 5.6 \times 10^{-13} \text{ mbar}$$

4.2.2.4 Arrangements for in-vacuo devices

Both re-entrant flanges are equipped with four pins carrying M4 threads. These pins are welded to the baseplates of the flanges. On recommendation of our vacuum supplier, we chose a wall thickness of 6 mm for the baseplates. Otherwise the chamber would not be stable enough under a pressure difference of 1 bar.

Vacuum chambers are typically manufactured with mechanical tolerances that are large compared to the ones in optomechanical assemblies. Typically, the mechanical tolerances are in accordance with DIN ISO 2768-m. For the dimension of our chamber, this means length tolerances of ± 0.3 mm and angular tolerances of $\pm 0.3^\circ$.

4.2.3 Manufacturing and commissioning

I do not give a fully detailed report of my lab work on the vacuum system here, but restrict myself to selected topics.

4.2.3.1 Vacuum cleaning procedures

Two different cleaning strategies were used. Vacuum parts that were delivered in a UHV clean state were cleaned again as follows:

- wipe with acetone and pure cotton
- wipe with isopropanol and pure cotton
- clean from dust with clean dusting gas

Parts that have been manufactured or changed by us - including all of the mechanical parts in the microscope - have been treated with a more elaborate cleaning procedure:

- bath in deionized water + soap for at least 24h
- bath in deionized water
- bath in deionized water + acidic cleaner¹⁰ for at least 24h
- bath in deionized water
- bath in deionized water + alkaline cleaner¹¹ for at least 24h
- bath in deionized water
- bath in 99.5% acetone for at least 24h
- bath in 99.9% isopropanol for at least 24h

All parts that were small enough to fit into our ultrasonic bath have been cleaned for several minutes in addition to the steps listed above. Finally, all parts were baked under vacuum at temperatures above 200 °C.

¹⁰Elma Clean 60

¹¹Carl Roth Ultrasonol 11

4.2.3.2 Pumping and leak testing

During commissioning, our vacuum system was pumped using a 80 L s^{-1} turbomolecular pump¹² backed by an oil-free scroll pump¹³. As the vacuum system is not intended to be vented once the work is finished, the turbo pump is not permanently connected. We connect it to one of the all-metal angle valves whenever necessary.

Two leak testing techniques have been applied successfully in the course of this work:

- Helium leak testing using a leak tester that is connected to the turbo pump. This is not the best way to do helium leak testing, a mass spectrometer located inside the vacuum chamber would be much better.
- Leak testing by pouring acetone on potential leaks and looking for pressure changes. If the acetone hits a leak, this leads to falling pressure in most cases. In some cases, the pressure rises.

I would suggest that the sensitivity of both techniques is similar. If I detected a leak with helium I was also able to detect it with acetone.

4.2.3.3 2D-MOT rectangular viewports

Our workshop manufactured the monolithic 2D-MOT chamber from a 1.4404 (AISI 316L) stainless steel rod. Most of the shaping was done by wire electrical discharge machining. Afterwards, the interior as well as the window sealing surfaces were electropolished¹⁴ in order to reduce the effective surface. The chamber was baked to a temperature of $300 \text{ }^\circ\text{C}$ under high vacuum conditions.

A crucial step when commissioning the 2D-MOT was to attach the four rectangular glass plates to the steel body. Using indium¹⁵ wire, this is a well known standard technique, but we aimed to achieve bakeability to higher temperatures. The idea to use lead¹⁶ wire instead of indium wire for the window seals was inspired by the work of T. Petelski [140].

Like Petelski, we used high purity $\varnothing 0.5 \text{ mm}$ lead wire¹⁷. The wire was squeezed between the steel frame and the window glass spreading to a width of about 2 mm . At first, it seemed easy to use lead as a sealing material - making it leak tight was no issue. During bakeout, leaks opened and did not close when ramping the temperature down. These leaks could be fixed by compressing the

¹²Pfeiffer Vacuum HiPace 80

¹³Varian SH110

¹⁴Performed by Vakuu-Anlagenbau GmbH, Elmshorn.

¹⁵Indium has a melting temperature of $157 \text{ }^\circ\text{C}$.

¹⁶Lead has a melting temperature of $327 \text{ }^\circ\text{C}$.

¹⁷Sold by Advent Research Materials Ltd.

lead wire a little further, but in subsequent bakeouts windows (fused silica) broke.

We have tested several things to get rid of this problem without success:

- increased window thickness
- increased lead wire diameter
- make the “flanges” that exert the pressure on the window more stable for more uniform sealing

After some time we decided to use indium seals and N-BK7 instead of fused silica windows. A possible cause of the problem could be the low thermal expansion of the fused silica windows of about $0.5 \times 10^{-6} \text{ K}^{-1}$ which is much less than $16 \times 10^{-6} \text{ K}^{-1}$ for 1.4404 stainless steel.

In the final configuration, we have used 99.99%, $\varnothing 0.7 \text{ mm}$ indium wire¹⁸ in combination with N-BK7/H-K9L viewports of thickness 10 mm. This material has a coefficient of thermal expansion of $7.5 \times 10^{-6} \text{ K}^{-1}$ which is much closer to the value of stainless steel. After roughing and several days bakeout at $100 \text{ }^\circ\text{C}$, the vapor pressure side of the chamber reached a pressure of about $5 \times 10^{-9} \text{ mbar}$ as derived from the ion pump current. In this new configuration we did not have problems with windows breaking after thermal cycling. Unfortunately, one of the viewports¹⁹ leaked after bakeout. As we do not have a groove on our sealing surfaces into which the indium wire can be put, it is difficult to renew the seal on a vertical viewport. The leak was cured using Vacseal without thermal annealing. The leak did not show up again over the past three years.

4.2.3.4 Preparing the main chamber vacuum

The CF300 main chamber has been produced from 1.4404 (AISI 316L) pipes and 1.4306 (AISI 304L) flanges by a local vacuum company²⁰. All surfaces have been blasted with fine glass beads. Our first task was to ensure that the vacuum system without in-vacuo devices can be pumped to a sufficiently low pressure. We conducted the following steps:

- All flanges of the chamber were closed with blanks and it was baked at $400 \text{ }^\circ\text{C}$ for one week while evacuated using the turbo-molecular pump.
- After venting the chamber with air, the following components were installed: Ion pump, Bayard-Alpert pressure gauge, titanium sublimation pump, electric feedthroughs and all-metal angle valve

¹⁸Sold by CMRdirect.

¹⁹The leaky viewport was the one where the horizontal 2D-MOT beam enters the chamber.

²⁰Vakuum-Anlagenbau GmbH, Elmshorn

- Repeated runs of baking at about 250 °C for several days and leak testing until the chamber was leak-tight
- Repeated degassing runs of the TSP filaments and the pressure gauge filaments
- Repeated runs of the “HighPot” function of the ion pump controller to clean the ion pump elements
- Run TSP at maximum rated current of 50 A for some minutes
- At this stage, the lowest pressure we have ever observed on the UHV gauge was 4×10^{-12} mbar. We never achieved such a low pressure measurement afterwards.
- Add all viewports, bake at about 170 °C for three days
- Run TSP and perform extensive leak test. Lowest pressure observed at this stage was 5×10^{-11} mbar. Discovered leaks on one CF63 viewport (out of 7) and one CF16 viewport (out of 9).

At this stage we were confident that our vacuum system would be good enough after replacing the viewports and decided to do this when installing the chamber interior.

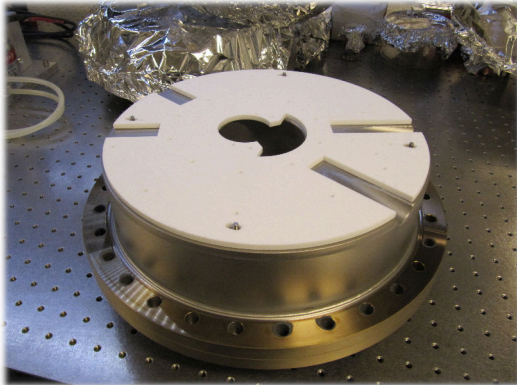
4.2.3.5 Installing the chamber interior except microscope assembly

In March 2016 the following components were installed:

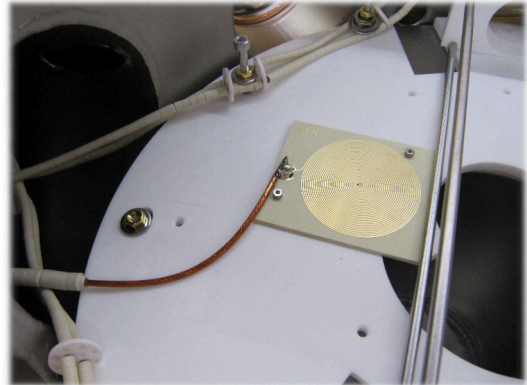
- Two large MACOR[®] plates serving as mounts for all other components. They are connected directly to the CF300 re-entrant flanges using washers and nuts. One of them is shown in Fig. 4.10a. Manufacturing these components from a non-conducting and non-magnetic material was essential to reduce eddy currents and vibrations.
- The microscope mounting structure
- A coil with 31 turns based on a printed circuit board serving as an antenna for radio frequency signals, shown in Fig. 4.10b. It will be used for driving transitions between m_F -states. This antenna geometry has been developed in the course of the bachelor thesis [141]. The antenna is connected via a Kapton-isolated 50Ω coaxial cable and an SMA feedthrough.
- A microwave antenna, shown in Fig. 4.10c. The design was inspired by [142]. It is connected via a Kapton-isolated 50Ω coaxial cable and an SMA feedthrough and is used to drive transitions between $F = 9/2$ and $F = 7/2$ hyperfine states.

- Four high-voltage electrodes. These were to be used in a possible extension of the apparatus for experiments with NaK molecules that would rely on the ability to orientate the molecules in an external electric field.

Figure 4.10d shows a picture of the apparatus prior to closing the chamber.



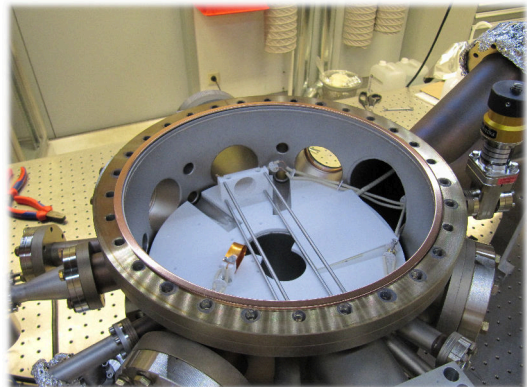
(a) MACOR[®] ceramic mounting plates are attached to each re-entrant flange. Washers have been placed between the steel and the ceramic surface in order to avoid virtual leaks.



(b) The printed-circuit board radio frequency antenna is connected to a Kapton isolated coaxial cable.



(c) Microwave antenna as inspired by [142]. A Kapton isolated coaxial line is soldered to an OFHC loop located in the vicinity of the experiment position.



(d) Full in-vacuo assembly including the electrode assembly that had to be removed later on. A thin MACOR[®] sheet is put on top of the radio frequency antenna to avoid a short circuit by deposited titanium. This sheet is not attached.

Figure 4.10: Components in the vacuum chamber.

In October 2016, while performing experiments with a ³⁹K MOT, I discovered that we had a ferromagnetic component close to the atoms. The signature of this was obvious: After loading a MOT in a strong magnetic gradient of

20 G cm^{-1} , it was possible to trap atoms in the remnant magnetic field for minutes after the magnet current had been turned off. The electrodes had been made from a martensitic steel (1.4125) instead of an austenitic steel. This martensitic steel is ferromagnetic. We removed the electrode assembly. The mounting structure for the microscope assembly consists of six MACOR[®] parts that are connected to the upper MACOR[®] mounting plate with M4 screws. For all in-vacuo applications, we have used special stainless steel screws with a slotted thread to avoid virtual leaks. Additionally, we have added venting holes and reduced surface contact wherever possible. Illustrations of the mounting structure can be found in Fig. 4.11.

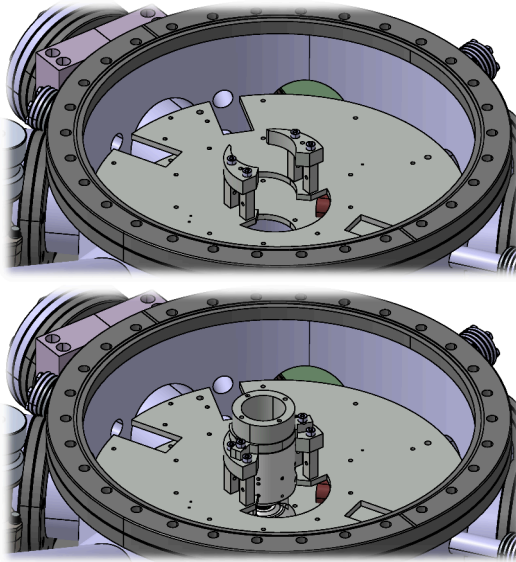


Figure 4.11: Microscope mounting before and after inserting the microscope

After the installation of the in-vacuo components, the chamber was evacuated and baked at about $170 \text{ }^\circ\text{C}$ for two weeks. During the first two days of baking, the chamber was pumped only with the turbo pump, afterwards the ion pump was switched on. The pressures measured during the bakeout are plotted in Fig. 4.12. After firing the TSP several times, a pressure of $3 \times 10^{-11} \text{ mbar}$ was reached on 04.04.16. Over the following weeks, this value fell continuously and stabilized at about $2 \times 10^{-11} \text{ mbar}$.

Only a few days after the bakeout was finished, we produced our first MOT of ^{39}K atoms on 07.04.16. Having trapped atoms enabled us to perform lifetime measurements, these are documented in the master's thesis of Christian Darsow-Fromm [143]. The resulting lifetime of about 70 s is consistent with the pressure in the vacuum chamber.²¹

²¹Later measurements performed after completion of the vacuum system resulted in a lifetime of 95 s.

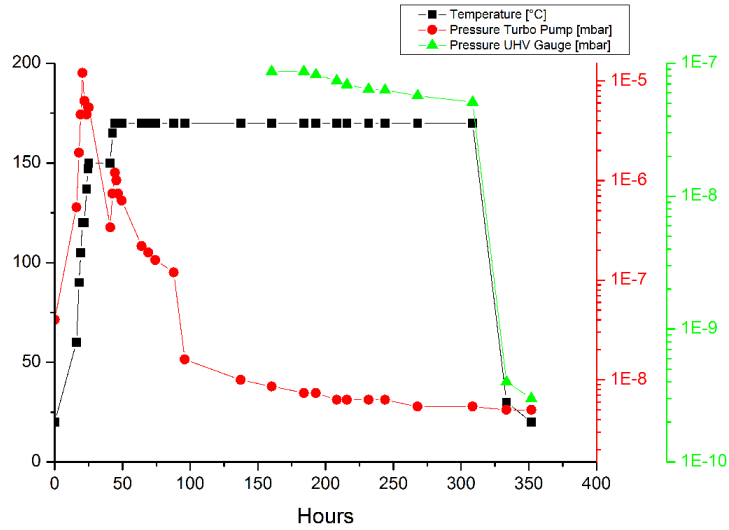


Figure 4.12: The temperature and the pressure during bakeout. The pressures were measured using a Pirani gauge close to the turbo pump and a Bayard-Alpert gauge in the pump section of the main chamber. The pressure decreased suddenly when the ion pump was switched on after about 85 hours.

4.2.3.6 Microscope installation

The microscope assembly had to be installed as the last step as it can only be baked at 100 °C. For this purpose, the chamber was flooded with pure argon. Using a pressure reducer, the argon pressure inside the chamber was regulated to 50 mbar above atmospheric pressure. Next, the upper CF100 viewport was removed and the microscope assembly lowered into the chamber where it was attached using two M4 screws.

We hoped that it might be possible to reach the 2×10^{-11} mbar regime without additional bakeout, but after one week of pumping and firing the TSP several times, the pressure was stuck at about 6×10^{-10} mbar. We decided to use self-regulating heating strips with a nominal maximum temperature of 100 °C in order to keep the temperature below the microscope's limit. The pumping section was heated with regular heating strips to 120 °C. The chamber was baked for three weeks. The highest temperature achieved close to the microscopes was 80 °C. This was limited by the self-regulating heating strip. Directly after this bakeout, we measured a pressure of about 2×10^{-10} mbar. After firing a TSP filament twice and degassing both pressure gauge filaments several times, the pressure fell to 2×10^{-11} mbar.

4.3 Magnet systems

This section describes how magnetic fields are created in our apparatus. In particular, this includes the coil geometry, the technical realization of the conductors and the resulting electric properties.

4.3.1 Functional requirements

- Create a linear quadrupole field in the 2D-MOT chamber
- Create a quadrupole field at the MOT position
- Enable magnetic transport of the trapped atoms from the MOT position to the measurement position. Reliable magnetic transport requires a gradient of about 100 G/cm.
- Generation of a homogeneous magnetic field at the microscope position of at least 250 G to exploit Feshbach resonances. According to [50], the Feshbach resonance between $|9/2, -7/2\rangle$ and $|9/2, -9/2\rangle$ ^{40}K atoms is at 202.10(7) G. For advanced experiments, it should be possible to generate a magnetic field with a gradient below $1 \times 10^{-2} \text{ G cm}^{-1}$.
- Generate magnetic fields along one horizontal axis with an amplitude of at least 1 G. This is required to define a quantization axis for optical pumping, absorption imaging and Raman cooling.

4.3.2 Technical requirements

- Field strength: The coils have sufficient turns to achieve the required field strengths. They should be positioned as close as possible to the atoms. In addition, the voltage and current range of the power supply that drives the current has to match the resistance of the coil. For rapid changes of the magnetic field, the inductance of the coils is also important.
- Field homogeneity: A homogeneous magnetic field is provided by Helmholtz pairs of coils. Under the assumption that the cross section of the conductor is negligible compared to the radius of the coil, the first and second derivatives of the magnetic field vanish in the center. In quantum gas experiments homogeneity is not that easily provided because the coils have a thickness that can not be neglected. A smart way to solve this problem is to install two pairs of coils with opposite field curvatures. By choosing the current ratio correctly, one can achieve a very homogeneous magnetic field.

- Temperature management: Several components of the experiment, in particular optical and optomechanical components, are sensitive to temperature changes. To reduce the amount of heat dissipated into other components of the apparatus water cooling and mechanical isolation are necessary.
- Vibration isolation: Rapid changes in the current flowing through the coils lead to mechanical vibrations. Thus, a direct connection between sensitive devices and the coil assembly should be avoided.

4.3.3 Resulting coil structure

The most stringent condition for the electromagnet design was to produce a magnetic trap of about 100 G cm^{-1} whose minimum can be shifted by 4 cm. There exist at least three solutions for a shiftable magnetic trap:

1. Overlap two pairs of quadrupole coils. Ramp one quadrupole current up and the other one down to perform a transport. This technique has been used for transports over larger distances very successfully without heating the cold atoms [144, 145].
2. Have one pair of movable coils. This scheme has been demonstrated in [146, 147] but has one disadvantage: Movable mechanics always have a limited lifetime and are never completely maintenance free. If one uses this scheme, one would have to ensure that the movable parts are easily accessible and replaceable.
3. Apply an additional offset field along the axis of transport. This is a good technique for short distances and we use it to align the transported atoms with our optical traps. For a transport over 4 cm this would require an offset field of 400 G to shift the 100 G cm^{-1} gradient. To produce such a large field with coils that are 30 cm apart is difficult. In the same context, creating a QUIC trap²² in our apparatus is not feasible. Switching a 25 G cm^{-1} spherical quadrupole trap into a QUIC trap would require a current of 800 A in the “Raman” coil pair.

²²QUIC traps [148] have a non-zero magnetic field minimum. This is useful to avoid Majorana spin-flip losses in the trap center which is required to evaporatively cool a quantum gas to quantum degeneracy.

We decided to use two pairs of overlapping quadrupole coils for the magnetic transport. The coil pair centered around the experiment position can be switched electronically into a Helmholtz coil and can provide highly homogeneous fields. Along the transport axis, we have one pair of coils that will define the field we use for optical pumping and Raman cooling. These key components are shown in Fig. 4.13.

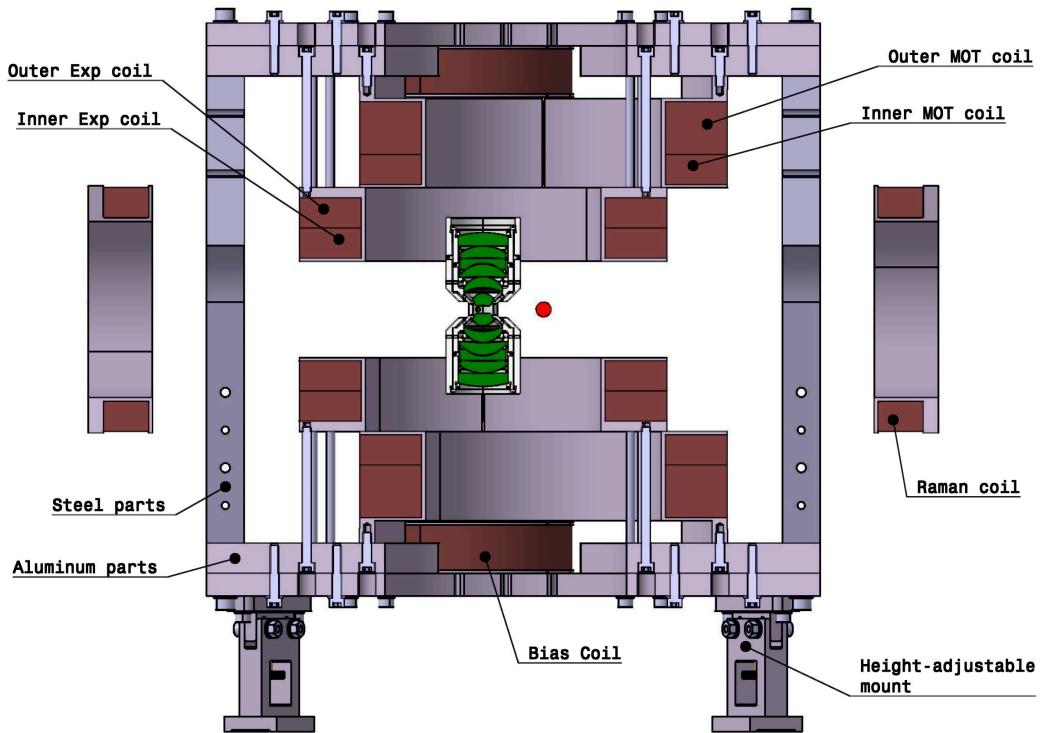


Figure 4.13: Cross-sectional view showing the magnet coils, the microscope optics and the position of the MOT. Each MOT coil and each Exp coil consists of two separate coils sharing the same bobbin. For coarse alignment of the magnetic trap with respect to the microscope, the coil assembly is equipped with height-adjustable mounts.

Along the horizontal axis perpendicular to the transport axis, coil placement is complicated by space limitations arising from the pumping section and the 2D-MOT, see Fig. 4.14. Inspired by cloverleaf type coils, we have added four small coils that are capable of producing a field along this axis. How this works is explained in Fig. 4.15.

4.3.4 Water-cooled high current coils

In most cold atoms experiments, cooling of the main electromagnets is necessary. In this experiment we also have water-cooled coils, but for the typical experimental procedure and the resulting duty cycles, water-cooling is not

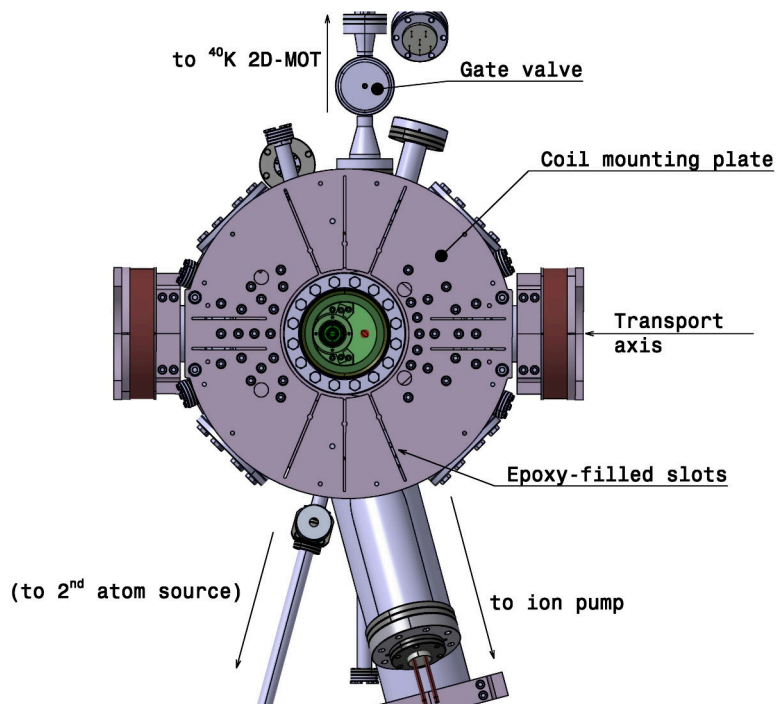


Figure 4.14: The apparatus with coil mounting structure and vacuum chamber seen from above. Perpendicular to the transport axis, coils can not be placed adequately because the space is blocked by vacuum equipment. To reduce the influence of eddy currents, relevant parts of the mounting structure are equipped with epoxy-filled slots.

strictly necessary here. From a thermal point of view, there are essentially two requirements the coils have to fulfill under normal operating conditions:

- The temperature should stay below the damage threshold.
- The coils should not heat their surroundings too much.

The first condition can be easily fulfilled by respecting technical rules - the heating of wire assemblies is well understood. Whether a proposed solution fulfills the second condition is much harder to check. The good thing about the second condition is that it becomes less relevant if one only requires the apparatus to be thermally stable under steady-state conditions - thermal drifts are allowed when the machine is switched on or off. Whether the first condition is met can be checked precisely:

Let us consider a coil that is made from $4\text{ mm} \times 4\text{ mm}$ solid copper wire with $8 \times 11 = 88$ turns. These numbers are the design values of the MOT coil we use - the largest coil in the apparatus. The copper wire used has Kapton isolation, here a PVC isolation is considered. Detailed information on the maximum rated current of PVC isolated wires is given in the technical standard DIN VDE 0298-4. PVC has a maximum operating temperature of 70°C which

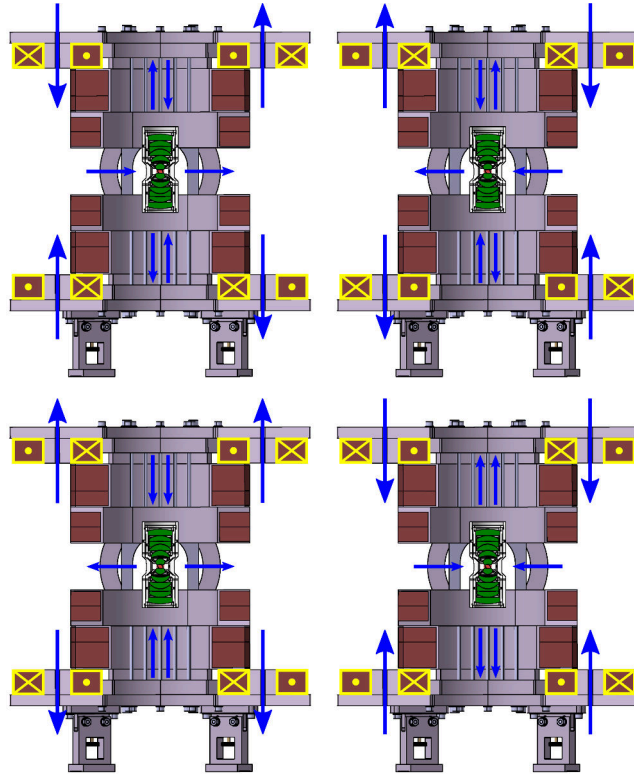


Figure 4.15: The “Bias” coils consist of four coils which are powered by one supply. The direction of the current can be chosen independently for each coil which results in 16 possible field configurations, but here only the four relevant ones are shown. In the upper row, the coils are configured to produce an offset field. In the lower row, they produce a gradient field.

defines the maximum rated currents. Kapton can be used well above 200 °C, thus the damage threshold estimate presented here is very moderate.

For a 16 mm² wire, the norm gives a maximum current of 80 A to 100 A depending on the exact usage conditions. This value has to be multiplied with a factor of 0.7 to take into account 11 neighboring wires and a factor of 0.3 to account for 8 layers. In the pessimistic scenario, this results in a maximum continuous current of 17 A. The currents that are actually used in the experiment are higher²³, but only applied for a short time. Most experiment could be performed without water cooling.

We did not want to restrict the apparatus to experiments that require only a low duty cycle of the magnet system and decided to install water-cooled coils. Using cooled coils also has the advantage of increased operational safety if the cooling is sufficient to keep the coils cold even if the power supply continuously delivers the maximum rated current.

There exist at least three types of fluid-cooled magnet coils with different pros

²³MOT current is typically 25 A, current for using Feshbach resonances is about 40 A.

and cons:

- Hollow-wire coils, where the cooling fluid flows through a channel inside the conductor
 - Monolithic structure, leaks are almost impossible unless electrocorrosion is severe
 - Good thermal contact between cooling medium and conductor
 - High flow resistance for the cooling fluid
 - As the cooling fluid is in contact with electric conductors, electrochemical processes might become relevant.
- Coils where the conductor is not directly cooled, but via a cooled mounting structure
 - Low thermal contact between cooling fluid and conductor
 - Water-cooled mounts are space consuming
 - No electrocorrosion
- Bitter-type coils [149]
 - Extraordinarily good contact between medium and conductor
 - Low flow resistance
 - Structure consists of many parts, leaks are very likely
 - Electrocorrosion is relevant

Our experiment uses hollow-wire coils where a Kapton isolated copper wire has been wound on an aluminum bobbin. The aluminum parts are slotted to suppress eddy currents. Epoxy resin “Araldit F” and glass fabric stabilize the coil. As the epoxy resin is cured at temperatures around 140 °C and Kapton can withstand temperatures even above 200 °C without degradation, the coils won’t experience any damages below 140 °C. The coils were manufactured externally²⁴.

We considered different wire diameters. A wire with larger diameter can be cooled more efficiently, as the diameter of the cooling channel is also larger and the flow at given pressure scales with the fourth power of the diameter. A coil wound from large diameter wire would also be shorter. Such a coil has less resistance and a smaller self inductance. But it requires power supplies capable of driving higher currents. We decided to use the smallest wire diameter available to avoid extremely high currents. This also reduces the risk of stray fields from uncompensated feed lines. The properties of the wire are given in Tab. 4.1.

²⁴Oswald Elektromotoren GmbH, Miltenberg

Description	Value
Outer contour copper	□4 mm
Isolation	Kapton, thickness ≈ 0.4 mm
Contour cooling channel	$\varnothing 2.5$ mm
Conducting cross sections	10.88 mm ²
Resistance at 20 °C	1.64 m Ω /m
Minimum bending radius	15 mm

Table 4.1: Properties of the hollow-wire used for our water-cooled coils according to a datasheet provided by Oswald Elektromotoren GmbH.

Each of the MOT coils and each of the Exp coils is split into two independent coils named “inner” and “outer”. The “inner” coil pair is closer to the atoms than the “outer”. This increases the cooling water flow at given pressure and enables us to produce very homogeneous fields at the experiment position as described in 4.3.2. It might also become useful if rapid field changes are required. The properties of the water-cooled coils are given in Tables 4.2, 4.3, 4.4a and 4.4b. The field strengths, gradients and field curvatures of the MOT and Exp coils are listed in Tab. 4.5.

Description	Value (inner coil)	Value (outer coil)
Number of turns*	32	55
Inner radius	81 mm	81 mm
Outer radius	121 mm	121 mm
Resistance*	32 m Ω	54 m Ω
Inductance*	220 μ H	650 μ H
Water flow* @ 4.5 bar	0.28 L min ⁻¹	0.20 L min ⁻¹

Table 4.2: Properties of each MOT coil (*according to datasheet)

Description	Value (inner coil)	Value (outer coil)
Number of turns*	31	31
Inner radius	81 mm	81 mm
Outer radius	121 mm	121 mm
Resistance*	31 m Ω	31 m Ω
Inductance*	220 μ H	220 μ H
Water flow* @ 4.5 bar	0.28 L min ⁻¹	0.28 L min ⁻¹

Table 4.3: Properties of each Exp coil (*according to datasheet)

Description	Value
Number of turns*	23
Inner radius	60 mm
Outer radius	80 mm
Resistance*	14 m Ω
Inductance*	88 μ H
Water flow* @ 4.5 bar	0.45 L min ⁻¹

(a) Properties of a Raman coil

Description	Value
Number of turns*	47
Inner radius	20 mm
Outer radius	60 mm
Resistance*	16 m Ω
Inductance*	51 μ H
Water flow* @ 4.5 bar	0.40 L min ⁻¹

(b) Properties of a Bias coil

Table 4.4: Properties of auxiliary water-cooled coils (*according to datasheet)

Coil pair	Helmholtz B_z [G A ⁻¹]	Helmholtz $\frac{d^2 B_z}{dz^2}$ [G cm ⁻² A ⁻¹]	Gradient $\frac{dB_z}{dz}$ [G cm ⁻¹ A ⁻¹]
Inner MOT	1.57	0.033	0.23
Outer MOT	1.84	0.043	0.27
Inner Exp	3.01	-8.607×10^{-3}	0.34
Outer Exp	2.34	2.574×10^{-2}	0.32

Table 4.5: Fields produced by the main water-cooled coils. The Helmholtz field at the experiment position is very homogeneous if the current in the inner coil pair is three times the current in the outer coil pair.

4.3.5 Coil mounting structure

The water-cooled coils are attached to a height-adjustable mechanical assembly that is not connected to the vacuum chamber. The exact height and position of the assembly was optimized after we were able to trap and transport atoms. Attaching the coils to a mechanical assembly well separated from the vacuum chamber reduces the coupling of vibrations and heat transfer from the coil assembly to other components. The magnetic forces are negligible in the regime we use. If one considers our Exp coil to be an ideal Helmholtz coil pair powered with 100 A, the force acting between the coils is

$$F = \mu_0 N^2 I^2 = 48 \text{ N}$$

Although this static force is not relevant, it excites acoustic vibrations in the assembly when fields are changed rapidly.

One design guideline was to reduce the influence of the coil assembly on optical access. We achieved this by connecting the upper and the lower part of the assembly with four narrow steel pillars. The coils themselves are connected to large aluminum plates. To suppress eddy currents, the aluminum plates are slotted and the slots filled with a mixture of epoxy resin, glass balls and cotton flakes. In addition, the connecting surfaces between separate parts of

the assembly have been coated with a layer of epoxy. The mounting structure is shown in Fig. 4.16.

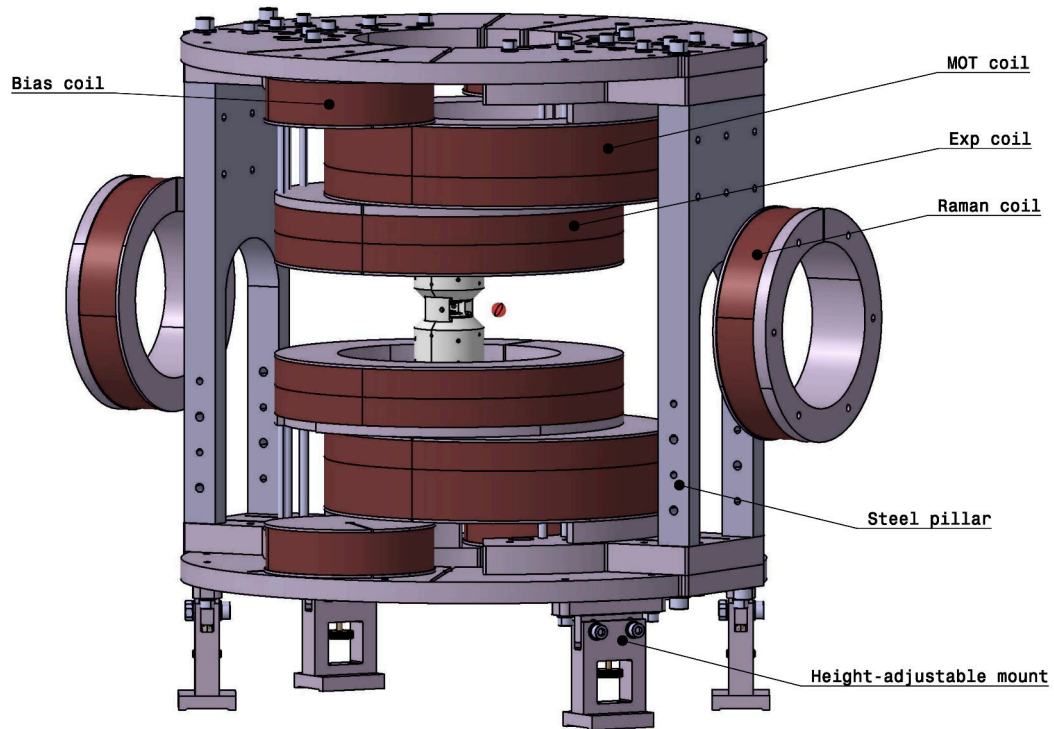


Figure 4.16: Full magnet assembly with coils and mounting structure. The mounts for the Raman coils are not shown. The coils are attached to slotted aluminum plates. The upper and the lower parts of the assembly are connected by four steel pillars. The MOT and the microscope are shown for orientation.

From today's perspective, I would recommend to make the coil bobbins and the mounting structure from fiber reinforced-plastics instead of aluminum.

4.3.6 High current electronics

The currents through the coils to generate the required magnetic fields are controlled using n-channel power MOSFETs²⁵ in an H-bridge configuration for switching and reversing the direction of the current. For this device the external lead current is 200 A and the maximum avalanche rating is 100 A (at 25 °C). The avalanche rating is important for our application, as MOSFETs used for switching inductive loads are likely to be driven into avalanche breakdown. The MOSFETs are controlled using the dual channel gate driver²⁶ in combination with a 15 V supply voltage provided by DC/DC converters. When applying a gate-source voltage of 10 V to this MOSFET, the drain-source resistance drops to 7.5 mΩ.

The magnets can be operated with currents up to 200 A, so we decided to use two MOSFETs in parallel to realize a switch. Currents passing through an H-bridge have to pass two switches. Accordingly, every H-bridge has a resistance of about 7.5 mΩ. A diode²⁷ is integrated in each circuit to have a well-defined current flow direction. It is rated for currents up to 230 A and has a voltage drop of 1.5 V.

Significant amounts of energy are dissipated in the high current circuits. At 200 A, the heat dissipated in each H-bridge is 300 W and in the diode additional 300 W. Sufficient cooling of the MOSFETs and diodes - which come in a SOT-227 package - is provided by attaching them to a water-cooled heat sink.

When using MOSFETs with inductive loads, one should include voltage limiting elements to protect them from damage. It is also advisable to include gate resistors that limit the switching speed of the MOSFET and thereby reduce unwanted “ringing” oscillations. The circuit configuration we have used for more than 1.5 years without damage is shown in Fig. 4.17.

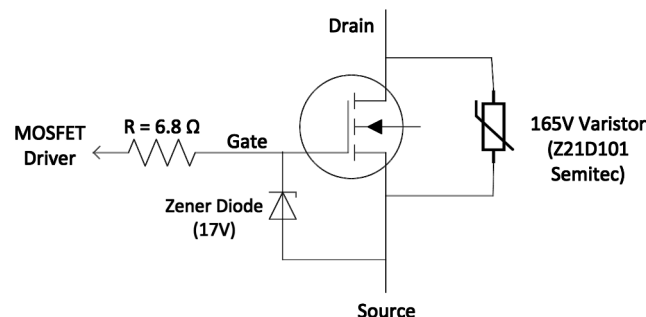


Figure 4.17: The MOSFETs used in our H-bridges are protected by a varistor between the drain and source and a Zener diode between gate and source. A gate resistor reduces the ringing effect occurring when the state of a MOSFET is changed.

²⁵IXYS IXFN230N20T

²⁶Analog Devices ADuM3220

²⁷Vishay VS-UFL230FA60

The voltage necessary to drive the circuit can be calculated from the maximum current and the voltage drops across the coils and the switching electronics. If the experiment requires faster field changes, it might be necessary to choose power supplies that provide higher voltages. We decided to use high speed programmable power supplies made by Delta Elektronika B.V., as we have good experience with these supplies. Details of the devices are listed in Tab. 4.6. The power supplies have opto-isolated programming inputs to avoid ground-

Coils	Power Supply	Voltage [V]	Current [A]	Power [W]
MOT	SM 30-200-P069-P154-P167-P231	35	220	6000
Exp	SM 30-200-P069-P154-P167-P231	35	220	6000
Raman	SM 18-50-P246-P249-P251	18	50	800
Bias	SM 15-100-P069	17	100	1500

Table 4.6: Power supplies for high-current coils. All power supplies are standard products made by Delta Elektronika B.V.

loop problems. From the supplied voltages and the inductance of the coil one can estimate the initial rate with which the current can be changed:

$$\dot{I}(t=0) = \frac{U}{L}$$

Neglecting mutual inductances, the inductance is about 1 mH for the Exp coils, 2 mH for the MOT coils and 0.2 mH for the Raman coils. For the Exp coil pair this gives $\dot{I}(t=0) \approx 33 \text{ A ms}^{-1}$.

4.3.7 Predominant eddy currents

We have taken measures to avoid currents flowing in the bobbins and in the surrounding aluminum parts. Eddy currents flowing through the vacuum chamber should be limiting for the timescale on which the magnetic field relaxes after sudden changes. The exponential decay constant of an eddy current flowing along a path with inductance L and resistance R is given by

$$\tau = \frac{L}{R}$$

To calculate it, one has to define a path inside the steel chamber for which the upper expression should be evaluated. One part of the chamber that combines a large inductance with low resistivity are the CF300 flanges. Their position with respect to the coils is such that a significant net magnetic flux passes through the flanges.

A round trip along one of these flanges has an inductivity of about 0.9 μH and a resistance of about 0.3 $\text{m}\Omega$ (taking the copper seal into account). This gives

a $1/e$ current decay time of $\tau = 3$ ms. For advanced experiments, magnetic fields have to be applied with a precision of 1×10^{-5} or even better. For the eddy currents to decay to the 1×10^{-5} level, it takes about 35 ms in this simple model.

4.3.8 Additional field coils

It is useful to have pairs of coils along all of the symmetry axes to compensate for the magnetic field of the earth or other external magnetic fields and to apply magnetic quantization fields for absorption imaging. The additional coils do not require water cooling because only relatively weak fields are required. The small coils are also included along the axes with the large water-cooled coils to provide more operational flexibility.

The additional coils were wound using 1 mm Cu wire fixed with epoxy resin. Each of the main water-cooled coils was equipped with three additional coils. Hand-wound coils supported by 3D-printed nylon bobbins were mounted along the transport axis and the axes along which the MOT and lattice beams enter the chamber.

4.3.9 Permanent magnet 2D-MOT field

Inspired by the diploma thesis of B. Höltkemeier [150], we decided to use a permanent magnet configuration for producing the 2D-MOT quadrupole field instead of using coils. The required gradient - as reported by other potassium experiments - is $\sim 10 \text{ G cm}^{-1} - 20 \text{ G cm}^{-1}$. Producing this gradient with coils is inefficient, as the separation between the coils is large: The distance from the coil to the 2D-MOT beam axis would be at least 70 mm in our case. A simulation of a hollow wire racetrack coil arrangement resulted in currents of about 100 A and a dissipated power of about 250 W. Water cooling and an expensive high current power supply would be required. In contrast, the required fields can be generated easily with permanent magnets.

The permanent magnet assembly consists of two bars, each containing ten $18 \text{ mm} \times 10 \text{ mm} \times 5 \text{ mm}$ neodymium magnets. These magnets have the magnetization quality N45SH which has a remanence of 1.35 T and is usable up to 150°C . The cross-sectional view in Fig. 4.18 shows how this arrangement with two magnet bars produces the required field geometry.

A numerical simulation²⁸ has been performed to calculate the resulting field gradient. In the apparatus, it is possible to vary the spacing between the magnet bars to find the gradient with the highest MOT loading rate but this procedure is tedious. We fixed the distance between the magnets and the atomic beam to be 67 mm. At this distance, a gradient of 13 G cm^{-1} is achieved.

²⁸using the software BiotSavart, Ripplon Software Inc.

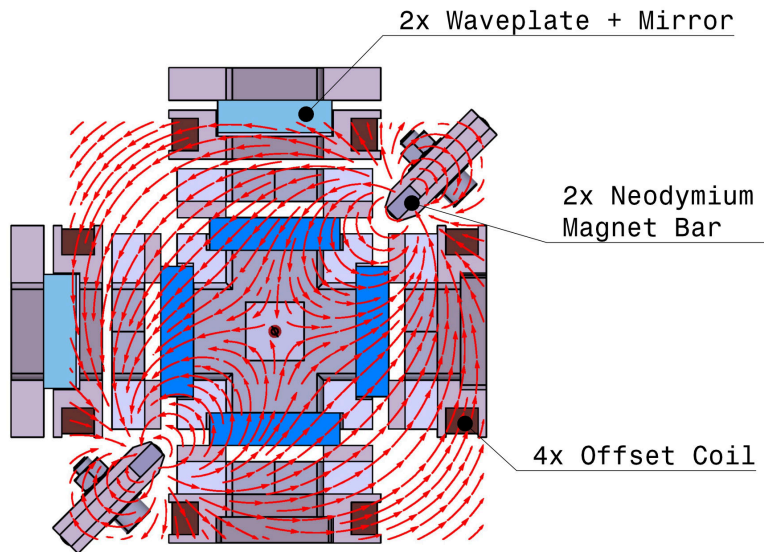


Figure 4.18: Cross-sectional view of the 2D-MOT chamber including surrounding magnets, coils and optics. The field lines show that the magnet arrangement produces the required quadrupole field. The field lines are taken from Fig. 3.19(a) in [150].

To account for misalignments and to compensate the gravitational sag, we added four small coils to apply offset fields. The offset currents are optimized for a high loading rate of the MOT. Currently, only the vertical offset field is required to maximize the MOT loading rate.

As we can not switch the 2D-MOT gradient off, we ensured that it does not produce significant stray field at the measurement position: The coordinates of the measurement position (in the main chamber) with respect to the center of the magnet assembly are (650 mm, 40 mm), where the first coordinate is along the atomic beam axis and the second coordinate is along the transport axis. At the measurement position, the magnetic field vector produced by the permanent magnets is (0.3 mG, 1.5 mG) and the vertical component is negligible.

4.4 High resolution imaging system

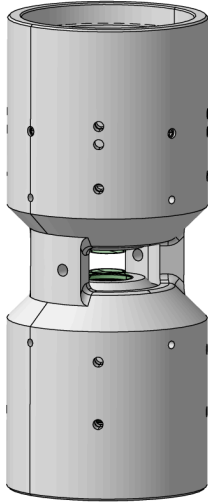


Figure 4.19: In-vacuo microscope assembly. The “double housing” contains two objectives.

The high resolution microscope assembly is the key component of our apparatus. It consists of two identical objectives facing each other and with a common focal plane. In principle, both microscopes can be used for imaging as well as manipulation simultaneously. In practice, we use one microscope for imaging and the other to create the desired physical system. Having two microscope lenses does not significantly enhance the possibilities of the apparatus, but it simplifies optical alignment tremendously since interferometry is easy with every beam that is being passed through the assembly. In addition, light patterns which are imprinted through one objective lens can easily be imaged using the other objective lens. The form and position of dipole traps can be adjusted easily.

This idea is not new, it is already implemented in our group’s Lithium experiment for example. What is new here is that we outsourced the problem of aligning the objective lenses to an optics company. This only became possible because the objective lenses are mounted within the vacuum system.

4.4.1 Optical design of the microscope objectives

Our high resolution microscope objectives are infinity-corrected achromats made from spherical lenses with a large field of view. In many respects, they are similar to microscope objectives used in life sciences. Nonetheless, two things are significantly different:

- As we do not want the atomic cloud to collide with the objective’s first lens, the working distance must be large.
- The microscope must be capable of handling large laser intensities. Optical cement between the lens elements is not allowed.

The most important optical properties of the microscope objective are listed in Tab. 4.7. The focal shift as a function of wavelength is plotted in Fig. 4.20.

Description	Value
Design	Spherical system, infinity corrected
Numerical aperture	0.75
Effective focal length	20 mm
Achromatic design wavelengths	767 nm and 870 nm
Field of view	$\varnothing 200 \mu\text{m}$
Working distance	2.5 mm
Exit pupil	31 mm
Number of lenses	6
Chromatic focal shift	$< 1 \mu\text{m}$ for λ between 740 nm and 890 nm $< 2.5 \mu\text{m}$ for λ between 720 nm and 910 nm
Absorptive transmission loss	$< 1.5 \%$
Reflective transmission loss	$< 6 \%$ for λ between 680 nm and 880 nm
Photon collection efficiency	15.7% @ 770 nm assuming isotropic emission

Table 4.7: Properties of the high resolution imaging and manipulation optical system.

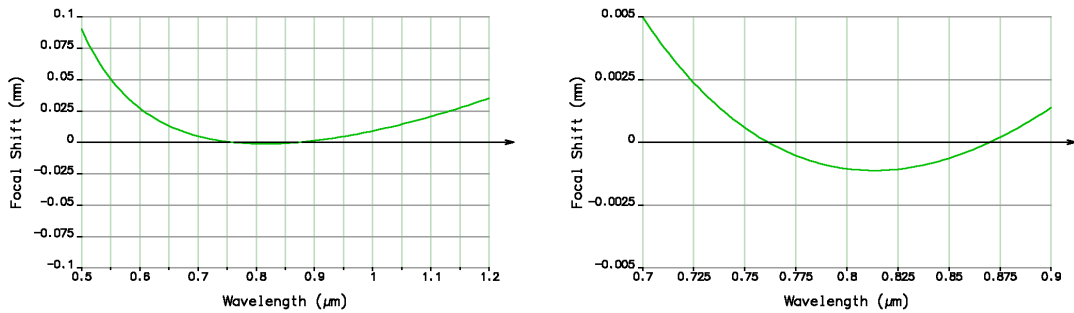


Figure 4.20: Focal shift of the microscope objective calculated with OSLO. The objective is designed to be achromatic at 767 nm and 870 nm.

We currently use the objective lenses at the wavelengths 770 nm for fluorescence imaging, at 767 nm for absorption imaging and for optical tweezers at 850 nm. The performance in terms of resulting spot sizes in the focal plane for different distances of the object to the optical axis is shown in Fig. 4.21.

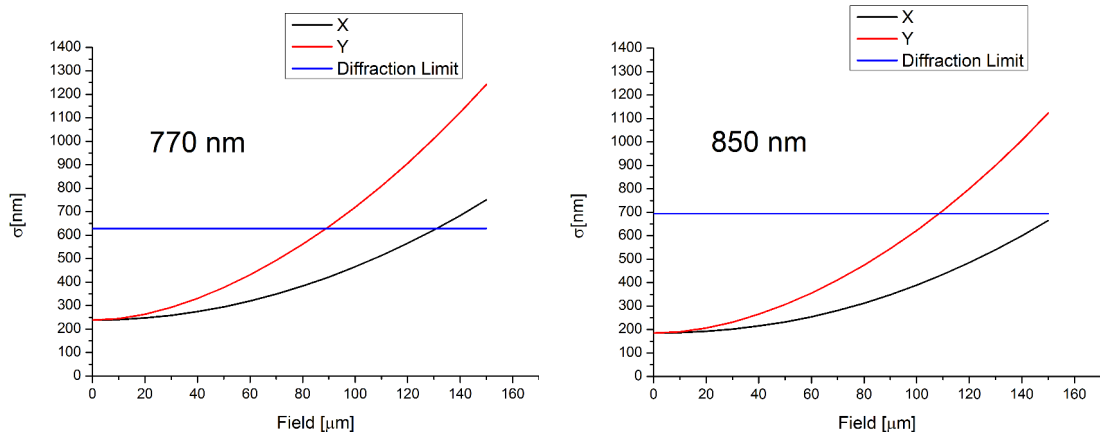


Figure 4.21: Spot sizes plotted against the displacement from the optical axis. The object is displaced in the y-direction. These calculated graphs show that the microscope design is within specification for the size of the diffraction-limited field of view.

I generated the plots from ray tracing simulations to check whether the lens design conformed with the specification.

The usable wavelength range is primarily defined by the tolerable focal shift. It can be extended by compensating the focal shift using an additional lens with low optical power. This is illustrated in Fig. 4.22, where I simulated the optical performance of the objective if one allows the focal shift to be compensated with an additional lens. If the NA is limited to 0.6, the objective is diffraction limited over the entire wavelength range from 600 nm to 1100 nm.

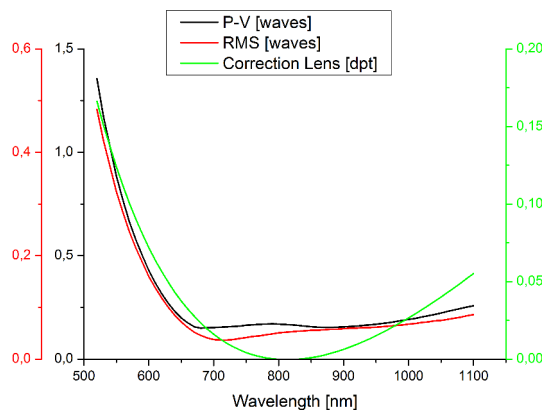


Figure 4.22: Calculated optical performance of the microscope at NA 0.75 in terms of peak-valley and RMS wavefront error for different wavelengths. In this calculation, the focal shift has been compensated by placing an appropriate “perfect” lens 1 m in front of the microscope. For each wavelength, the power of this correction lens has been optimized using a simplex algorithm.

4.4.2 Measures taken to ensure UHV compatibility

The design of the microscope assembly has been performed primarily by the experienced experts of the optical company Special Optics Inc. We advised them how their standard design has to be modified to ensure UHV compatibility.

The foundation of every vacuum compatible mechanical design is an appropriate choice of materials. A useful reference for selecting appropriate materials is given by the NASA publication “Outgassing Data for Selecting Spacecraft Materials” provided as an online catalog [151]. In the catalog, the total mass-loss (TML) of material samples after 24h hours, 125 °C bakeout under vacuum is listed for several thousand materials. For glues, the curing procedure is also documented. The mechanical parts of the microscope assembly have a surface area of about 800 cm². This is about 10 % of the steel surface area of the main chamber and to use a material with low TML is important. In addition, it was crucial to choose a material with a coefficient of thermal expansion (CTE) similar to standard optical glasses to avoid disarrangement of the lenses during bakeout. The materials that have been considered are listed in Tab. 4.8.

Material	TML [%]	CTE [$1 \times 10^{-6} \text{ K}^{-1}$]	E [GPa]	Machinability
MACOR [®]	0.01	8	67	+++
ZERODUR [®]	0.04	0.05	90	+
PEEK	0.14	50	4	+++

Table 4.8: Possible materials to be used for the microscope mechanics. The total mass-loss (TML) is cited from [151] and a good measure for the applicability in ultra-high vacuum environments. There exist some other machinable ceramics that are very similar to MACOR[®], but have better thermal conductivities and higher operating temperatures.

We decided to use MACOR[®], which is a machinable glass ceramic. It has negligible outgassing, zero porosity, a CTE that is very similar to optical glasses and can be machined to high precision with standard workshop equipment. Finding a UV-curable glue that could be used in small droplets for the purpose of attaching lenses to spacer rings and for locking adjustable parts of the assembly in the correct position once the interferometric adjustment is finished was not that easy. We decided to use the optical adhesive “OPTOCAST 3415”. It is curable with UV-light and/or thermally. Other important properties are:

- Single component - no stirring is necessary. Stirring might lead to inclusion of air bubbles.
- Linear curing shrinkage is only 0.07 %.
- TML according to [151] is only 0.15 %.

- CTE is $< 12 \times 10^{-6} \text{ K}^{-1}$, very similar to the CTEs of MACOR[®] as well as optical glasses.

These excellent properties arise from the silica filling material (85%).

For adjustment purposes, the microscope assembly includes ordinary M3 set screws made from 1.4404 stainless steel, without vented threads. After successful interferometric testing, the optics company locked these screws with glue.

The main design task during UHV optimization was to remove any potential virtual leaks by adding numerous venting holes, notches and slots. Most noteworthy in this context is that we had to add ventilation to the lenses themselves at locations where they are in direct mechanical contact. The structure of the microscope is shown in Fig. 4.23.

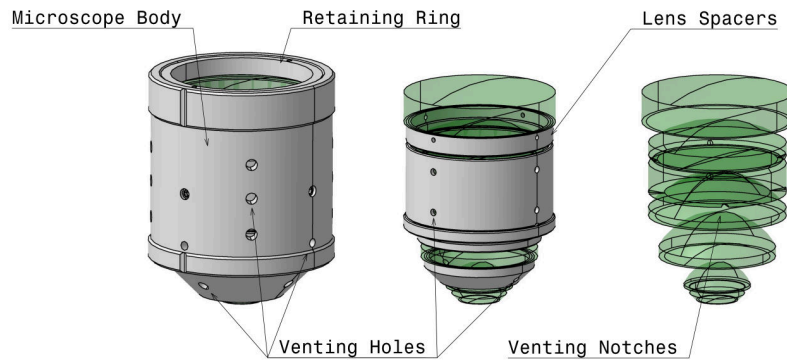


Figure 4.23: One of the objective lenses: Full assembly, microscope body removed and all mechanical components removed. The microscope body as well as the lens spacers are equipped with several venting holes. Three of the six lenses are in direct mechanical contact. These lenses have been equipped with venting notches to pump the volume between the lenses.

4.4.3 Microscope manufacturing

All MACOR[®] components have been produced by our university’s workshop, cleaned using the cleaning procedure described in 4.2.3.1 and baked under high vacuum at about 300 °C for 48h. Finally, the components were wrapped in clean aluminum foil and sent to Special Optics Inc. for assembly. The individual microscope objectives were assembled and interferometrically tested. Afterwards, they were mounted into the “double housing” while ensuring good relative positioning of the lenses by interferometry. During this procedure, the distance between the lenses was adjusted by choosing an appropriate spacer from a set that was available in steps of 10 μm. Hence, the lens spacing might be as much as 5 μm off, but this error can be easily compensated with other

optics. The entire alignment procedure was performed under atmospheric conditions. For the optical aberrations except defocus, it is not relevant whether the lenses are in vacuum or in air. The focal length of each microscope is - according to ray tracing simulations - $7\ \mu\text{m}$ longer in air. This focal shift has been accounted for when the objective spacing was fixed.

To ensure appropriate mechanical stability during the entire assembly process and afterwards, it was necessary to apply small glue droplets at about 60-80 positions inside the assembly. The glue was cured using UV light and post-cured thermally at $95\ ^\circ\text{C}$ for 6 hours. After the final cure, the entire assembly was again tested interferometrically to ensure that no changes had been caused by the heat treatment.

After a thorough visual inspection, Fig. 4.24, we installed the microscope assembly inside the vacuum system as described in 4.2.3.6.



Figure 4.24: Optical testing of the microscope assembly

4.5 Lasers and optics

Modern ultracold atom experiments use laser light in several ways for manipulating internal and external degrees of freedom of atoms. This radiation has to be produced, controlled with high degree of precision and brought into contact with the atoms in the correct way. We use laser systems spatially separated from the experiment and deliver the radiation through single-mode optical fibers. This is attractive as it ensures high beam quality and enables us to minimize the amount of equipment close to the sensitive experiment.

4.5.1 Laser systems

All laser systems used in this experiment are based on semiconductor laser technology. We use external cavity diode lasers (ECDL) for producing coherent light with a precisely defined frequency. These devices reach output powers of some 10 mW. In most of our applications, higher powers are required. Thus, we use the light from an ECDL to seed a tapered amplifier (TA) chip in a master oscillator power amplifier (MOPA) configuration. A TA is similar to a laser diode, but capable of handling much higher intensities. It has an active medium, but does not include laser feedback and is not capable of lasing without an external seed. TAs can reach powers up to a few watts, in our experiment typically 2 W.

Our ECDLs use a diffraction grating in a Littrow configuration, which is aligned so that the first order of diffraction is coupled back to the laser diode. This external feedback stabilizes the laser and reduces its linewidth down to a few 100 kHz, which is adequate for addressing atomic transitions in alkali metals reliably. The laser can be tuned by rotating the diffraction grating, changing the laser diode current or the laser diode temperature. Mode-hop free tuning ranges of many GHz are possible. This ECDL technique became popular in the 1990s, and was developed in the cold atom community, see [152] for reference. Nowadays, it is a standard technique commercially available and we use the product “DL pro” provided by the company Toptica.

The TAs in our apparatus are manufactured by DILAS and are delivered on a “C-Mount”. We add a temperature stabilized heat sink as well as optics for coupling in the seed beam and for collimating the output. One drawback of tapered amplifiers is their poor beam profile which significantly reduces the usable output power. Another drawback is that the TA emits a broad background spectrum with a power that is about 40 dB suppressed compared to the power at the seed wavelength. In our apparatus, as will be explained in detail in 4.5.3, this background leads to a problematic amount of D1 light in the optical paths that are supposed to contain only D2 light. To solve this problem, we use narrow band optical filters on the output of our TAs. Figure

4.25 illustrates the configuration we use as a laser source when higher power is required.

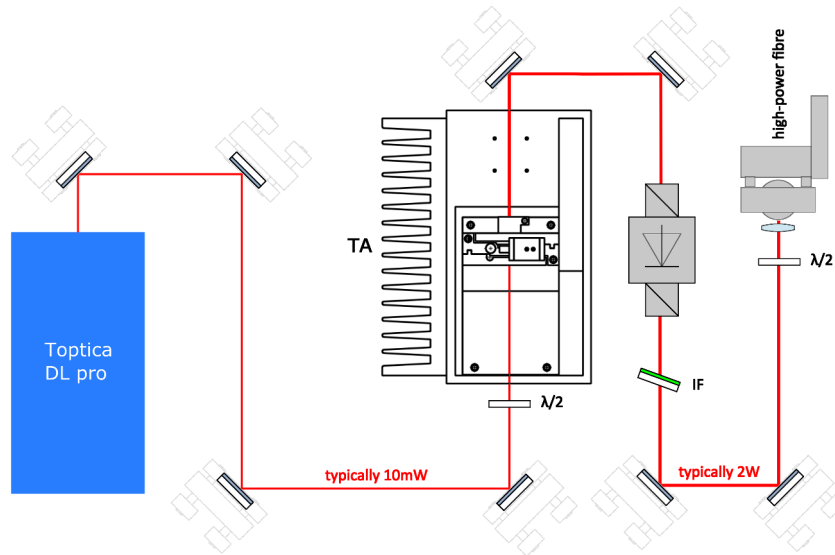


Figure 4.25: Our MOPA configuration. A TA chip is seeded by a commercial ECDL. An optical isolator is integrated into the ECDL to suppress unwanted optical feedback. The output of the amplifier passes an additional optical isolator. After spectral filtering with an interference filter (IF), it is coupled to a high-power fiber patch cord.

In the course of setting up the experiment, we have had two master students working on the D2 and D1 laser systems. For a detailed review of these laser systems, I refer to their master theses [153] and [143]. The latter is still more or less up to date.

4.5.1.1 D2 laser system

The first step in our experimental sequence is to collect potassium atoms in a magneto-optical trap. This experimental trapping and cooling technique uses the D2 line. D2 light is also useful for taking absorption images of the atoms. The requirements imposed on the D2 laser system are:

- It should be usable for ^{40}K as well as ^{39}K (not simultaneously). Switching from one isotope to the other should not take too much time.
- Enough power on both cooling and repumping transition has to be provided to supply both the 2D-MOT atom source as well as the MOT. For ^{39}K , the MOT is largest if cooling and repumping powers are more or less equal. In ^{40}K , the required amount of repumping light is lower.
- The detuning of both repumping and cooling light has to be adjustable. For the repumping light, the required tuning range is only a few MHz

and can be achieved by tuning acousto-optic modulators (AOM). The cooling light is also used for absorption images. At high magnetic fields, the required tuning range can easily reach several hundred MHz.

- For absorption images, one needs resonant D2 cooler light. As the illumination times of these images are typically short - only some 10 μ s - switching the light on and off has to be performed using AOMs. As these AOMs always have some amount of light leakage, mechanical shutters are required to completely block the light.

One main design guideline was to reduce the number of components - in particular the number of lasers and amplifiers. This improves the reliability of the system and reduces costs. We finally decided to have only two amplified laser sources. The repumper laser is locked to a vapor cell, the cooler laser is locked to the repumper laser using a beat lock. 2D-MOT and MOT use separate AOMs for the cooling light to allow for small detuning differences, but the cooling laser detuning is primarily defined by the beat lock. In our experimental sequence, absorption images are taken after the magnetic transport. As this transport is slow - it takes some 100 ms - the cooling laser can be easily tuned from the MOT detuning to the required imaging detuning by changing the beat lock frequency. There is enough time to close the mechanical shutters that block the MOT light and afterwards the same AOM used during the MOT phase can be used for the short light pulses required for absorption images. Figure 4.26 on page 83 gives a detailed overview of the resulting laser configuration.

A very important part of a laser system in atomic physics is the frequency stabilization to a reference element. Here, the reference element is a vapor cell containing a natural distribution of potassium isotopes. The repumper laser is locked to the “crossover” feature that arises from the transitions $|^2S_{1/2}, F = 1\rangle \rightarrow |^2P_{3/2}\rangle$ and $|^2S_{1/2}, F = 2\rangle \rightarrow |^2P_{3/2}\rangle$ using saturated absorption spectroscopy. The relevant atomic level scheme with optical transitions is given in Fig. 4.27. For laser stabilization, one has to generate an error signal which can be fed back to the laser. Here, this is done using a technique called “modulation transfer spectroscopy”: Two overlapping laser beams enter the vapor cell, one “pump” and one “probe” beam. The pump beam is frequency modulated. This frequency modulation is modulated onto the probe beam via interaction with the potassium vapor. A photodiode measures the intensity of the probe beam after passing the cell. The error signal is generated by demodulation. The spectroscopy system is shown in Fig. 4.28.

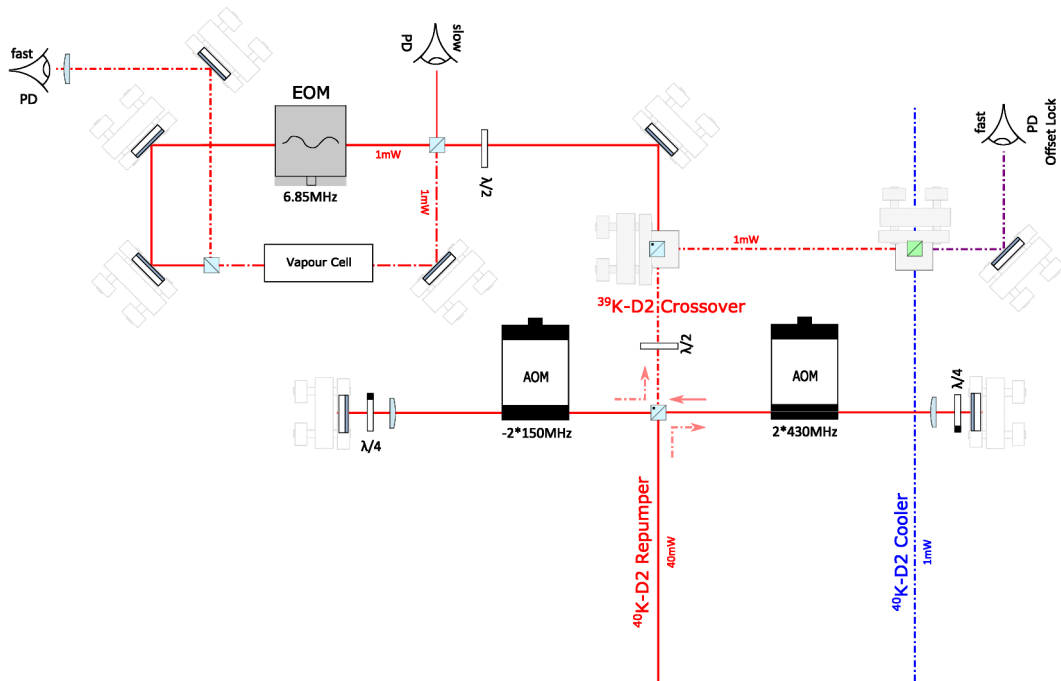


Figure 4.28: Modulation transfer spectroscopy system. Two AOMs are used in a double-pass configuration to shift the repumping light to the crossover in ^{39}K . The 430 MHz AOM has to be disabled to trap ^{39}K .

Prior to spectroscopy, the light is frequency shifted by two double-pass AOMs. This compensates for the frequency difference between the ^{39}K crossover and the ^{40}K repumping transition. This double-double pass AOM arrangement wastes a lot of laser power but is very attractive because switching between isotopes is simplified. For experiments with ^{39}K , one has to disable the 430 MHz and do some optimization on the lock signal. As the cooling laser is also referenced to the ^{39}K crossover, the lock points and offset-lock tuning frequencies are different.

4.5.1.2 D1 laser system

The D1 laser system shown in Fig. 4.29 is used for the following purposes:

- During MOT loading, slightly blue-detuned D1 light is fed in to lower the density of the atomic cloud and increase the MOT capacity significantly.
- After MOT loading, we apply a Λ -enhanced grey molasses sequence.
- The atoms are pumped to the outermost magnetically trappable m_F -state using the D1 line.
- After magnetic transport, we apply grey-molasses light to load the atoms into the optical dipole traps.

- Prior to Raman sideband cooling, we prepare the atoms in the desired m_F -state.
- During Raman sideband cooling, the required pumping photons are also supplied by the D1 system.

To have a flexible system that can be easily expanded, we decided to include a reference laser that is locked to the ^{39}K D1 line which serves as the beat lock reference for the other lasers.

The molasses cooling scheme requires a small amount of D1 repumping light that excites the upper ground state $|^2S_{1/2}, F = 7/2\rangle$. The relevant transition in the case of ^{40}K is about 1286 MHz detuned from the transition that is used for the molasses cooling. We modulate the D1 molasses light with an EOM at about 1286 MHz to add a small amount of repumper.

An additional repumping laser is needed for situations where only repumping light is required. This laser is called the F-pump laser.

The D1 laser system can be used for ^{40}K as well as ^{39}K but so far we have not used it with ^{39}K . To switch between isotopes, one would need different beat lock frequencies and an EOM with significantly different frequency.

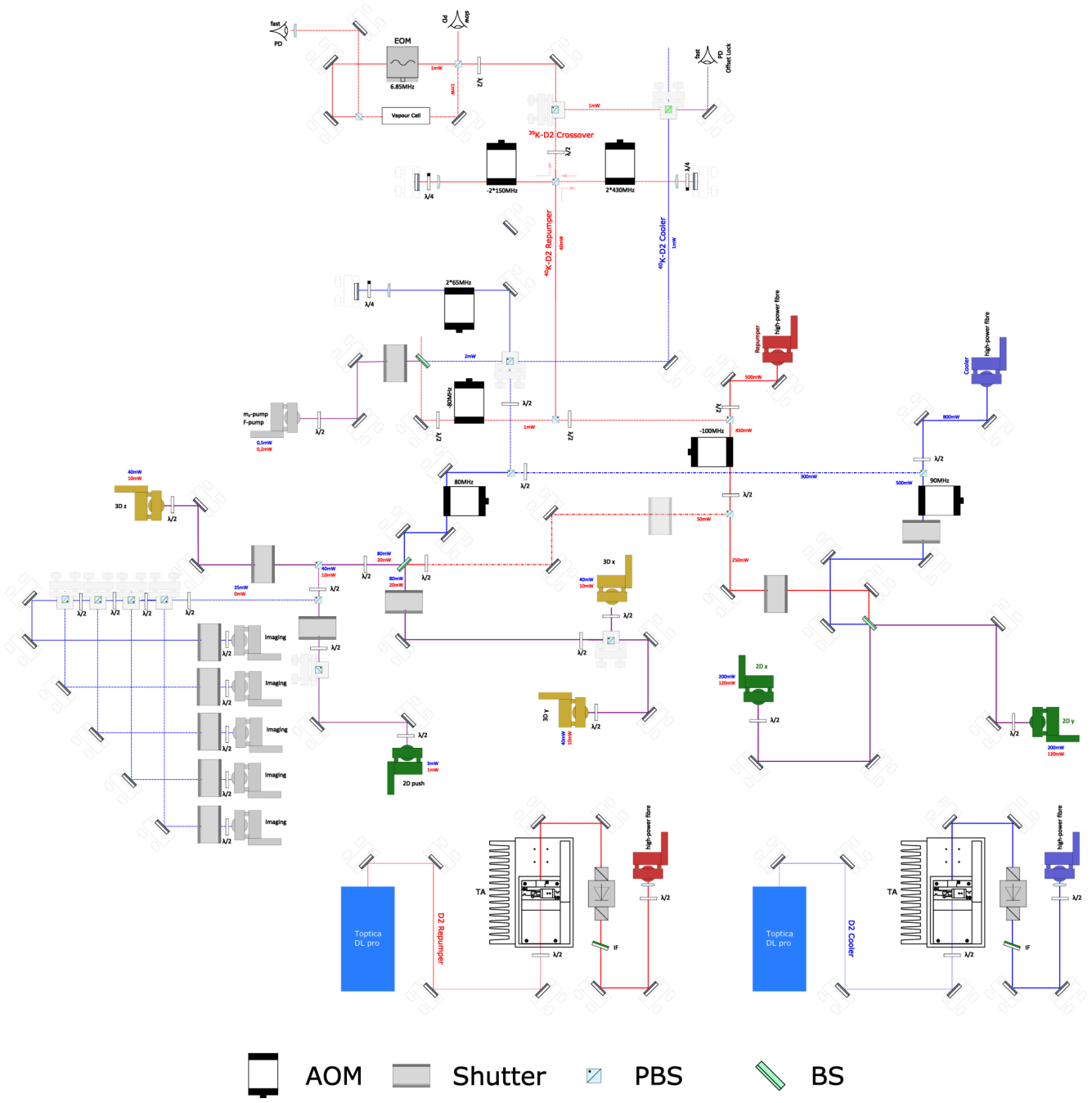


Figure 4.26: Overview of the D2 laser system. The laser powers and frequencies are approximate values. The repumping light is drawn in red, the cooling light in blue. The lasers are located at the bottom, the optics for spectroscopy (detailed illustration in Fig. 4.28) at the top of the drawing. 2D-MOT fiber couplings are drawn in green, MOT fiber couplings in yellow. A beam preparation for optical pumping on the D2 line exists but we have not used it so far. This is an updated version of Fig. 2.6 in [143].

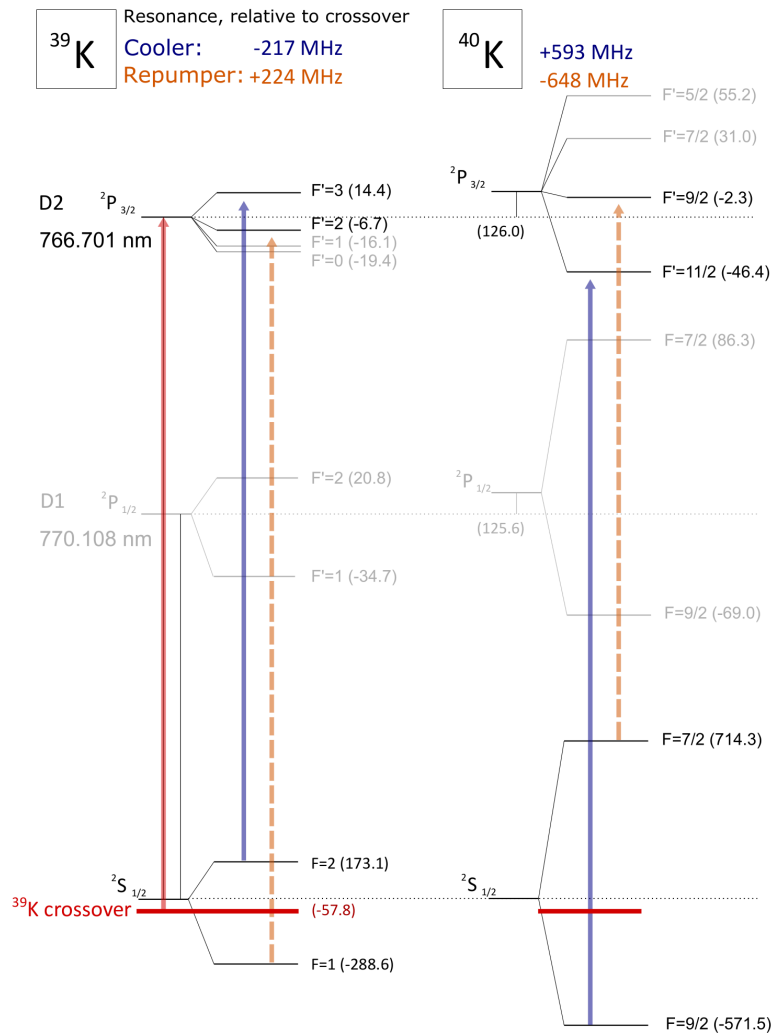


Figure 4.27: Level schemes of ³⁹K and ⁴⁰K. The repumper laser is locked to the crossover in ³⁹K, regardless of which species is being trapped. ³⁹K MOTs need a lot of repumping light because the hyperfine splitting in the excited state is small. The hyperfine levels of ⁴⁰K are inverted.

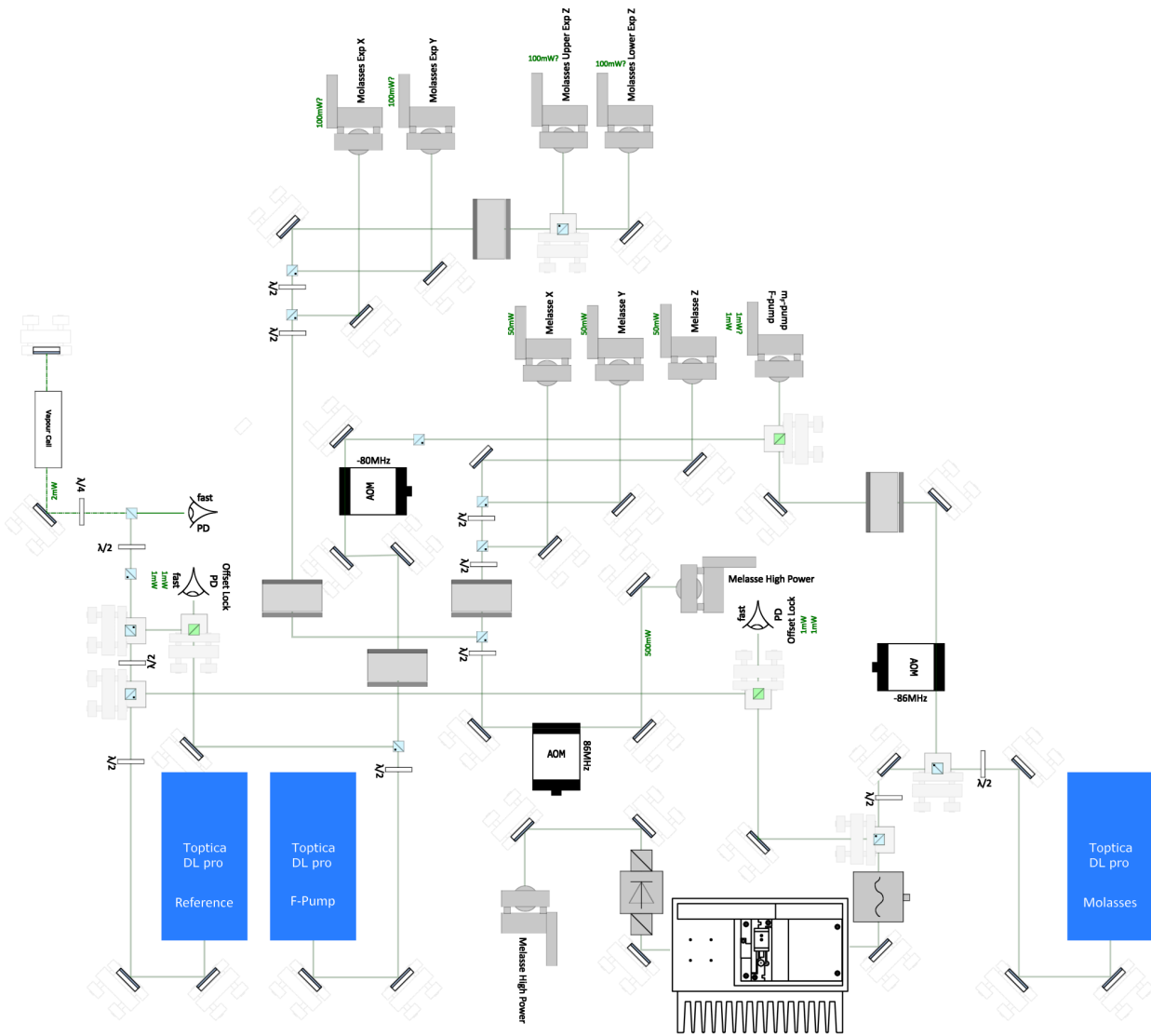


Figure 4.29: Illustration of the D1 laser system. It provides grey-molasses, F-pump and m_F -pump light for both the MOT and the measurement position. This is an updated version of Fig. 4.5 in [143].

4.5.1.3 850 nm laser system

Infrared 850 nm radiation is used to trap the atomic sample in optical dipole potentials. The choice of this wavelength results as a compromise between

- the required trap depths and trap frequencies
- a sufficiently low scattering rate
- a reasonably high optical resolution to achieve high tunneling rates between neighboring trap sites
- the availability of economic, reliable laser systems with sufficient output power.

We decided to use our standard MOPA in combination with several fiber couplings with AOMs for power stabilization and fast switching. To avoid unwanted interference between different traps, the AOMs use different frequencies. Currently, we use three TAs seeded by one ECDL to have enough power for all optical traps.

4.5.1.4 Raman laser system

In Raman sideband cooling, the narrow linewidth provided by far detuned coupling of the states in a Λ three-level system is exploited for addressing motional quantum states of trapped atoms. The ground states $|^2S_{1/2}, F = 9/2\rangle$ and $|^2S_{1/2}, F = 7/2\rangle$ form the lower levels of the Λ configuration, $|^2P_{3/2}, F = 7/2\rangle$ the upper state. The transition $|^2S_{1/2}, F = 9/2\rangle \rightarrow |^2S_{1/2}, F = 7/2\rangle$ is driven by adding two light fields, which are red-detuned from the $|^2S_{1/2}\rangle \rightarrow |^2P_{3/2}\rangle$ manifold by many GHz and which have a relative detuning given by the energy difference between the two ground states. If the relative detuning of these light fields is chosen correctly, one can address the red motional sideband. Following this momentum transfer, the atom is pumped back to the initial internal state.²⁹

Typical Raman sideband cooling makes use of lasers that are some 10 GHz off-resonant. It is not feasible to obtain such a large detuning using modulation techniques on resonant D2 light. Hence, we use an additional diode laser for this purpose. As the exact value of the global Raman beam detuning is not important and the temperature stability of the Toptica diode lasers is very good, it was not necessary to include any kind of frequency stabilization. A

²⁹The cooling scheme will be explained in more detail in 5.7.2 and an illustration of the relevant levels and transitions is given in Fig. 5.26. Here, the focus is on the generation of the Raman coupling beams.

cheap wavelength meter³⁰ is connected to the system permanently in order to monitor the wavelength and to be able to change the value of the global detuning in a controlled manner. 10 GHz detuning corresponds to a wavelength difference of about 0.02 nm which is easily measured. The D2 Raman laser system is shown in Fig. 4.30.

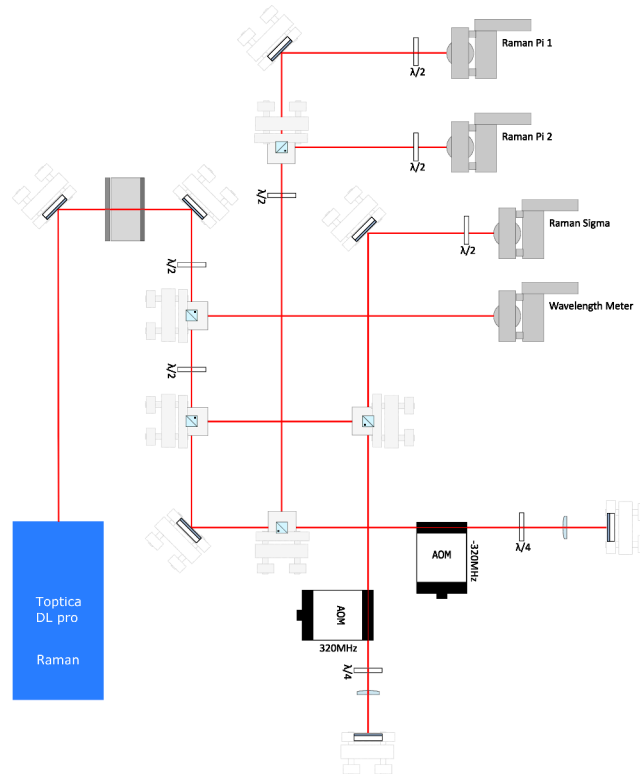


Figure 4.30: The D2 laser system used for Raman sideband cooling.

A precise control of the frequency difference of the Raman beams - we call them “Sigma” and “Pi” corresponding to their polarization at the experiment - is crucial. As the frequency difference is about 1286 MHz and this is roughly 4×320 MHz, we pass both beams through AOMs in double-pass configuration, thereby shifting the frequency of the Sigma beam up by 640 MHz and of the Pi beam down by the same value. The radio frequency signals are created by first mixing 1370 MHz from a frequency generator with 84 MHz from a computer controllable DDS source³¹, then filtering out the unwanted sideband and dividing the signal by four with a frequency divider. The motional states can then be addressed by changing the DDS output frequency. In order to cool all degrees of freedom, one of the Pi beams is split and coupled to the atoms along different axes.

³⁰Moglabs MWM772

³¹The DDS is not fast enough to provide 1286 MHz or 320 MHz directly.

4.5.2 Optical assemblies around the experiment

Here, I will summarize aspects of the optical assemblies that help us to bring our atomic samples in contact with the required light fields.

4.5.2.1 2D-MOT optics

The 2D-MOT cooling beams are elliptical beams with a size of about $50 \text{ mm} \times 25 \text{ mm}$. Each of the two beams contains cooling and repumping light. As shown in Fig. 4.31 they are shaped using two cylindrical lenses with focal lengths of 150 mm and 75 mm.

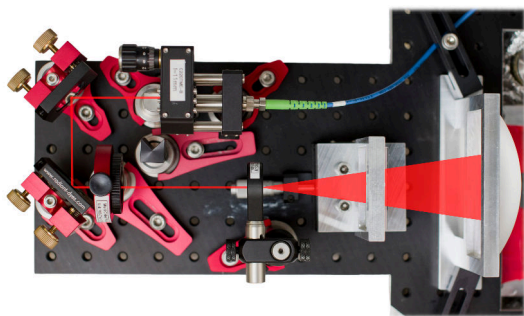


Figure 4.31: One of the 2D-MOT beam output couplers. A telescope consisting of one aspheric lens and two cylindrical lenses is used for preparing a large elliptical beam.

After passing through the chamber, the beams are retroreflected using large protected-silver mirrors and custom made $\lambda/4$ waveplates³². Adjusting the 2D-MOT beams was trivial, an increased density could be easily observed along the atomic beam axis as soon as the polarizations and detuning had been chosen approximately correct. We have about 150 mW of cooling light and 50 mW of repumping light in each of the 2D-MOT arms.

To increase the atomic flux, we use a push beam powered with a few mW of MOT light. It propagates parallel to the axis defined by the differential pumping stage and exits the main chamber through a view port. We observe a significant increase in MOT loading rate when using the push beam. Initially, we also planned to use a $2D^+$ -MOT configuration. For this purpose, we included a mirror in the vacuum chamber by electropolishing one steel surface. During experiments conducted in the course of Christian Darsow-Fromm's master thesis [143], we did not observe an increased loading rate in the $2D^+$ -MOT configuration. Later on, the mirror surface became coated with potassium and can no longer be used.

4.5.2.2 MOT and molasses optics

At the MOT position, we have three retroreflected D2 MOT beams as well as three retroreflected D1 molasses beams. D2 and D1 light is delivered in separate optical fibers and collimated to beam diameters of about 25 mm for

³²Castech, Low Order, 80 mm \times 35 mm

the D2 light and 12.5 mm for the D1 light. A polarizing beamsplitter (PBS) cube is used to overlap the beams, before they pass through a 767 nm low order $\lambda/4$ waveplate to create the correct MOT polarization and orthogonal molasses polarization, see. Fig. 4.32.

The retro-reflector is formed by a $\lambda/4$ waveplate and a dielectric mirror. As we use the reflected PBS port for the D1 light and the waveplates are made for D2 light, we do not expect the D1 beams to be perfectly σ -polarized. Nonetheless, the polarization of the D1 light is approximately opposite to that of the D2 light. We chose this D2/D1 combination scheme for simplicity but during our first experiments with D1 molasses light, it turned out that the fact that the handedness of the D1 light is opposite to the D2 light is a very useful feature: With this polarization and a blue D1 detuning, the blue detuned molasses beams in combination with the MOT gradient field form a restoring force, see Fig. 4.33. This is particularly useful as we are not able to switch off the MOT

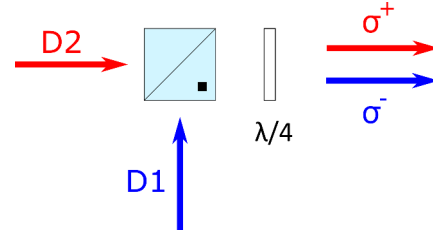


Figure 4.32: Beam combination and polarization preparation at the MOT position.

gradient sufficiently fast to enter a grey molasses phase directly following the

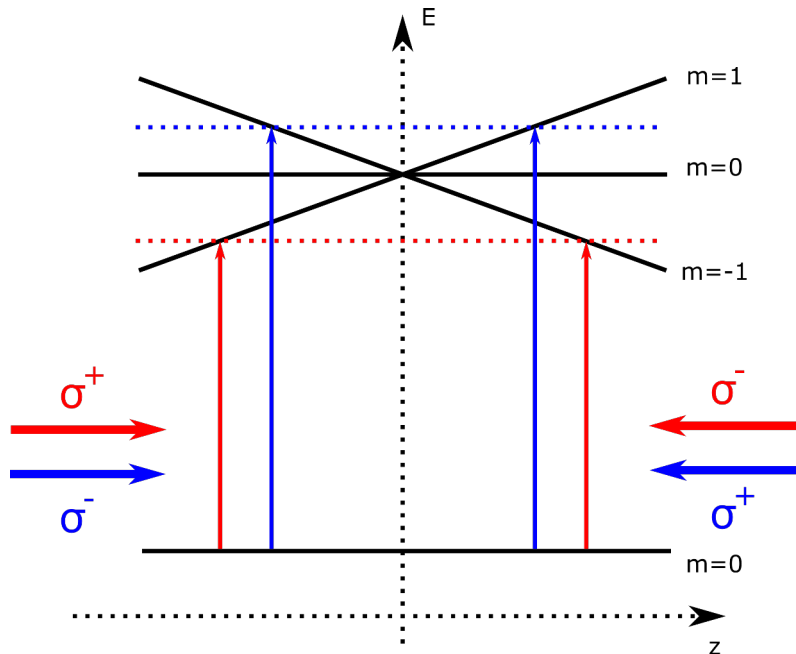


Figure 4.33: In a MOT configuration, blue-detuned light exerts a restoring force on the atoms, if the polarization is reversed compared to the usual red-detuned case. Referring to their detunings, the D2 light is drawn in red and the D1 light in blue.

gradient sufficiently fast to enter a grey molasses phase directly following the

MOT phase due to the electrical conductivity of the vacuum chamber. We discovered this feature around the same time a similar effect was reported in a ^{87}Rb experiment and published in [154].

We chose a space saving optomechanical design consisting of 30 mm cage system parts and lens tubes and placed the output couplers and the retro-reflectors far away from the UHV chamber to ensure that MOT optics do not restrict any optical access to the microscope position.

4.5.2.3 Lattice optics

At the experiment position, two horizontal, crossed, retroreflected $\lambda = 850$ nm beams form an optical lattice. As there is no vertical beam, each of the resulting lattice sites has a tubular geometry.³³ We use this lattice for practice and for preparing larger cold atom samples which will be used to reach quantum degeneracy. We use a beam waist of about $w_0 = 30$ μm for the lattice and have a laser power of about $P = 300$ mW at each output coupler. In our scheme, both lattice arms are p-polarized, hence there is no interference between them. In this case, the trap frequencies are³⁴

$$\nu_z = \frac{4}{\pi} \sqrt{U_{dip} / (\lambda^2 m)}$$

$$\nu_r = \frac{2}{\pi} \sqrt{U_{dip} / (w_0^2 m)}$$

where

$$U_{dip} = 3 \times 10^{-36} \text{ J } P w_0$$

is the depth of a single running wave trap. For our design parameters, we obtain $U_{dip} = 1 \times 10^{-27}$ J $\hat{=} 73$ μK , $\nu_r = 184$ kHz and $\nu_z = 2.6$ kHz.

The schematic of one of the lattice arms is shown in Fig. 4.34. In principle, it is straight forward to produce a focus of some 10 μm using achromatic lenses with sufficient apertures. What makes it difficult here is that we have to reflect the light with a dichroic mirror and this mirror - due to the large number of dielectric coating layers - is curved and introduces aberrations. To compensate for these aberrations, the focusing achromats have to be mounted with a significant tilt. To check the performance of the optical system and to find the correct tilt angles, we checked the resulting spot size on a CCD camera.

Having the ability of taking absorption images along the lattice axes was crucial for the alignment procedure. Fortunately, each of the running wave traps produces an atomic density excess on the magnetically trapped cloud that is well visible in the pictures. This could be used for aligning the lattice beams

³³A vertical lattice passing through the microscope assembly was added in November 2018.

³⁴As an introduction to optical dipole traps, I can recommend [155].

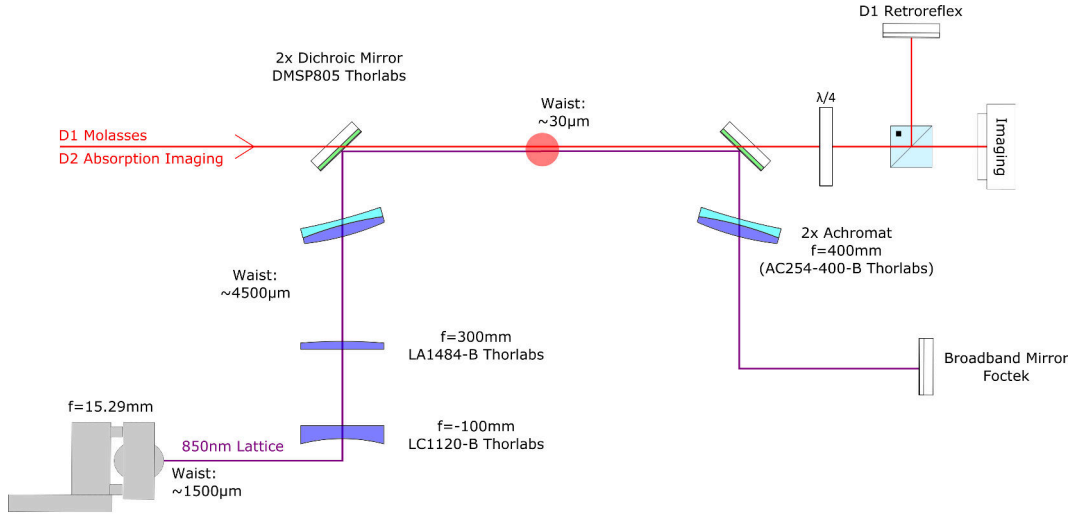


Figure 4.34: Schematic view of one of the lattice arms. The 850 nm light is expanded using a telescope and focused onto the atoms using an achromatic lens. As a dichroic mirror is used to combine this light with D1 and D2 light that is also needed at the experiment position, the achromat has to be tilted significantly in order to compensate aberrations introduced by the dichroic mirror. After passing through the vacuum chamber once, the light is collimated using an identical achromat and retroreflected.

with respect to each other and with respect to the atomic cloud. A detailed report is given in Sec. 5.5.

4.5.3 Beams passing through the microscope assembly

The primary tasks of the microscope objectives is to image optical potentials and atomic fluorescence. Currently, the optical potentials are single optical tweezers or arrays of tweezers. A tweezer is produced by feeding a large Gaussian beam with small aberrations into the upper microscope objective. The lower microscope collimates the light and it might be retroreflected - this is useful for adjustment purposes and could also be exploited physically as the resulting optical potential has a much higher vertical trap frequency. The outgoing tweezer light is not perfectly collimated, as the distance between the two objectives is not perfectly correct, as explained in 4.4.3 on page 76. The effect can be measured easily using a shearing interferometer and compensated with a telescope. The difficulty with producing a diffraction-limited tweezer is to make the input beam aberration free. Canceling the aberrations - primarily introduced by the dichroic mirrors that have to be used for separating tweezer light from D1 and D2 light due to the polarization requirements - is done by slightly tilting the lenses that are used for expanding the beam to the desired size.

The D1 fluorescence scattered in the Raman cooling process is collimated after

the microscope and is imaged to an intermediate image plane using a $f = 1000$ mm achromat. Together with the EFL of the objective (20 mm), this results in an intermediate image magnified by a factor of 50. From here, the light is collimated again using a $f = 500$ mm achromat and then focused on the SCMOS camera with a $f = 100$ mm achromat. This lens combination images the intermediate image with a demagnification of 5. So the total magnification of the D1 fluorescence imaging system is 10. To prevent D2 light that is also part of the Raman process from hitting the sensitive SCMOS camera, three identical narrow band filters are included in the imaging path. The first of these filters is located close to the intermediate image plane and is used not only for protecting the D1 imaging path, but also for separating the light that is used for D2 absorption imaging. We chose a very similar magnification for the absorption imaging.

The illumination beam necessary for absorption imaging is provided by focusing a large laser beam into the microscope objective using an achromat with a focal length of $f = 750$ mm. The achromat and the first microscope objective then form a telescope that reduces the beam size and produces a small collimated beam at the atoms position if the position of the achromat has been chosen correctly. To determine the expected waist at the atom position, one needs to know the rear focal length of the microscope objective. A simulation using OSLO gives a rear focal length of about 20.5 mm. Accordingly, a beam with 11.5 mm waist is demagnified to about 0.3 mm. Figure 4.35 illustrates how a collimated beam can be produced by the microscope objective from a convergent beam.

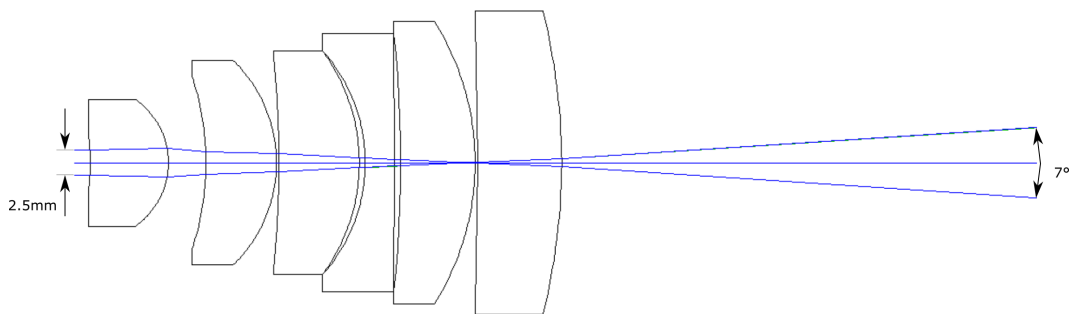


Figure 4.35: A convergent beam entering the microscope forms a collimated beam in the focal plane. The rear focus of the microscope objective is located inside the lens assembly, about 45 mm from the front focus.

This technique of producing a small collimated beam at the position of the atoms is used for additional beams as well:

- two D1 molasses beams, one from above and one from below
- one Raman Pi beam coming from below

We do not understand the mechanism in detail, but it turned out that having vertical D1 molasses beams is very helpful for loading the optical lattice and tweezer potentials. The Raman Pi beam is crucial for being capable of cooling all degrees of freedom with Raman sideband cooling.

The optical systems surrounding the microscopes are illustrated in Fig. 4.36. The different polarizations of the beams have been omitted from Fig. 4.36, they are as follows:

- Tweezers: linear polarization perpendicular to the axis defined by the magnetic transport
- Absorption imaging system illumination: circularly polarized
- D1 molasses: circularly polarized, handedness identical to the corresponding beam at the MOT position
- Raman: linear polarization parallel to the transport axis

The beam preparation is also not shown in Fig. 4.36. After the fiber output couplers, the beams are magnified using telescopes. For the case of the D1, imaging and Raman light, the beam quality is not that important. They are prepared using a single telescope consisting of an aspheric lens with short focal length and an achromat. When preparing the tweezer light, more care was taken to make the beam aberration free. The aberration can be reduced by minimizing the curvature of the fringes displayed on a shearing interferometer. We achieved a better beam quality when using two telescopes with smaller magnification than one with large magnification. For the tweezer light, the magnification is about $5 \times 6 = 30$.

Adjusting the microscope optics is simplified tremendously by having two opposing, perfectly aligned objective lenses. Nonetheless, there are some helpful tricks:

- When removing the Semrock filter located in front of the absorption imaging camera, the tweezer potential is imaged here. After compensating small focal shifts by slightly adjusting one of the lens positions, one can use the camera image and adjust the tweezer optics to minimize the resulting spot size and to adjust the position.

- If the 750 mm achromat that focuses the D1 and imaging light into the microscope is removed, the D1 light that exits the lower microscope simulates atomic fluorescence. This light was used for coarse alignment of the fluorescence imaging system.
- Imprints of the imaging beam on the atomic cloud can be observed on the absorption pictures taken along directions perpendicular to the microscope axis. If the focusing achromat in such a situation is removed as described above, one can also observe how the microscope focus is aligned with respect to the atoms. This procedure is explained in more detail in 5.5 on page 105.

4.5.4 Auxiliary absorption imaging systems

All relevant optical axes are equipped with absorption imaging systems useful for alignment purposes. A nice additional benefit of having these cameras: One can easily search for unwanted light leakage. The auxiliary absorption imaging systems have a very low optical resolution. The one with the highest numerical aperture is along the transport axis. The NA is about 0.04 which results in a diffraction limit of about $12\ \mu\text{m}$. Currently, we do not need any higher resolution in the horizontal plane. The low horizontal NA is primarily caused by the dimensions of the vacuum chamber and by the close spacing of MOT and experiment position. Exploiting the theoretical limits defined by the chamber would give a NA of about 0.15.

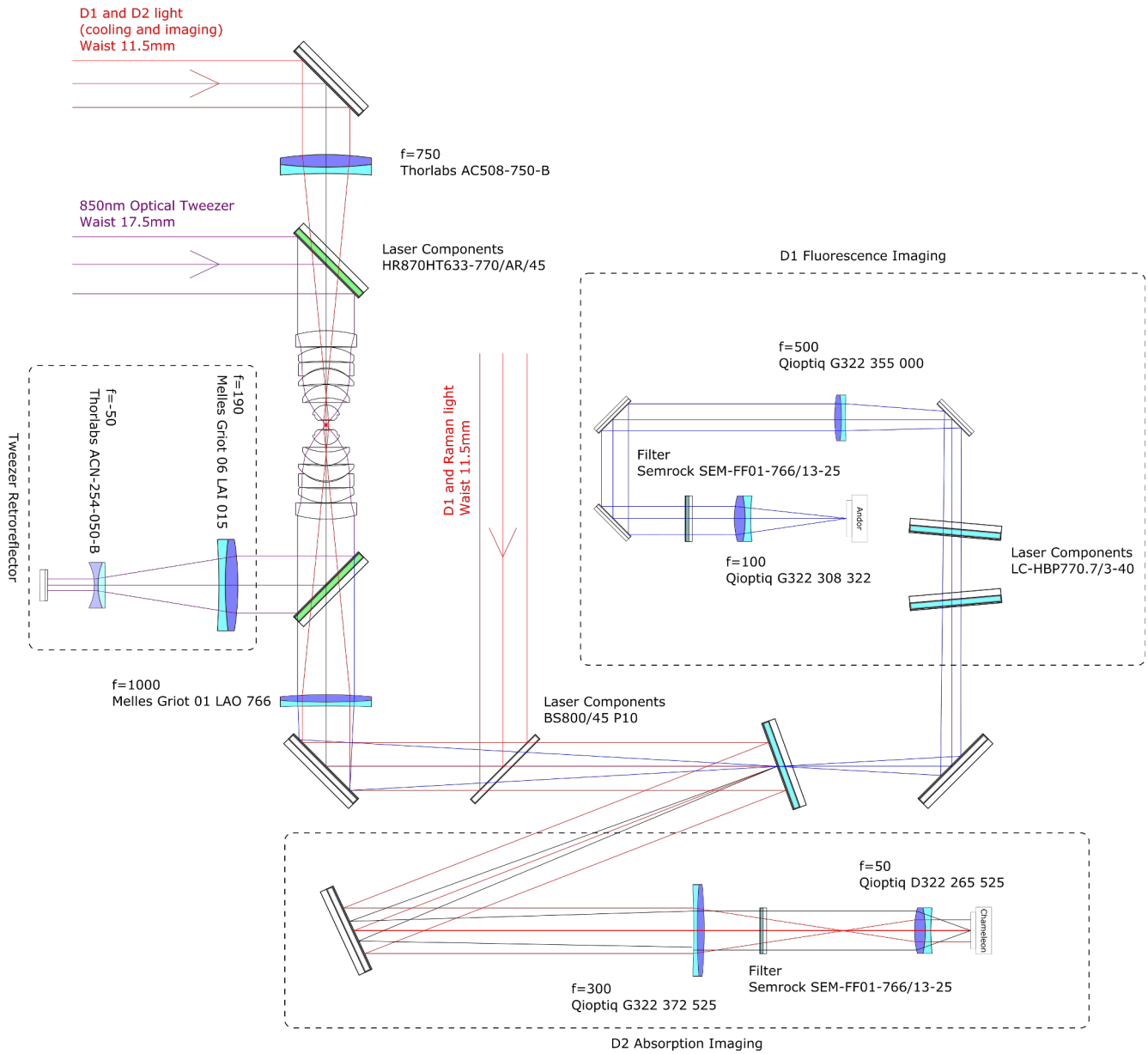


Figure 4.36: Optical systems for the high resolution part of the quantum gas microscope. The illustration only shows the key components and the spacing is not to scale.

Chapter 5

On the pathway to tweezer-plaquette physics

In this chapter I describe and characterize the procedure for preparing arrays of ultracold atoms, explain the physics and provide technical details.

5.1 MOT loading

The MOT apparatus was commissioned by Christian Darsow-Fromm and a detailed description and characterization can be found in his master thesis [143]. Most of the details given there are still valid. The latest improvements are described here.

The number of trapped atoms in the MOT is optimized by adjusting the optics and the MOT parameters. This number can be ascertained by measuring the amount of light scattered by the atoms. The scattered MOT light is collected using a lens placed outside the vacuum chamber and imaged onto a CCD camera¹. The number of atoms is estimated using the following procedure:

1. Two images are taken, the first one with atoms, the second at the end of the experimental cycle with no atoms but still with MOT light on. By subtracting the counts pixel by pixel, we obtain a resultant image that is essentially free from stray light.
2. We perform a two-dimensional Gaussian fit on the background-subtracted image. The fit yields the height A of the Gauss peak (in counts) and the widths w_x and w_y (in camera pixels). The total number of counts in the Gaussian peak is given by $N_C = 2\pi Aw_x w_y$.
3. The camera converts the incoming photons into electrons that can be collected and counted. At the given wavelength of $\lambda = 767$ nm, the

¹FLIR (Point Grey) CMLN-13S2M-CS

conversion efficiency is about 0.3. During readout, the resulting pixel values are digitized with 12 bit precision so a saturated pixel has $2^{12} = 4096$ counts. According to the technical documentation of the camera, a pixel is saturated if it contains 6421 electrons. From these figures it follows that the camera produces about $0.3 \times \frac{4096}{6421} \approx 0.2$ counts per photon so the number of photons hitting the camera chip is about $N_{Ph} = N_C/0.2$.

4. Only a small number of the photons scattered by the trapped atoms actually reach the camera. The solid angle accepted by the imaging lens, given by its diameter $D = 25$ mm and distance from the atoms $d \approx 26$ cm, is $\Omega = \frac{\pi D^2}{4d^2} \approx 7.3 \times 10^{-3}$. Hence, the total number of scattered photons is $N_{Ph,tot} = \frac{4\pi}{\Omega} N_{Ph}$.
5. The MOT cooling light is characterized by a certain detuning δ and an intensity which is usually expressed in multiples of the saturation intensity $I = s \times I_{sat}$. The MOT beams actually have a Gaussian intensity distribution, but we shall assume that the intensity distribution is constant. The spatial dependence of the detuning arising from the magnetic quadrupole field is also neglected and the atoms are considered to be two-level systems. Accordingly, the repumping light is not taken into account and the effective scattering rate of each individual atom for the MOT cooling light is given by

$$\gamma' = s \frac{\Gamma/2}{1 + s + (2\delta/\Gamma)^2}$$

where $\Gamma = 2\pi \times 6$ MHz is the natural linewidth of the atomic transition. With the exposure time t , the atom number is then given by

$$N = \frac{N_{Ph,tot}}{t \times \gamma'}$$

The saturation intensity for this transition is about 1.75 mW cm^{-2} and we assume each MOT beam has an intensity of $10 \times I_{sat}$. With three retroreflected MOT beams and a negligible amount of absorbed light, we estimate $s = 60$.

In 2016, few weeks after loading our first MOT of ^{39}K (93.26 % natural abundance), we loaded ^{40}K (0.012 % natural abundance) as well. We achieved an initial loading rate of about $1 \times 10^4 \text{ s}^{-1}$. After inserting an enriched potassium sample (3 % of ^{40}K) into our 2D-MOT chamber in January 2017, the loading rate could be increased to about $5 \times 10^6 \text{ s}^{-1}$.

The number of atoms derived from fluorescence measurements could be roughly confirmed by using the absorption imaging technique. The evaluation of absorption images is much less sensitive to technical uncertainties, as - in the limit of using very short light pulses with negligible saturation- the only experimental parameters that enter into the particle number calculation are the

cross section of the atomic transition and the magnification of the imaging system². We had to image the atoms while they were magnetically trapped. In this scenario, the detuning of the imaging light is spatially dependent. In addition, due to the magnetic quadrupole, there exists no well-defined quantization axis and accordingly no well-defined atomic cross section for interaction with circularly polarized light. Hence the number of atoms is underestimated. Despite these complications, the atom numbers derived from absorption and fluorescence imaging are very similar as shown in Fig. 5.1. The loading curves

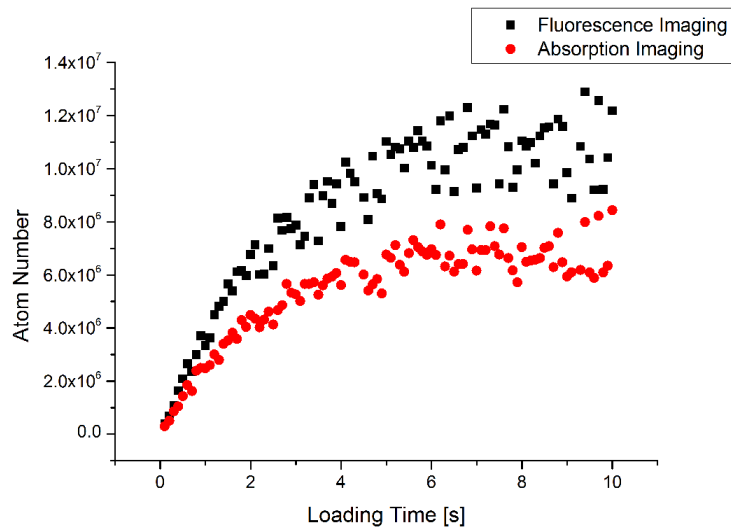


Figure 5.1: Loading curve of the ^{40}K -MOT in an early stage of the experiment (February 2017) derived from fluorescence imaging and absorption imaging assuming a cross section of $1.12 \times 10^{-13} \text{ m}^2$. Shot-to-shot fluctuations were relatively high but improved over the following months.

show large shot-to-shot fluctuations in the atom number. It took some months to eliminate the technical issues causing these fluctuations. The most crucial improvements were

- reduction of vibrations on the laser table by using a commercial high precision shutter system with minimal vibration³
- using commercial ECDLs⁴ with improved intrinsic stability
- improvement of laser locking electronics, in particular the ones that have to be tuned during the experimental cycle. This was easily done once we switched to commercial laser hardware. With the controllers we use now⁵, a combined laser stabilization acting on both laser current and

²[156] presents theory and experiments on absorption imaging in the saturated regime.

³Stanford Research Systems SR 475

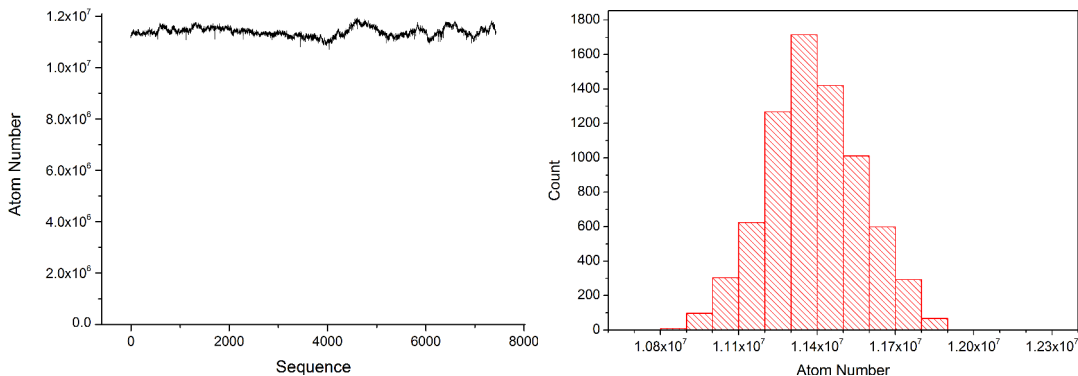
⁴Toptica DL Pro

⁵Toptica DLC Pro

piezo voltage is easily realized, enabling us to reliably tune the diode lasers with sufficient speed within the experimental cycle. The lasers are primarily frequency-stabilized via the laser current. The piezo voltage feedback loop is used with low gain and serves to compensate for drifts on the timescale of hours. As the laser diodes are temperature-stabilized, such long term drifts are primarily caused by atmospheric pressure variations effectively changing the optical path length of the external laser cavity.

- optimized polarization matching at the input side of the polarization-maintaining optical fibers.

Now, the atom number fluctuations are down to about 2% over 12 hours as illustrated in Fig. 5.2.



(a) Atom number plotted against the number of experimental cycle.

(b) Statistics of measured atom numbers. The mean value is 1.14×10^7 , the standard deviation 1.8×10^5 .

Figure 5.2: Stability analysis of the MOT atom number derived from fluorescence measurements. The data covers a time span of about 12h.

We have discovered that the capacity of the MOT can be increased by feeding in near-resonant D1 molasses light (cooling and repumping transition) during MOT loading along all of the MOT axes thereby reducing the density of the atomic cloud. A similar technique has been previously used in a ^{39}K experiment and published in [157]. In the MOT sequence, we enable the D1 light during loading and after simultaneously switching off the D1 light as well as the 2D-MOT, we wait 50 ms prior to imaging the atoms. By this, we ensure that the atomic cloud can relax to a usual MOT ensemble. MOT loading curves with and without this D1 capacity enhancement are shown in Fig. 5.3.

To further increase our MOT loading rate, we tried to boost the 2D-MOT vapor pressure by light-induced atom desorption using incoherent UV light [158]. Using intensities up to 40 mW cm^{-2} of 375 nm light produced by a LED we could not observe any effect.

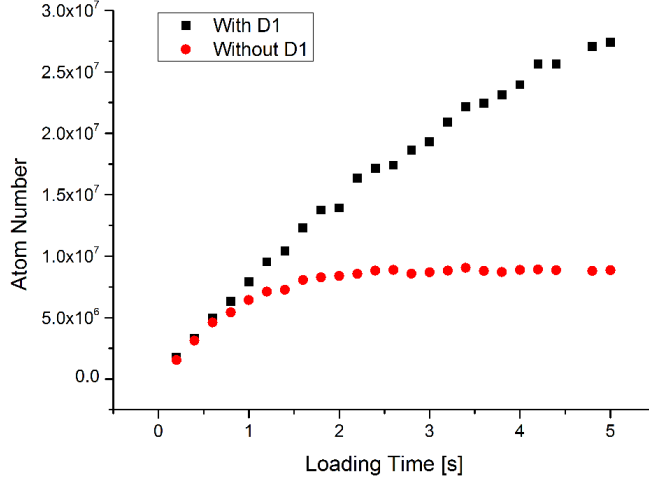


Figure 5.3: Loading curves of the ^{40}K MOT, with and without applying near resonant D1 light during loading.

The MOT settings we currently consider optimal are listed in Tab. 5.1. It

Description	Value
MOT beam diameter	≈ 25 mm
Intensity cooler	$\approx 10 I_{sat}$
Intensity repumper	$\approx I_{sat}$ (loading)
	$\approx 0.1 I_{sat}$ (after loading)
Detuning cooler	-4.1Γ
Detuning repumper	-1.5Γ
Magnetic gradient	12.5 G cm^{-1}

Table 5.1: Overview of MOT parameters currently used for trapping ^{40}K .

should be noted that due to the low complexity of our MOT laser system, the detuning used for the 2D-MOT and MOT are roughly identical and can not be varied independently⁶. As the magnetic gradient used in the 2D-MOT is very similar ($\approx 13 \text{ G cm}^{-1}$), one might argue that the best detuning values should also not be much different. Nonetheless, I regard the 2D-MOT part of the laser system to be the best starting point if one wants to increase the MOT loading rate.

⁶Repumper detunings are always identical. Cooler detunings could be varied by a few MHz as we have separate AOMs for MOT and 2D-MOT light, but using these elements for optimization would be tedious and has not been done so far. See Figure 4.26 on page 83.

5.2 Grey molasses

After collecting sufficiently many atoms in the MOT, we reduce the temperature of the sample by applying blue detuned D1 light in a $\sigma^+ - \sigma^-$, Λ -enhanced grey molasses scheme. An explanation of this cooling mechanism can be found in [159]. This intermediate cooling step is required as the temperature in the MOT is limited by the Doppler temperature. With the natural linewidth Γ , it is given by

$$T_D = \frac{\hbar\Gamma}{2k_B}$$

which is 145 μK for ^{40}K . The mean velocity at this temperature is

$$\bar{v} = \sqrt{3k_B T/m} = 0.3 \text{ m s}^{-1}$$

Prior to loading the atoms into a magnetic trap - to transport them to the measurement position - they have to be optically pumped. Optical pumping needs a well-defined magnetic dipole field as quantization axis and the magnetic quadrupole field required for MOT operation has to be switched off first. Due to the steel chamber surrounding the experiment, it takes time for the eddy currents to decay. This time is on the scale of 10 ms (estimated in 4.3.7). Over this time, the atomic cloud would increase in size by at least a factor of three (at the Doppler temperature). The mode-matching of the atomic cloud to the magnetic trap would be very poor and the resulting phase-space density after magnetic transport low.

Generally, optical molasses are considered to work best if magnetic fields are negligible. As explained in 4.5.2.2, our molasses beams have the correct circular polarization and the correct detuning (blue) to form a MOT as well - as long as the magnetic quadrupole field is present. This feature enables us to perform a smooth transition from the MOT operating conditions - with high spatial density being conserved - to molasses conditions where low temperatures are achieved. This method leads to sub-Doppler cooled samples without losing too much density. The exact procedure we currently use is as follows:

1. The red detuned D2-MOT light is ramped down in intensity to about 10% of the loading stage value.
2. In addition to the D2-MOT light, blue detuned D1 light is enabled.
3. The D2-MOT light is switched off. The quadrupole field current is ramped down in 3 ms. At the end of this ramp, the corresponding high current switch is closed to shut the current off.
4. While the quadrupole field is decaying, we keep the intensity of the D1 light constant for 25 ms.

- The intensity of the D1 light is ramped down to 10% of the initial value in 15 ms. This step is crucial for the final temperature of the gas.

We optimized this part of the experimental sequence by time-of-flight measurements with absorption imaging on the D2 line. The lowest temperature observed was 6 μK which agrees with earlier work [159]. To reach this temperature, earth magnetic field compensation by applying appropriate currents to the auxiliary coils was essential. Without compensation, the final molasses temperature rises to some 10 μK . The mean intensity required for our molasses is $\approx 10I_{sat}$ and the detuning of the cooling light 4.5Γ . For detunings of 4Γ and above no significant detuning dependence is found for the final number of atoms or the temperature as shown in Fig. 5.4.

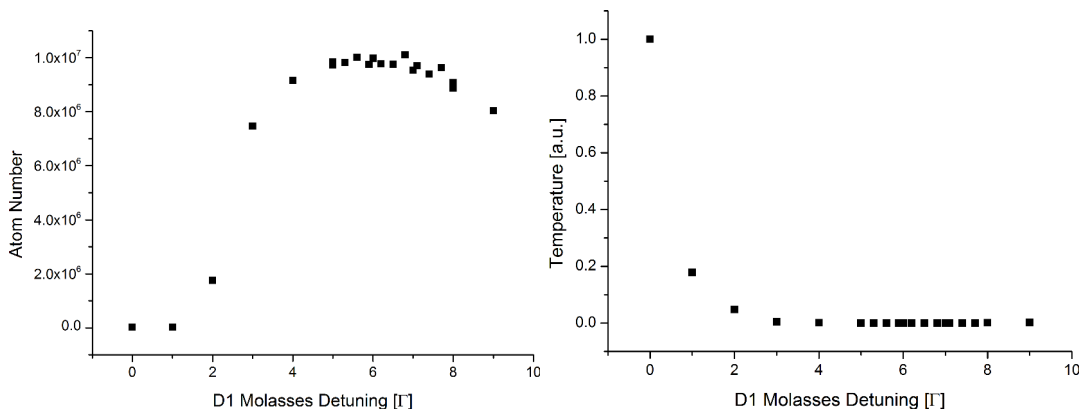


Figure 5.4: These graphs illustrates the grey molasses performance in terms of final atom number and temperature for different D1 cooler detunings.

A crucial parameter of the Λ -enhanced molasses is the so-called “Raman detuning”: If the frequency difference between D1 cooling and repumping light - this is exactly the frequency fed to the EOM in our D1 laser system, see Figure 4.29 on page 85 - is equal to the ground state splitting of 1286 MHz, these two lasers couple the ground states via a two-photon transition. This coupling leads to the occurrence of additional dark states making the cooling scheme more efficient.

The Raman detuning has to be adjusted carefully as the Raman resonance is only few a 100 kHz broad. This parameter strongly affects both the final temperature and the number of atoms. Our experimental results demonstrating the Raman resonance are shown in Fig. 5.5.

5.3 Optical pumping

At the end of the grey molasses sequence, the atoms are completely free from magnetic fields. Next, the current through the “Raman” coils is set to its

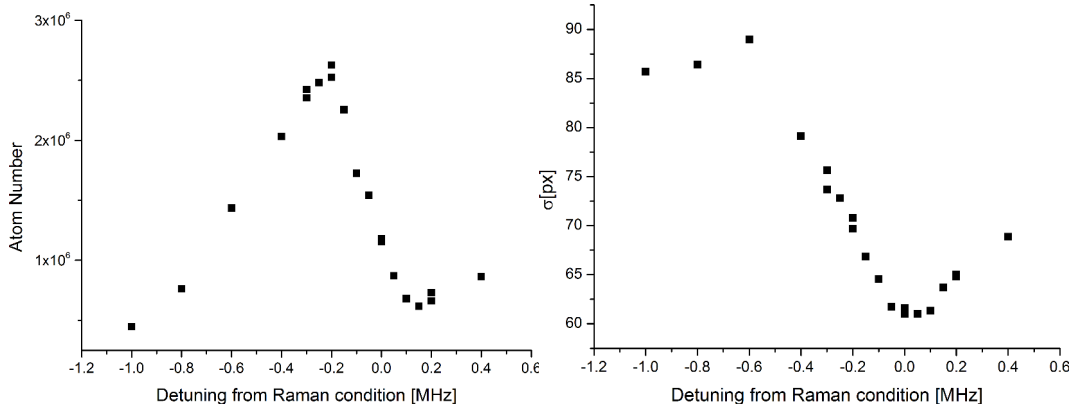


Figure 5.5: Raman resonance condition observed in the atom number (left) and the width of the atom cloud after a fixed time-of-flight of 14 ms (right). The highest atom number is achieved for a frequency about 200 kHz below the value given by the ground state splitting.

maximum value. After a wait time of 1 ms, both m_F - and F-pumping light are turned on. The m_F -pump light is applied for 100 μ s, F-pump for 150 μ s. At the time we were setting up the optical pumping and magnetic trapping sequence, we were not capable of measuring the fidelity of the optical pumping process. The number of magnetically trapped atoms served as a figure of merit for the optimization. Later, when we were capable of doing m_F -sensitive spectroscopy using our microwave system presented in 5.7.1, it turned out that our optical pumping fidelity was far from optimal caused primarily by impurely polarized pumping light.

5.4 Capturing and transporting atoms magnetically

During the optical pumping sequence, the MOT coil power supply is set to the current of 30 A used for capturing the atoms. The power supply loads its internal capacitors to the maximum voltage value as the high current switch is still closed. The atoms are captured directly upon the end of pumping light application by opening the high current switch. Then, the pumping quantization field is ramped down quickly and the magnetic trapping current flowing through the MOT coils is ramped up to 170 A within 100 ms. The magnetic trap is moved over a distance of 4 cm by lowering the current flowing through the MOT coils and increasing the current through the coils centered around the microscope. To make this movement smooth and to roughly preserve the geometry of the trap, the currents are ramped as $\sin^2(t)$ and $\cos^2(t)$ functions as shown in Fig. 5.6.

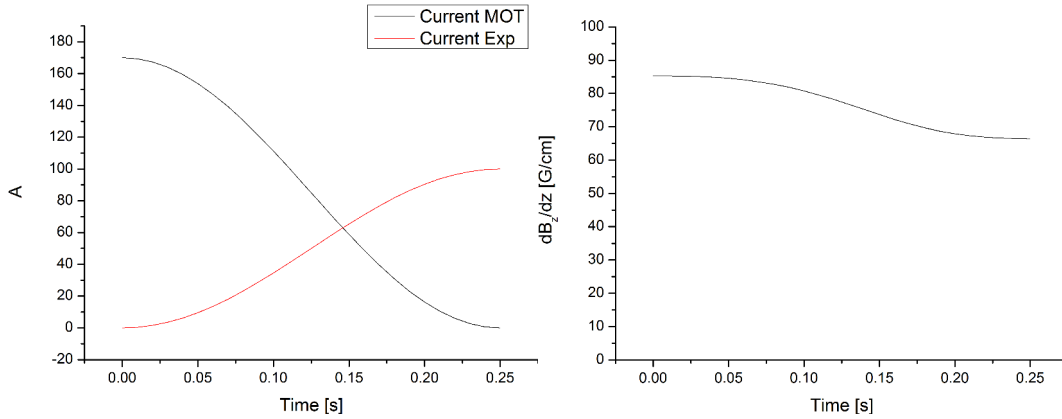


Figure 5.6: Current ramping sequence for magnetic transport with an almost constant gradient. The coil pair centered around the experiment position is closer to the atoms so the current required is lower. At the final position, the gradient is slightly weaker than at the MOT position with the parameters currently used.

As depicted in Fig. 5.7, the transport leads to a maximum acceleration of about 400 cm s^{-2} - about two orders of magnitude lower than the acceleration caused by the static trapping potential. Heating effects caused by the transport should

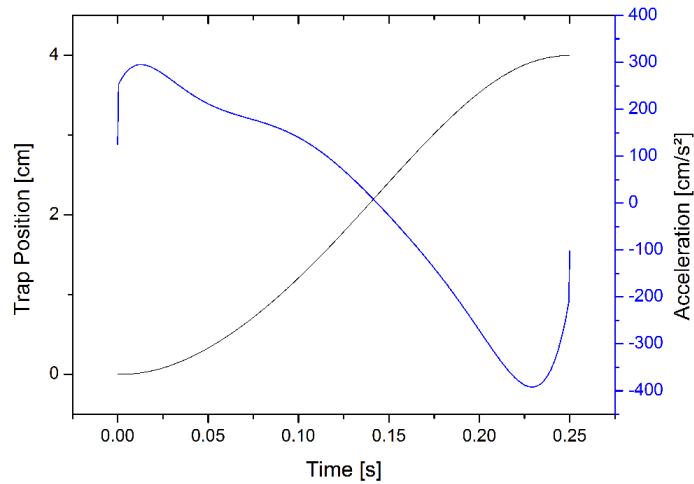


Figure 5.7: Resulting trap movement and acceleration due to the applied transport scheme.

be negligible. Time-of-flight measurements can not be performed properly out of a magnetic trap due to the slow decay of the trapping potential caused by eddy currents. Rough temperature estimates relying on single absorption images of the atomic cloud while still magnetically trapped suggest that the sample is not significantly heated by optical pumping, magnetic capture or

magnetic transport.

5.5 Loading of lattice and tweezers

I shall next present the steps required for transferring the atoms from the magnetic confinement to optical dipole traps.

5.5.1 Alignment of atom traps

The magnetic trap at the end of the transport sequence as well as the optical traps have to be aligned within the FOV of our high resolution imaging system, which is about 200 μm in diameter. This alignment is performed by evaluating absorption images of the atoms. The position of the objective lens assembly in the vacuum chamber is not defined very accurately and reference points outside the chamber are only useful for approximate alignment.

The initial alignment of the coils was performed in an early stage of commissioning by moving the coil assembly on the optical table and adjusting the height while monitoring the position of the MOT.⁷ Now, the coil assembly is constrained by current and cooling water connections and can not be moved. The final position of the magnetically trapped atoms after transport is adjusted by applying appropriate currents to the offset coils. We could easily shift the trap position by some 100 μm . To reference the position we primarily used parts of the objectives, which are also visible on the absorption images taken along two perpendicular axes. One of these imaging axes passes through two small holes drilled through the pylons connecting upper and lower part of the objective assembly, see Figures 4.19 on page 72 and 5.8.

Images of the status before offset field alignment are shown in Fig. 5.9. The largest displacement visible in this figure is about 1 mm.

Another strategy used to ensure the alignment of our atomic sample with respect to the microscope was to feed in near-resonant D2 light through the upper objective as a position marker. This light renders parts of the cloud transparent by saturating the atomic transition. Depending on whether or not this marker light is collimated prior to entering the microscope, the resulting images show conical or tubular structures on the atomic clouds. Typical examples of such images are shown in Fig. 5.10. If perfect alignment of the marker beams with respect to the microscope is ensured, this is a very reliable technique for aligning the atomic sample.

The adjustment of the 850 nm horizontal lattice axes used for precooling and practicing purposes was more difficult. In the focus, these lattice beams are

⁷The MOT was prepared with stronger magnetic gradients than usual to reduce the influence of light-induced forces.

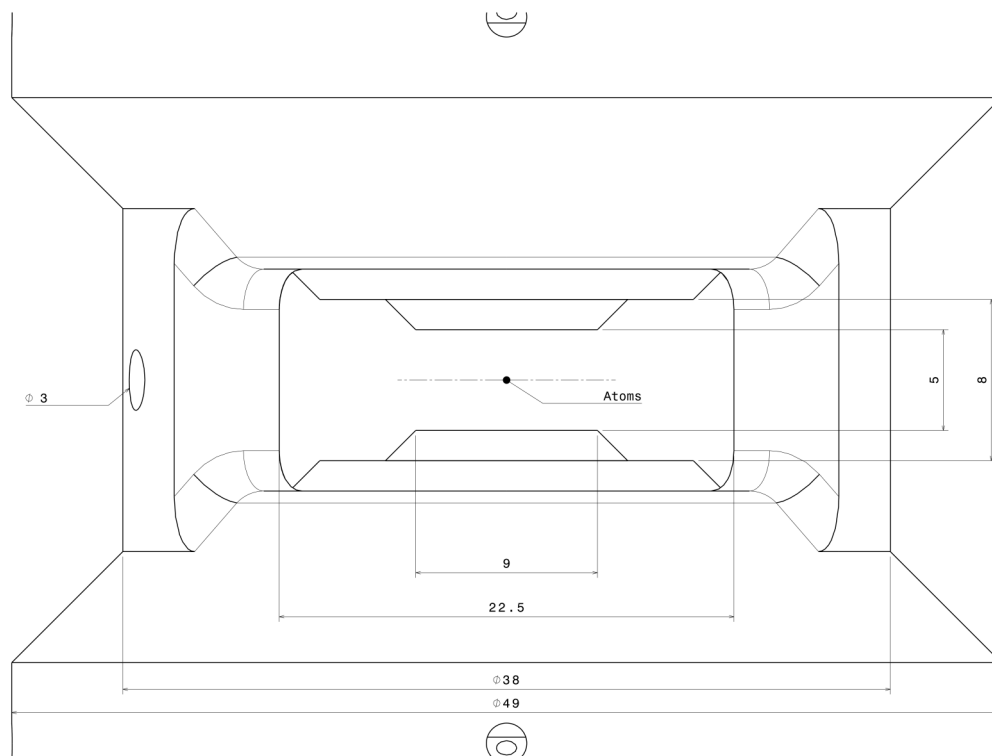


Figure 5.8: Sketch of the microscope parts surrounding the measurement position with an enlarged scale. Here, only one of the $\varnothing 3$ mm holes is visible.

supposed to have a waist of $30\ \mu\text{m}$. A dichroic mirror located between the focusing achromat and the atoms is necessary to be able to apply D1/D2 light along the lattice beams. It introduces aberrations complicating the alignment procedure, see Figure 4.34 on page 91. To achieve a minimal focus at the correct position, we carried out the following steps:

1. Ensure perfect collimation and small aberrations in front of the focusing achromat using a shearing interferometer.
2. Place the focusing achromat at the correct distance from the measurement position. With a Rayleigh range of about 3 mm, choosing the correct distance is not critical.
3. Roughly align the lattice beam to the correct direction. It should not hit the windows perpendicularly. An infrared viewing device is useful for observing how the lattice light hits mechanical parts of the microscope assembly.
4. Place a silver mirror directly in front of the vacuum chamber and image the light on a CCD camera. Minimize the spot size in the focal plane by tilting the focusing achromat such that errors introduced by the dichroic mirror are compensated.

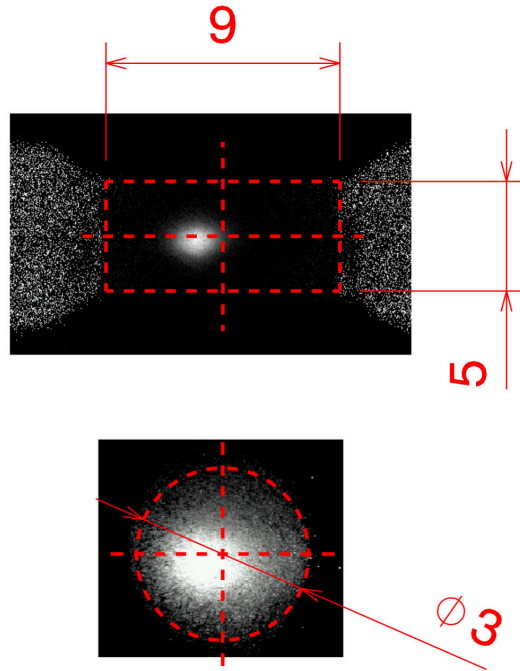


Figure 5.9: Two absorption images taken for the purpose of aligning the magnetic trap. The upper one is taken along the axis used for the magnetic transport, the lower one along the small holes drilled into the microscope assembly. These axes are approximately perpendicular.

5. Remove the mirror. Image the magnetically-trapped atomic sample along the lattice beam. In a weak magnetic trap⁸, the density excess produced by the optical dipole trap can be easily observed. The position of this feature is then moved to the center of the FOV of the microscope.
6. On the rear side of the chamber, the re-collimating achromat is shifted and tilted such that the light is collimated and has minimal aberrations using a shearing interferometer.
7. Retro-reflect this beam using a silver mirror such that a second density excess becomes visible on the absorption images and overlap both features.

Some absorption images taken during this process are shown in Fig. 5.11. Using this technique, both lattice arms are walked to the position indicated by the cone-technique described above. Finally, after cooling the atoms into the lattice and switching the magnetic confinement off, the y-lattice becomes visible in the imaging along the x-axis and vice versa. This is used for fine tuning the relative positioning of the lattice arms. At this level, it is possible to collect D1 fluorescence light with the lower microscope objective when illuminating

⁸25 A is a good value for the current through the Exp coils.

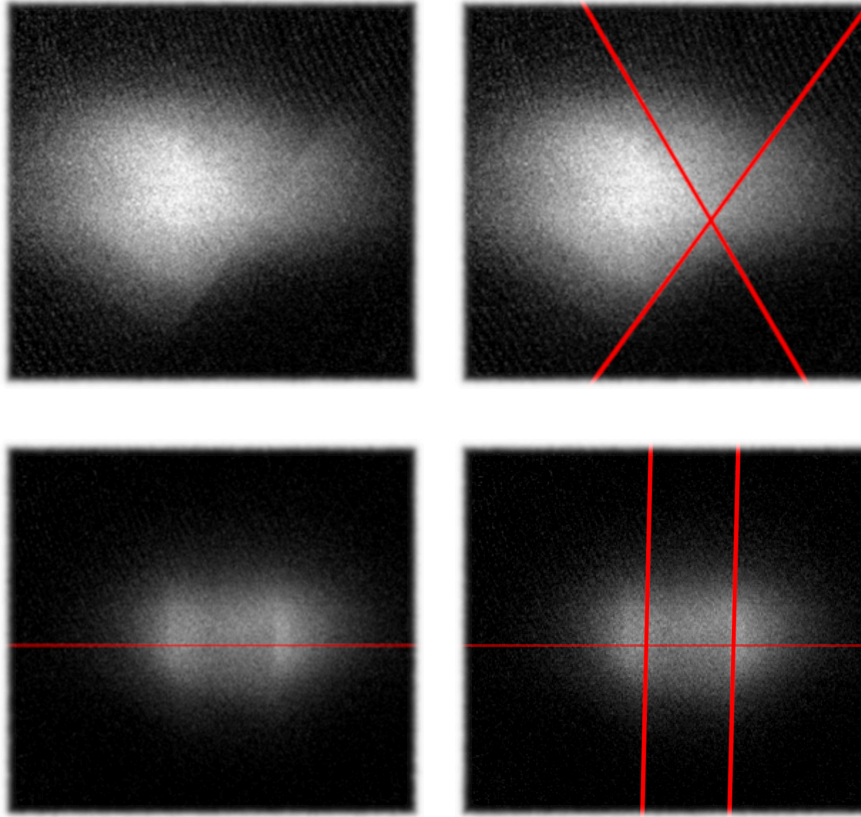


Figure 5.10: Absorption images showing the effect of D2 imaging light being passed through the microscope assembly. In the upper row, this light is collimated before entering the microscope, mimicking an optical tweezer. In the lower row, the light is focused into the microscope such that the beam is collimated at the atomic cloud position. This technique of producing a collimated beam along the vertical axis, as described in more detail in 4.5.3, is used for other beams as well.

the sample with D1 light from the side. In these fluorescence images, both lattice arms are visible.

5.5.2 Loading procedure

Loading the cold atoms from the magnetic trap to an optical dipole trap is a crucial step in the experimental sequence. For all kinds of optical traps we use in this experiment - optical lattices, running wave traps with large waists and optical tweezers - we apply an identical scheme based on D1 grey molasses cooling. For the different trap geometries, there are only minor differences in the parameters.

The D1 beams have circular polarizations that are identical to the molasses beams used at the MOT position. To ensure power balancing, we use two separate beams on the vertical axis whereas along the horizontal axes, the

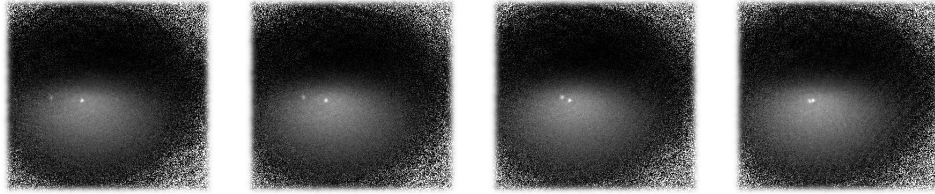


Figure 5.11: Absorption images taken along one of the lattice beams during the process of overlapping the running waves to form an optical lattice. The atoms are confined in a weak magnetic potential, the asymmetry of the cloud is caused by gravity.

D1 beams are retroreflected. Loading the optical potentials follows a simple scheme: The optical potential is applied in addition to the magnetic confinement. Blue detuned D1 light is applied for 20 ms while ramping the intensity linearly to 20% of its initial value. Afterwards, the magnetic confinement is slowly ramped down.

We characterized this procedure but do not understand the details of the underlying mechanisms. All six D1 beams are important for the loading to work properly. Our optimization showed that the parameters are very similar to those used in the grey molasses phase after MOT loading. A plot of the loading characteristics of the lattice with and without molasses light is shown in Fig. 5.12. The dependence on D1 cooler detuning as well as the initial and final

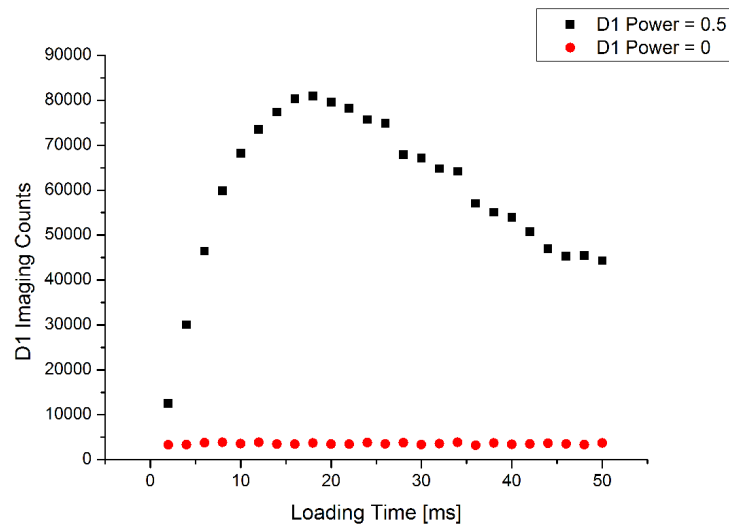


Figure 5.12: Loading curve for the optical lattice. The “loading time” denotes how long the D1 light was enabled during lattice loading. Later, the trapped atoms are illuminated with D1 light again and the collected fluorescence serves as a measure for the number of trapped atoms. Without applying any molasses light, a very small fraction of atoms is loaded. In the data shown here, the D1 light increases the loading efficiency by a factor of 20.

powers are shown in Fig. 5.13. In contrast to the pure molasses case, we do

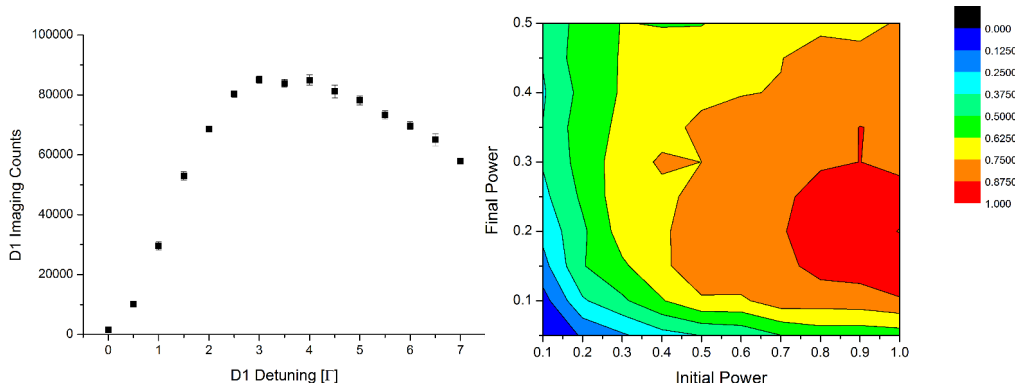


Figure 5.13: Dependence of loaded atoms on detuning and power of the applied D1 light. Compared to the case of pure grey molasses presented in Sec. 5.2, the behavior for different detunings is similar but it starts to work at smaller detunings and shows a more pronounced tail at larger detuning. The data for the power dependence suggests that higher loading efficiencies can be achieved with higher overall power. For all points in this graph, the power was ramped from the initial to the final value in 20 ms.

not observe a Raman condition for the repumping light frequency here. From time-of-flight measurements using absorption images, we deduced the temperature of the optically trapped atoms to be about $25 \mu\text{K}$. The temperature did not show any particular dependence on any of the molasses parameters.

5.6 Lattice

Our apparatus is equipped with a far detuned optical lattice formed by two pairs of retroreflected laser beams. The resulting optical traps have a tubular geometry in the intersection region of the lattice axes. The laser source was described in 4.5.1.3 and the optical system at the experiment in 4.5.2.3. Currently, we use the optical lattice as an intermediate step on the path to single atoms in optical tweezers. It is particularly useful for practicing RSC, as much more signal is provided than with single atoms. The atoms trapped in a lattice can be imaged in several ways:

- Absorption imaging systems along the lattice axes. They have the drawback that they integrate along the entire lattice and thereby also take into account atoms located outside the intersection region of the lattice beams. For measuring the total number of atoms trapped in the lattice, these imaging systems are useful. The highest atom number we have observed so far was about 3×10^5 .
- We can record absorption images along the microscope axis.

- We can image D1 fluorescence that is scattered when feeding in the D1 blue detuned molasses beams. We have to disable the vertical molasses beams because otherwise, the sensitive camera used for fluorescence imaging would receive too much stray light.
- The D1 pumping photons scattered as part of the RSC process are imaged through the microscope as well.

An example of a typical fluorescence image acquired using our microscope assembly is given in Fig. 5.14. The biggest advantage of using the microscope in lattice experiments is that it allows us to evaluate small regions of the sample and thereby reduce effects caused by spatial inhomogeneity.

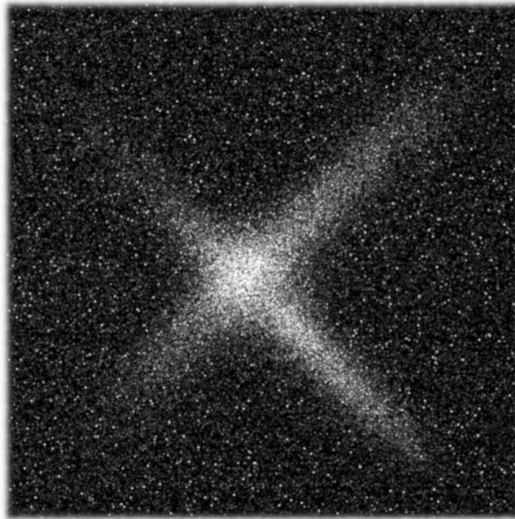


Figure 5.14: D1 fluorescence image of ^{40}K atoms trapped in a 850 nm optical lattice imaged with our high resolution imaging system. A significant fraction of the atoms is located outside the intersection region of the lattice beams.

We have investigated some of the key properties of the optical lattice to verify the operational parameters and for future reference.

5.6.1 Trap frequencies

To check that our 850 nm optical lattice is set up properly, it is useful to measure the resulting trap frequencies. Due to the Gaussian beam profile and the small size of the lattice, the trap frequency varies spatially and is broadened due to anharmonicity. To obtain a clearer signal, we have measured the trap frequency on each lattice axis individually. As the lattice beams have perpendicular polarization, this does not change the observed trap frequencies. Two techniques for measuring trap frequencies are:

1. Parametric heating loss by modulating the laser power in a lattice arm
2. Raman-induced D1-fluorescence spectra (see 5.7.2)

To measure the trap frequency before commissioning the Raman laser system, the lattice power was modulated with frequencies in the range where the trap frequency is expected by varying the amplitude of the RF signal fed to the AOM used for power stabilization and fast switching. The intensity variations drive parametric heating when the modulation is close to the trap frequency. The atom loss resulting from this process is detected in an absorption measurement.

During modulation, the intensity stabilization of the lattice beams is enabled, but the bandwidth of the PID controllers used for this is not high enough to counteract the modulation. Due to the properties of the RF-system, the modulation amplitude is not constant over the frequency range investigated: At 600 kHz, we measure a modulation depth of 2.5 %, whereas at 50 kHz we measured 7 %. Nonetheless, one obtains a meaningful loss spectrum when modulating the lattice for 12.5 ms, see Fig. 5.15. The plot shows two dips.

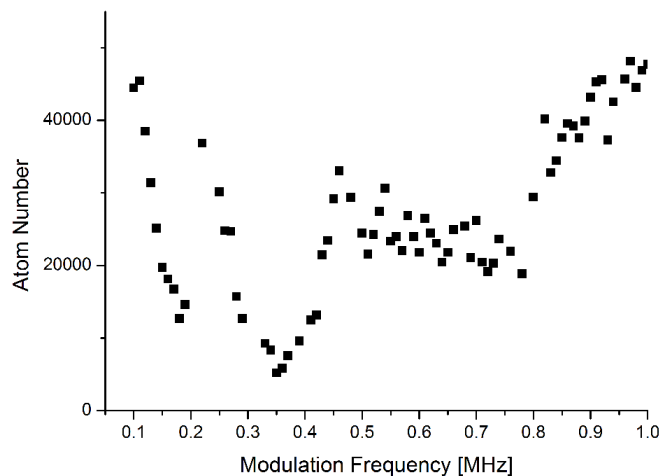


Figure 5.15: Loss spectrum taken by modulating one of the lattice arms at different frequencies to determine the trap frequency. The measurement indicates a trap frequency of about 175 kHz which fits to the value expected at 300 mW.

The dip at about 175 kHz is due to $|n\rangle \rightarrow |n+1\rangle$ transitions while the one at twice this frequency corresponds to $|n\rangle \rightarrow |n+2\rangle$ transitions. The latter have a higher probability because these transitions conserve the symmetry of the wavefunction.

5.6.2 Lifetimes

We have measured the lifetimes in the optical lattice and in the running-wave trap obtained by blocking the retro-reflectors. The atom number has been determined by absorption imaging. Shortly before illuminating the sample, F-pumping light was applied to clear the $|^2S_{1/2}, F = 7/2\rangle$ state. The respective plots are shown in Fig. 5.16. The lifetimes of the optical lattice are much

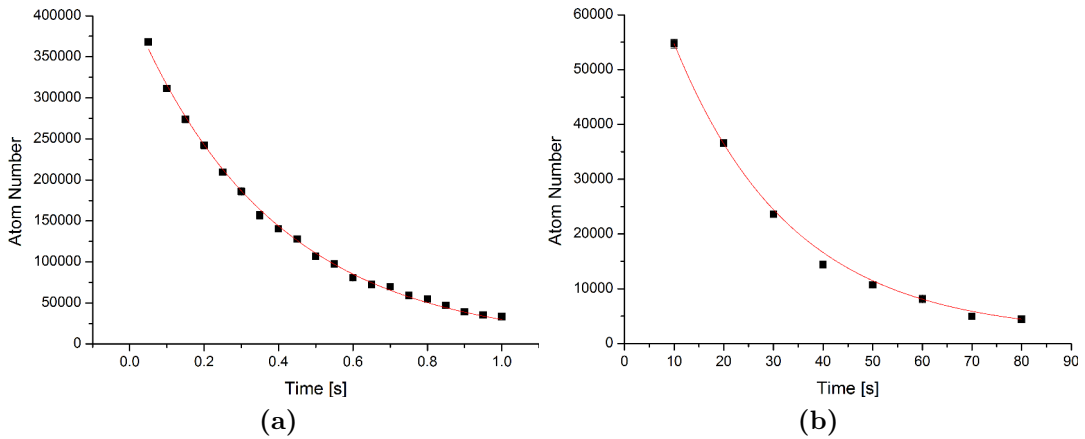


Figure 5.16: Lifetime measurements in the optical lattice (a) and the corresponding running-wave trap (b) where both lattice retro-reflexes have been blocked. The error bars are too small to be visible. For the lattice, we measured an exponential decay constant of 382 ms, for the running-wave trap 23.7 s.

shorter due to parametric heating processes. As we had previously measured a lifetime of about 95 s for magnetically trapped atoms, we assume the lifetime of the optically trapped atoms to be limited by light scattering as well as parametric heating.

5.7 Preparations for Raman sideband cooling

To prepare the atoms in the ground state of the harmonic oscillator potentials, Raman sideband cooling is required to remove the last motional quanta. The D1 grey molasses-based loading procedure described above results in mean occupational numbers of $\langle n \rangle \approx 2$, which is a good starting point for RSC. Nonetheless, achieving high-fidelity ground-state cooling involves several technical difficulties and relies on many experimental parameters being chosen correctly. This section reports on the steps we have made so far on the path to reliable ground-state cooling.

5.7.1 Microwave spectra

We can drive transitions between the $|^2S_{1/2}, F = 9/2\rangle$ and $|^2S_{1/2}, F = 7/2\rangle$ ground states using the corresponding microwave transition at about 1286 MHz with the single loop antenna included into the vacuum chamber (see 4.2.3.5). This is particularly useful:

- It enables us to transfer the atoms to $|^2S_{1/2}, F = 7/2\rangle$ without any heating. As long as the atoms are in this state, they are “hidden” in the sense that they are not affected by most of the applied laser frequencies.
- One can easily resolve transitions between different m_F -states. This is an important tool for optimizing the optical pumping processes.
- The resulting spectra can be used to investigate the magnetic field stability.

The transitions observed in microwave spectroscopy occur at the same frequencies as the carrier transitions in the Raman spectra if applied magnetic fields and light fields are identical. This made microwave spectroscopy an important intermediate step on the way to RSC.

5.7.1.1 Microwave generation

We create the microwave signal using a DDS source controlled by our experiment control computer in the same way as described in 4.5.1.4 for the Raman AOM signals. To amplify the signal, we use a high power amplifier⁹ that is capable of handling open-loop and short circuits. This amplifier provides up to 10 W output power, but we only require some 100 mW. It could drive the

⁹Mini Circuits ZHL-10W-2G+

antenna without any matching circuit without damage, but we use¹⁰ a stub-tuning device for matching the antenna to $50\ \Omega$. The stub is realized by an open coaxial cable connected to an SMA-tee in the transmission line between amplifier and antenna. The matching can be optimized at the corresponding frequency by changing the length of the stub cable. During matching, the circuit is connected to a vector network analyzer and the s-parameter S11 is measured. Results for the unmatched antenna and for an antenna with a matching stub of incorrect length are shown in Fig. 5.17.

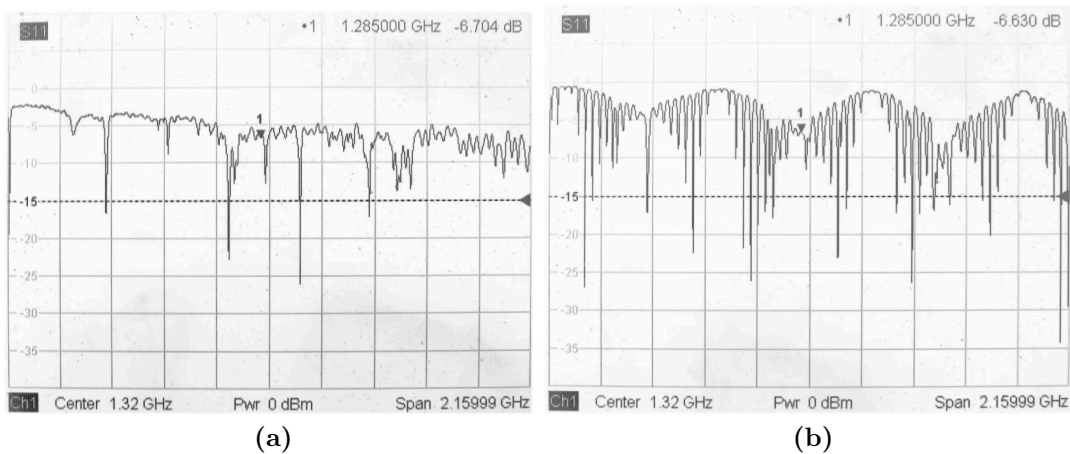


Figure 5.17: Reflection spectrum of the microwave antenna without (a) and with matching circuit (b). The resonances that appear when using the matching circuit can be shifted by varying the length of the tuning stub until a resonance is located at the desired frequency.

We could improve the matching further by using two stubs. The reflection could be suppressed down to $-45\ \text{dB}$. This matching is good only over a few MHz, as can be seen in Fig. 5.18. In the picture shown here for illustration, we have matched the antenna to the zero-field transition frequency. This matching is good for fields up to 1 G. For larger magnetic fields, the matching stub has to be changed.

5.7.1.2 Resolving m_F -spectra

The center of the microwave antenna is located at a distance of about 50 mm from the atoms and the axis defined by the antenna’s single coil winding meets the magnetic quantization axis - defined by the “Raman” coil pair - at an angle of 45° . Hence, we are operating in the near field and the radiated polarization

¹⁰After this text was written, we recognized that the matching circuit is not essential, as we have sufficient microwave Rabi rates even if a lot of power is reflected at the antenna. If the expensive ZHL-10W-2G+ amplifier is replaced with an amplifier not capable of handling reflected power, the matching information given here becomes relevant again.

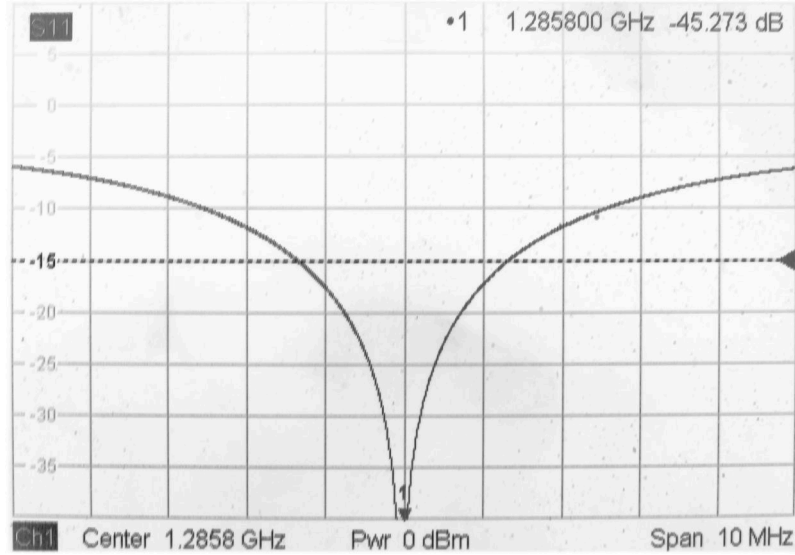


Figure 5.18: Reflection spectrum of matched microwave antenna.

is capable of driving all dipole-allowed transitions. The different m_F -states experience different Zeeman shifts. Taking the selection rule $\Delta m = 0, \pm 1$ into account, one observes frequency shifts compared to the 0-field case as given in Tab. 5.2.

MHz/G	$F=7/2 \rightarrow$	$7/2$	$5/2$	$3/2$	$1/2$	$-1/2$	$-3/2$	$-5/2$	$-7/2$
$F=9/2 \downarrow$									
$9/2$		-2.5	x	x	x	x	x	x	x
$7/2$		-2.19	-1.88	x	x	x	x	x	x
$5/2$		-1.88	-1.56	-1.25	x	x	x	x	x
$3/2$		x	-1.25	-0.94	-0.63	x	x	x	x
$1/2$		x	x	-0.63	-0.31	0	x	x	x
$-1/2$		x	x	x	0	+0.31	+0.63	x	x
$-3/2$		x	x	x	x	+0.63	+0.94	+1.25	x
$-5/2$		x	x	x	x	x	+1.25	+1.56	+1.88
$-7/2$		x	x	x	x	x	x	+1.88	+2.19
$-9/2$		x	x	x	x	x	x	x	+2.5

Table 5.2: Transition frequency shifts for m_F -transitions between $|^2S_{1/2}, F = 9/2\rangle$ and $|^2S_{1/2}, F = 7/2\rangle$.

In our experiment it would be ideal to have all atoms in one of the outermost m_F -states which would result in observing exactly one microwave transition. But as our optical pumping is not perfect - and was indeed very poor before we were able to use microwave spectroscopy - we observe more than one transition. One of the early microwave spectra is shown in Fig.

5.19. Here, the atoms were supposed to be in the magnetically trapped state

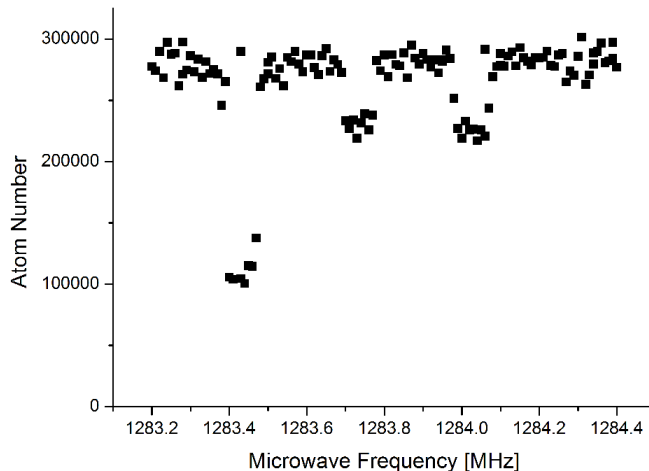


Figure 5.19: Microwave spectrum of atoms trapped in the optical lattice prior to optimization, recorded using absorption imaging. This spectrum was taken by enabling the microwave source for 10 ms at a fixed frequency and a power of about 1 W. Some of the atoms are transferred to the $|^2S_{1/2}, F = 7/2\rangle$ state which is dark for our absorption imaging light. One observes three resonances, which means that the sample had not been prepared in a pure m_F -state. The features correspond to the transitions $|F = 9/2, m_F = 9/2\rangle \rightarrow |F = 7/2, m_F = 7/2\rangle$ (strongest), $|F = 9/2, m_F = 7/2\rangle \rightarrow |F = 7/2, m_F = 7/2\rangle$ and $|F = 9/2, m_F = 7/2\rangle \rightarrow |F = 7/2, m_F = 5/2\rangle$.

$|F = 9/2, m_F = 9/2\rangle$ but inadequate pumping lead to about 1/3 population in the state $|F = 9/2, m_F = 7/2\rangle$. In addition, the transitions were broadened by applying the microwave radiation while the magnetic field was still changing. We investigated this by varying the time between ramping down the magnetic confinement and microwave application and could observe how the transition frequency shifts for some 10 ms. Measurement results illustrating this behavior are shown in Fig. 5.20. These measurements indicate that magnetic field changes persists for much longer times than expected in our apparatus. An estimate for the timescale was presented in 4.3.7. So far, we do not understand whether this observation is only caused by eddy currents, or by some other technical problems. We decided to avoid the issue by choosing sufficiently long waiting times.

After we had obtained a better understanding of our microwave spectra, we used them for optimizing the optical pumping sequence. The correct $\lambda/4$ -waveplate to create the circularly polarized pumping light¹¹ and its proper alignment were particularly important. In Figure 5.21 the occupation of unwanted states is much smaller than before. The atoms were pumped into the

¹¹It is a difference, whether a low-order waveplate is made for D1 or D2 light.

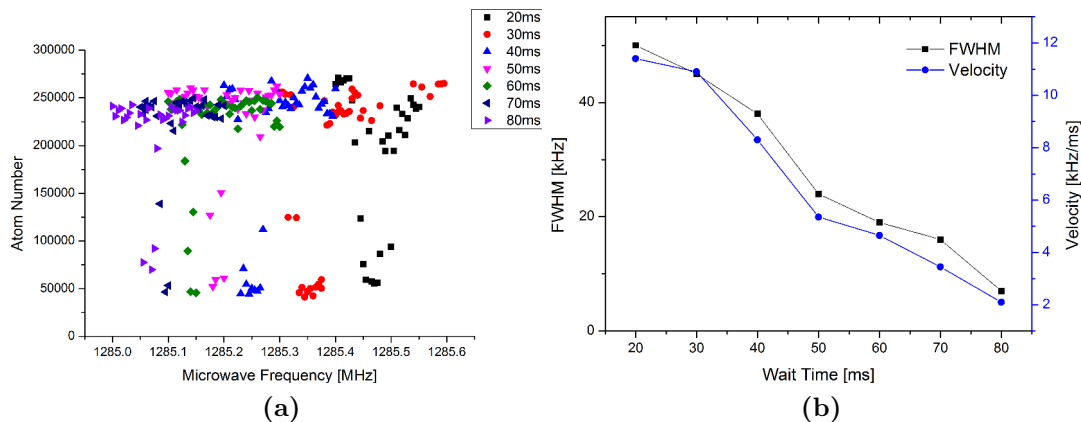


Figure 5.20: Microwave spectra recorded with different waiting times after the last changes in magnetic field (a). The measured linewidth and the velocity are greatly reduced after longer waiting times (b).

magnetically anti-trapped state $|F = 9/2, m_F = -9/2\rangle$ before recording the spectrum. This end of the m_F -spectrum is chosen for experiments as there exist easily accessible Feshbach resonances [160]. To reverse the direction of the optical pumping process, the current flow in the “Raman” coil pair is reversed. For this spectrum, we applied what we call the “blowout” technique: The microwave excites atoms to the upper hyperfine level, and subsequently non-excited atoms are removed from the trap by using resonant D2 cooler light. The remaining atoms are then imaged with D1 fluorescence.

5.7.1.3 Rabi oscillations and compensation of magnetic field fluctuations

When recording the first microwave spectra, we did not operate the microwave at a fixed frequency but performed frequency sweeps instead. With sweep ranges of typically 10 kHz and sweeping rates of 1 MHz s^{-1} , we obtained the most reliable results. This technique is not very useful for determining the (broadened) linewidth of the transition nor for Rabi cycles. By reducing the sweep interval, we aimed at obtaining a first estimate of the linewidth. The smallest upper limit we could determine for the observed linewidth using the sweeping technique was 5 kHz, see Fig. 5.22. This result indicates that stability of the magnetic field was limited to some mG.

After our first attempts to observe Rabi oscillations failed, we were certain that this must be due to insufficient magnetic field stability. The estimated field fluctuations were too large to be explained by current noise of our high-end power supplies, so the next most likely source of fluctuations was 50 Hz mains supply. To test this hypothesis, we synchronized the experimental cycle to the mains by stopping the clock of our experiment control devices until the

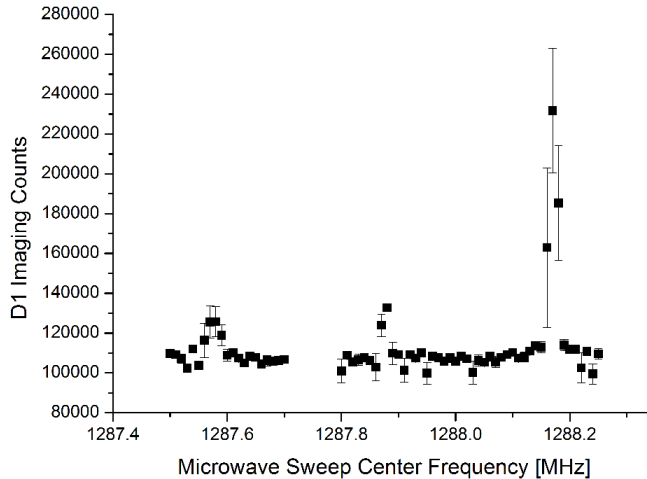


Figure 5.21: Microwave spectrum of the interesting frequency range recorded by sweeping the microwave frequency over 20 kHz in 10 ms using the “blowout” technique described in the text. Visible are the transitions $|F = 9/2, m_F = -9/2\rangle \rightarrow |F = 7/2, m_F = -7/2\rangle$ (strongest), $|F = 7/2, m_F = -7/2\rangle \rightarrow |F = 7/2, m_F = -7/2\rangle$ and $|F = 7/2, m_F = -7/2\rangle \rightarrow |F = 7/2, m_F = -5/2\rangle$. When we recorded this spectrum, we operated with an offset field of about 1 G. Later, when pushing Raman cooling attempts, we went to a higher offset field for improved separation of the m_F -transitions.

next rising zero crossing of the mains voltage. It is important to do this only few 10 ms prior to the time where good field stability is required, as the mains frequency is not very well-defined and the coherence time is rather short.¹² Applying this synchronization has an impressive effect on the visibility of Rabi oscillations, see Fig. 5.23.

To quantify the effect of magnetic field fluctuations arising from the electricity supply, we used the synchronization tool in the following way: First the experiment is synchronized, after a variable waiting time, a microwave spectrum is recorded. The center frequency of the microwave transition then depends on the waiting time. In Figure 5.24a the center frequency shows a clear 50 Hz oscillation.

One can think about two different approaches for compensating this magnetic field instability using additional currents:

- One can measure the unwanted magnetic field with a sensitive gauge and feed the acquired signal back to power supplies providing compensation currents. This would require additional hardware.

¹²In Europe, EN50160 requires a frequency of 49.5 Hz to 50.5 Hz for 99.5% of the year. During 0.5% of the year, a frequency between 47 Hz and 52 Hz is tolerated. To check conformity, the frequency measurements average over 10 s.

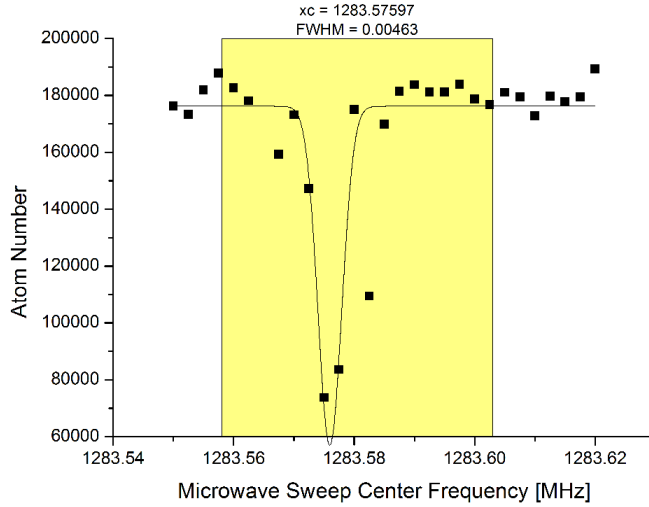


Figure 5.22: Line of the transition $|F = 9/2, m_F = 9/2\rangle \rightarrow |F = 7/2, m_F = 7/2\rangle$ taken at 1 G offset field with static external fields compensated. Recorded by enabling the microwave source for 1 ms and sweeping the frequency over 5 kHz during this time prior to absorption imaging. Power was about 500 mW. The fitted linewidth is limited by the frequency sweep. Using a smaller sweep range lead to noisy signals which suggests field fluctuations on the few mG scale.

- If one assumes a certain waveform for the field fluctuation one can easily compensate for it by applying the same waveform on top of existing offset currents. Then, one just has to find appropriate amplitudes for the modulation. This takes some time but is technically not complex, in particular due to our atoms being a very sensitive and well understood magnetic field sensor.

At the time this thesis is being written, we decided to use the second approach. We assume that the field fluctuation has a sinusoidal waveform with 50 Hz. As a first step, we apply a corresponding current modulation only to the “Raman” power supply. This is the easiest solution but it reduces the field instability dramatically as shown in Fig. 5.24b.

The combination of mains synchronization and feed-forward compensation current enabled us to observe a beautiful Rabi oscillation for many Rabi cycles. With the current field stabilization strategy, decoherence becomes relevant after about 6 ms. A plot from which the Rabi frequency is derived, is shown in Fig. 5.25.

It is not clear yet, to what extent a further magnetic noise reduction is required. Possible candidates for improvements are:

- Add a current regulation to the power supplies. By this, the current stability could be pushed below 1×10^{-4} .

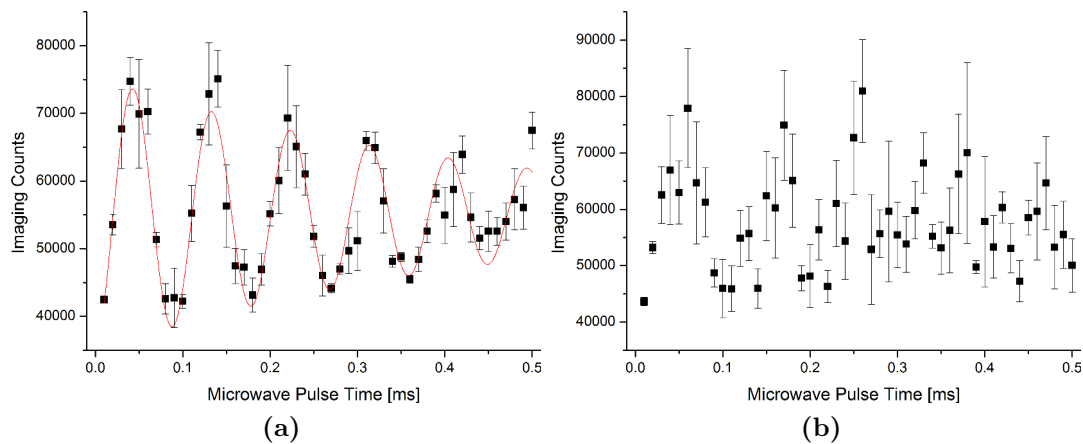


Figure 5.23: Attempts to observe Rabi oscillations on the microwave transition with (a) and without (b) synchronizing the experiment to 50 Hz mains voltage. The synchronization was performed 250 ms before the microwave spectroscopy. Here, no compensation is applied for magnetic field noise. In consequence, the Rabi oscillation decoheres after a few hundred microseconds.

- Adding active magnetic field stabilization.
- Improve the current feed-forward scheme. Besides applying the technique to other offset currents, one might also think about deriving the modulation signal from a measurement of the actual mains voltage. This might be particularly effective, as the mains has a voltage tolerance of $\pm 10\%$. It seems likely that this rather wide voltage tolerance is the ultimate limiting factor of the feed-forward approach.

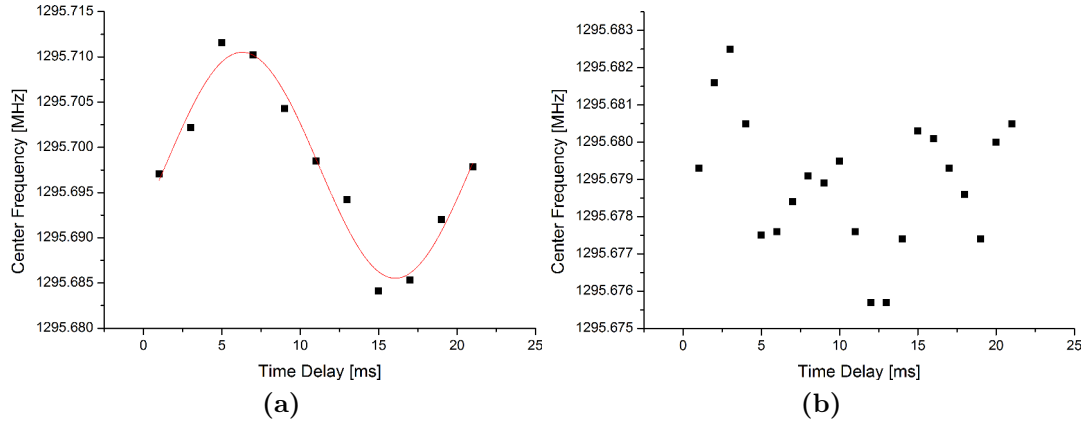


Figure 5.24: The center frequency of the microwave transition moves in time due to magnetic field noise. At $t = 0$, the experiment is synchronized to the mains frequency. (a) shows the case where no compensation current is applied to reduce the field fluctuations. Translated into the amplitude of the magnetic field oscillations, this plot suggests field fluctuations of 5 mG. When taking plot (b), most of the noise was canceled by applying a sinusoidal compensation current along one axis.

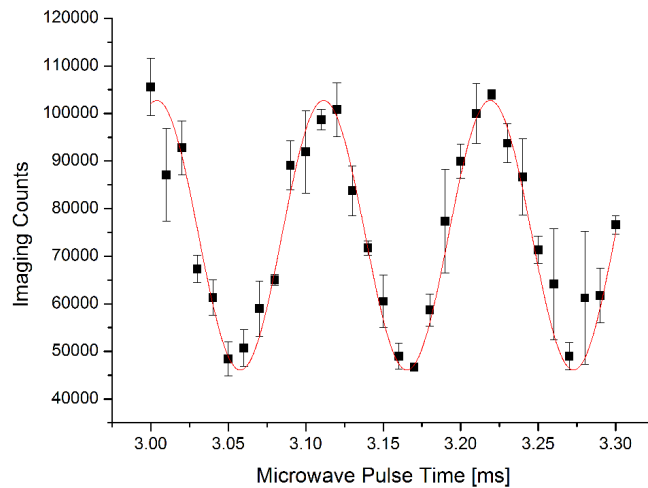


Figure 5.25: With mains synchronization and feed-forward magnetic field stabilization, we were able to drive a Rabi oscillation over many Rabi cycles. The measured Rabi frequency is 9.3 kHz.

5.7.2 Raman spectra

Key ingredient to Raman sideband cooling is the capability to resolve the vibrational states spectroscopically. In neutral alkali atoms, the natural linewidths of commonly used optical transitions is much larger than the trapping frequencies. To achieve the required frequency selectivity nonetheless, we use a two-photon transition to couple the states $|^2S_{1/2}, F = 9/2\rangle$ and $|^2S_{1/2}, F = 7/2\rangle$ by shining in two laser beams that are far detuned from the D2 transition. The frequency difference between these beams is matched to the required transition frequency. The natural linewidth of this transition is negligible - the upper state has a long lifetime. In the experiment, the transition is broadened to some kHz due to magnetic field fluctuations. A scheme of our Raman cooling is shown in Fig. 5.26: When tuned to the red sideband, the Raman lasers coherently drive the transition

$$|^2S_{1/2}, F = 9/2, m_F = -9/2, n\rangle \leftrightarrow |^2S_{1/2}, F = 7/2, m_F = -7/2, n - 1\rangle$$

In the ideal case, the population could be shuffled back and forth between

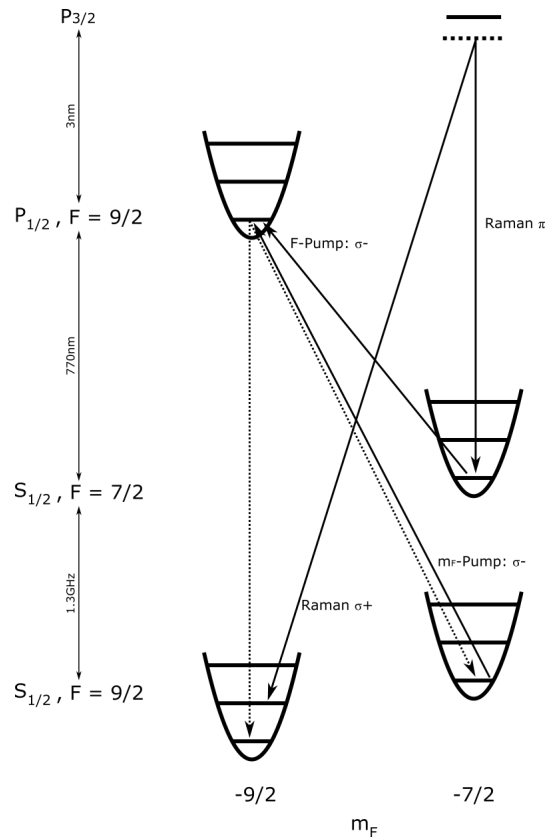


Figure 5.26: Raman laser and level scheme. The motional quantum number is reduced by a coherent two-photon transition. Afterwards the atom is pumped back to the initial state. The scattered pumping photons are unlikely to change the motional state.

the states for infinite times without any heating. Practically, there is a small probability for heating during each cycle because of resonant scattering on the D2 line. While driving the Raman transition, a pumping beam drives the transition

$$|{}^2S_{1/2}, F = 7/2, m_F = -7/2, n - 1\rangle \rightarrow |{}^2P_{1/2}, F = 9/2, m_F = -9/2, n - 1\rangle$$

from where the atom can decay to the ground state. Decay is also allowed to the incorrect m_F -state $|-7/2\rangle$, from where it is repumped with m_F -pump light. These pump transitions are unlikely to change the motional state in the Lamb-Dicke regime. Of course, one has to carefully tune the intensities of the pumping beams: If the intensities are too low, the atoms cycle on the two-photon transition longer than necessary. This reduces the cooling rate and additionally promotes heating by resonant scattering. If the pump intensities are too high, the pumping lasers themselves heat due to resonant scattering. Prior to actually use these techniques for RSC and optimizing all parameters to a level where high-fidelity ground-state cooling is achieved, preparational steps include recording a Raman spectrum - which is a very clear method for measuring trap frequencies - and measuring the transition rate of the two-photon process.

Currently, we use the Raman system - for optimization purposes - in two different ways:

- Shine in Raman as well as pump beams with adequate intensities and collect the D1 pump photons scattered in this process. One observes a Raman spectrum in the fluorescence signal.
- Shine in only Raman light. This drives a fraction of the atoms to $|{}^2S_{1/2}, F = 7/2\rangle$. Then, we use the blowout technique already used for microwave spectra: The atoms that remained in $|{}^2S_{1/2}, F = 9/2\rangle$ are removed by shining in resonant D2 light, afterwards the $|{}^2S_{1/2}, F = 7/2\rangle$ atoms are imaged using D1 cooling and repumping light. This is particularly useful for measuring the two-photon Rabi frequency.

Despite the existence of many parameters for the four lasers involved, it was straight forward to record a sideband-resolving spectrum and to observe particle loss when driving the blue sideband. The only thing we ensured by calculation prior to searching for a Raman signal was that the estimated Raman Rabi rate is sufficiently high. The Rabi rate is given by

$$\Omega_R = \frac{\Omega_1 \Omega_2}{2\Delta}$$

where Ω_1 and Ω_2 are the single photon Rabi frequencies of the respective Raman beams (resonance assumed) and Δ is the global detuning of the Raman

beams from the D2 transition. In terms of the saturation parameter $s = I/I_{sat}$, the single photon Rabi frequency in the resonant case is given by

$$\Omega = \Gamma\sqrt{s/2}$$

with the natural linewidth Γ .

In our apparatus, the power in each Raman beam is a few mW. The resulting intensity in units of saturation is typically $s = 100$. The Raman beams are detuned from the D2 line by typically 50 GHz. This gives a Raman Rabi frequency of 18 kHz.

For practicing the use of the Raman process, we used only one of the lattice axes at a time. This gives a clearer spectrum, as the trap frequencies of the lattices are not necessarily equal. For imaging the D1 fluorescence, we used the high resolution microscope and evaluated a central part of the lattice.

On 03.05.18, we observed a first Raman spectrum by shining in the Raman beams as well as the pump beams for 50 ms while collecting the scattered pump photons. We used about 10 % of the pump light intensity used in previous experimental steps such as preparing the atoms for magnetic trapping. This immediately gave a clearly visible Raman spectrum at the expected center frequency with well separated sidebands. We observed - for the usual lattice power of 300 mW - the sideband maxima in a distance of 200 kHz from the center of the carrier transition. One of these first spectra is shown in Fig. 5.27 together with the number of atoms remaining after the Raman light application. As expected, driving the Raman process around the carrier transition or the blue sideband significantly reduces the remaining atom number. We were also able to observe a reduction in the amplitude of the red sideband with longer application times, indicating that a fraction of the atoms were cooled to the ground state. In late September 2018, we had not yet optimized the cooling with respect to ground-state occupation. But we did some quantitative measurements to show that the cooling mechanism is working.

Two of these early measurements are shown in Fig. 5.28. Here, we applied Raman light for 50 ms on the red sideband and afterwards took a Raman spectrum. The cooling light application reduces the amplitude of the red sideband compared to the blue sideband. According to [161], the ratio of the sideband amplitudes gives the mean occupation number

$$\langle n \rangle = \frac{A_R/A_B}{1 - \frac{A_R}{A_B}}$$

Another interesting parameter is the occupation probability of the ground state:

$$P_{gs} = 1 - \frac{A_R}{A_B}$$

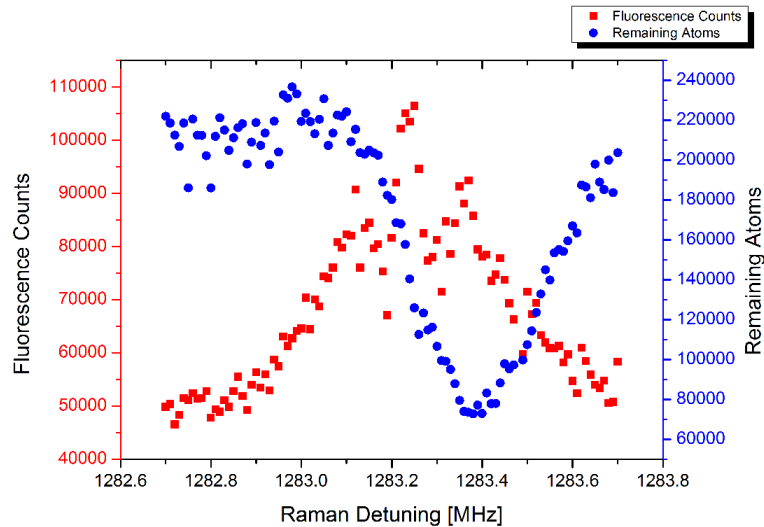


Figure 5.27: Spectrum of fluorescence photons collected during Raman light application and remaining atom number. Raman light with 75 GHz detuning was applied for 50 ms. The collected pump light fluorescence is drawn in red. The blue and the red sideband are about equal in amplitude and spaced the same distance from the carrier peak. In blue, the atom number remaining after the Raman light application is plotted. Around the blue sideband, we observe significant atom loss.

For the sample prior to Raman cooling, we obtained a mean occupation of $\langle n \rangle = 1.50$. This value is consistent with the temperature extracted from time-of-flight measurements where we determined a temperature of $T \approx 25 \mu\text{K}$. This would give a mean harmonic oscillator population of

$$\langle n \rangle = \frac{\exp\left(-\frac{\hbar\omega}{k_B T}\right)}{1 - \exp\left(-\frac{\hbar\omega}{k_B T}\right)} \approx 2$$

While observing the cooling process in a qualitative way was easy, it took some time to find the correct parameters for achieving a ground-state fraction close to unity.

An important step on the way to understand our Raman systems and to enhance its cooling performance was to measure the Raman rate. As noted above, one would expect this frequency¹³ to be on the 10 kHz scale. Due to the short coherence time of the process, it took us a while to actually observe the Rabi oscillation. We had to choose smaller global Raman detunings than the commonly used 50 GHz. With the standard setting, the Rabi oscillation is too slow to complete a cycle before the process decoheres. A plot with one full Rabi cycle is shown in Fig. 5.29. At about 22 GHz global Raman detuning, this gave a Rabi frequency of 29 kHz. This value is consistent with the

¹³Not an angular frequency!

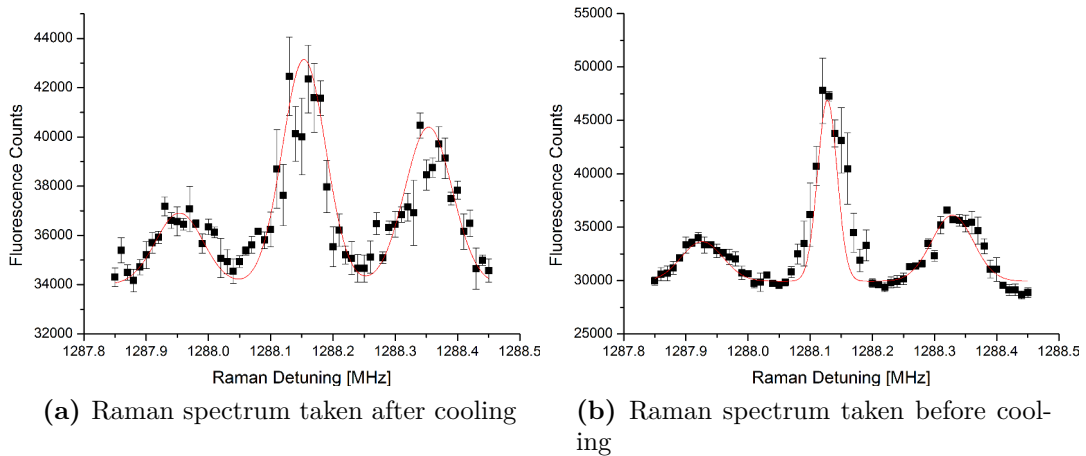


Figure 5.28: Raman spectra taken using the “blowout” technique with and without prior Raman light application on the red sideband. Some cooling effect can be detected: Without cooling, we derived a mean quantum number of $\langle n \rangle = 1.50$ ($P_{gs} = 40\%$), with cooling $\langle n \rangle = 0.84$ ($P_{gs} = 55\%$).

estimate given above, in particular as the actual laser beam intensities at the atom position are not known.

In late November 2018, after many minor improvements to the apparatus, we were finally able to observe a Raman cooling process that lead to a significant ground-state occupation. A Raman spectrum taken after cooling is shown in Fig. 5.30. Here, the ground state occupation is clearly much higher than in the previous spectra like the one shown in Fig. 5.28. We are not sure which of the changes we applied to the apparatus actually improved the cooling process, but we believe that the following played an important role:

- Adjustments on the Raman beams. In the first experiments, the illumination of the sample was not sufficiently homogeneous.
- Use detuned instead of resonant pump light. The 850 nm optical dipole traps are anticonfining for atoms in the $|P_{1/2}\rangle$ manifold. Detuned optical pumping leads to a mixing of $|S_{1/2}\rangle$ and $|P_{1/2}\rangle$ states. As explained in [114] this reduces the probability for an atom to get heated by anti-trapping.

In the Raman spectra presented here, the atoms are trapped in pancake traps produced by a single standing wave laser field. The Raman spectra were measured only along a single trap axis and the atoms cooled in 1D. A possible next step would be to extend this ground-state cooling scheme to atoms trapped in an optical lattice build from two, or three, standing waves. The required hardware is set up and working. Nevertheless, we want to achieve ground-state RSC in an optical tweezer first as we hope that a more homogeneous system might be better suited to gain more knowledge about the Raman system.

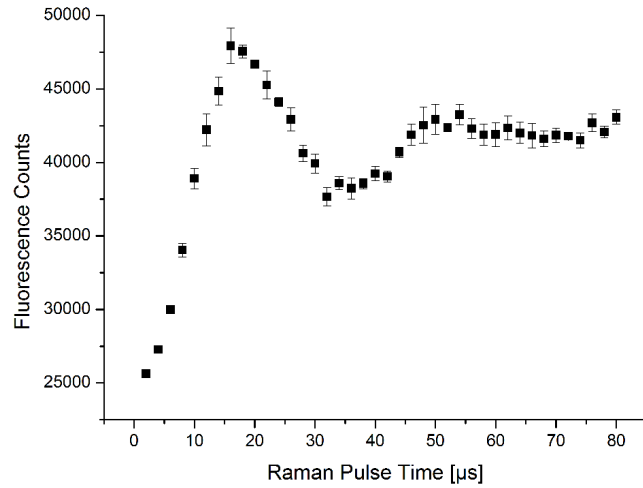


Figure 5.29: Damped Rabi oscillation of the two-photon transition. Recorded with a global Raman detuning of 22 GHz. The observed Rabi frequency of about 29 kHz is within the expected range. The cause of the fast decoherence is not clear at present.

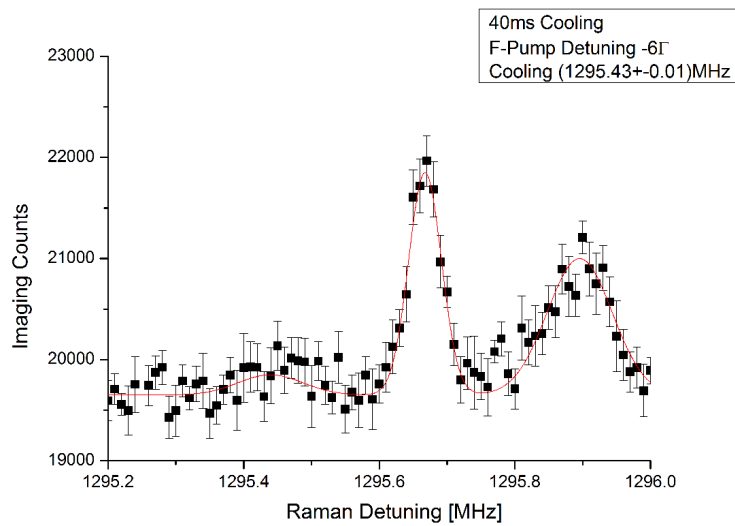


Figure 5.30: Raman spectrum recorded after 40 ms of cooling light application on the red sideband. The sideband is suppressed to a level, where its height can not be fitted reliably. The red line (fitted) suggests a ground state occupation of 85 %.

5.8 Atoms in the tweezer

Currently, we are able to load reliably a single atom into an optical tweezer using the D1 loading technique. The tweezer is occupied in about 50 % of the cases, which is exactly what one expects if a light-assisted collision process dominates atom loss: If the initial number of atoms in the tweezer is even, one ends up with an empty tweezer. If the initial number is odd, the last atom does not have a scattering partner and remains in the tweezer.

In the camera count histogram Fig. 5.31, one observes two peaks: The left one is always there and is produced by dark counts in the camera. The right one only occurs with atoms and is interpreted to be the fluorescence of a single atom. To produce this data, we illuminated the atoms with D1 light twice:

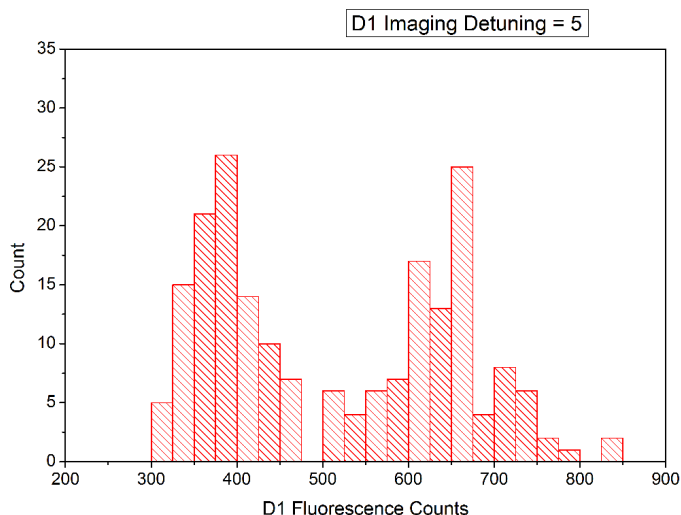


Figure 5.31: Histogram of camera counts in the tweezer region. The tweezer is occupied in about 50 % of the shots. Here, the atom was illuminated with usual D1 molasses light for detection, as we were not able to detect Raman fluorescence yet.

First to load the tweezer, then to check whether it is filled or not.

We have conducted attempts to increase the loading probability to above 50 % using a blue-shielding technique similar to [24]. As in December 2018, we have not found the correct parameters for sub-poissonian loading. When loading optical tweezers with a molasses technique, there is one technical complication: The interference pattern of the molasses beams exhibits drifts with respect to the tweezer position. To address this problem, we modulate the position of the retro-reflecting mirrors using piezos. This has been adopted from [14] and is - so far - only implemented for the horizontal molasses beams. Modifications to this modulation scheme might yield improved loading fidelity.

So far, we were not able to detect a Raman signal from the atom in the

tweezer. Unfortunately, this prevents me from presenting data on the tweezer's trap frequencies. Recording a tweezer Raman spectrum is one of the next important goals. With knowledge of the trap frequencies and the trap depth, we would have a cross check for the tweezers beam waist and the resolution of the microscope objective.

Chapter 6

Conclusions and Outlook

The physics of strongly correlated fermions in two-dimensional lattices is of crucial importance to understand high temperature superconductors. These materials are known for the appearance of unconventional electron pairing mechanisms that lead to anisotropic gap functions, e.g. the material YBCO featuring d-wave symmetry. The apparatus described and characterized in this thesis is designed to obtain a better understanding of these complex quantum systems by studying ultracold fermions in optical tweezers. The smallest system with d-wave symmetric states is the four-site plaquette. It can be regarded as the fundamental building block of d-wave superconductors. A main goal of our new quantum gas microscope is to investigate the nature of the four-site plaquette before extending the experiment to larger fermionic systems created by coupling several plaquettes.

The key component of the new apparatus is the high resolution microscope objective located inside the UHV chamber. As an important technical result, we demonstrated the technical feasibility of using complex, high-precision lens assemblies in a UHV environment. This simplifies optical alignment and might be used to build even more powerful quantum gas microscopes with less effort. The thesis provides detailed information on how we ensured UHV compatibility of the optical assembly. The other components such as vacuum systems, magnets and laser systems are designed to result in a versatile and extendable machine. The apparatus is prepared for experiments with optical tweezers and larger atom samples cooled to quantum degeneracy using all-optical cooling schemes.

In the course of commissioning the machine, we have shown that it can produce sufficiently large, sub-Doppler cooled, optically-confined samples of ^{40}K . In a one-dimensional optical lattice, we have realized a large ground-state occupation using Raman sideband cooling. With an optical tweezer, we are able to trap a single atom and to detect its fluorescence. All components work very reliably. The machine is capable of performing the experiment for several

thousand sequences without error. There are many additional components in the machine that are important for reliability and operational safety like the interlock system, the hard- and software for controlling the experiment, the RF sources and amplifiers, the 2D-MOT heating electronics, the cooling water supply and the air conditioning. These components are not considered in this thesis. Figure 6.1 serves as an illustration of the status at the end of my work.

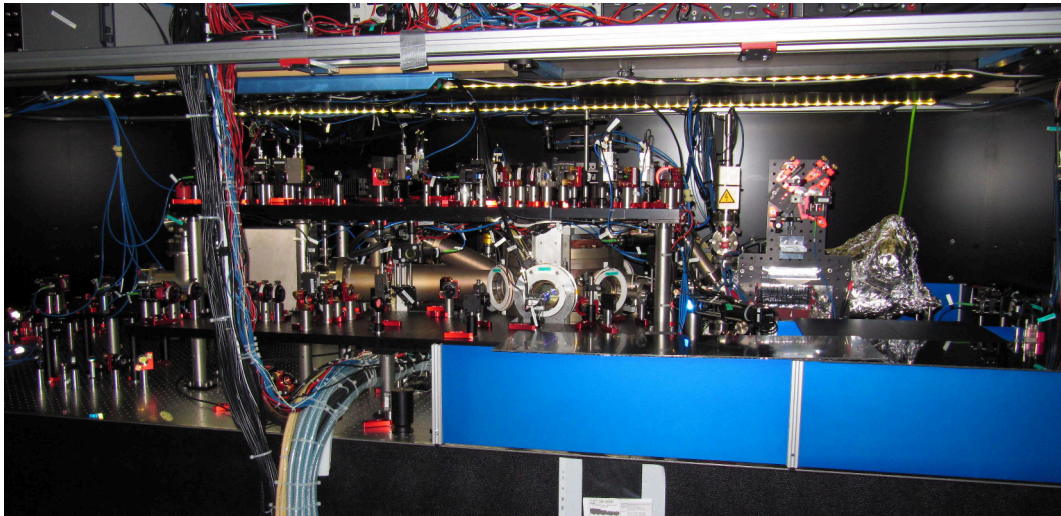


Figure 6.1: The apparatus in December 2018. From left to right: Pumping section, main chamber, 2D-MOT atom source. The vacuum chamber is surrounded by magnet coils, optical breadboards and optics. The optical table is equipped with a laminar flow box to provide thermal stability and a housing for laser safety and improved isolation.

The next milestone is to measure a Raman spectrum of a single atom and to cool it to the ground state. In combination with a measurement of the light shift, the trap frequencies obtained from Raman spectra could be used to determine the actual resolution of the imaging system. Afterwards, we will feed four tweezers into the microscope objective to form a four-site plaquette. The optics for this was prepared during A. Mozdzen’s master’s thesis [162] and uses four separate laser beams. This approach provides full control over all parameters of each tweezer but it relies on highly stable optomechanics to ensure that the spacing of the tweezers does not change. By adding optical modulators to one or more of these tweezers, the configuration could be extended to more complex tweezer arrangements. As soon as experiments with more than a single tweezer are performed, it will be essential to measure tunneling rates with a single atom before preparing states with more atoms. To prepare these more complex states, it would be useful to have a method for achieving a higher loading probability for the individual tweezers. As the application of atom sorting is not planned, enhancing the loading probability with a “blue shielding” mechanism will be required. So far, this has not been demonstrated with ^{40}K . The fidelity of ground-state cooling could be investigated with a

spin-polarized pair of atoms in a double-well.

On the longer term it would be fascinating to perform experiments in plaquettes as outlined in 2.3.4. The observation of the spatial formation of hole-pairs expected in the pseudogap regime would be particularly attractive because it does not rely on probing momentum. As soon as we are able to do single-atom sensitive imaging after time-of-flight expansion, it would be interesting to study momentum correlations on a single plaquette. By this, we might be able to verify the symmetries of the calculated ground states of the four-site plaquette for different fillings.

Nomenclature

- AL Aspheric lens, page 29
- AOM Acousto-optic modulator, page 80
- BCS Bardeen-Cooper-Schrieffer (theory), page 6
- BEC Bose–Einstein condensate, page 9
- CTE Coefficient of thermal expansion, page 75
- DDS Direct digital synthesizer, page 87
- DOF Depth of field, page 30
- DW Design wavelength, page 33
- ECDL External cavity diode laser, page 78
- EFL Effective focal length, page 29
- EIT Electromagnetically-induced transparency, page 32
- FOV Field of view, page 30
- IF Interference filter, page 79
- MOPA Master oscillator power amplifier, page 78
- MOT Magneto-optical trap, page 38
- NA Numerical aperture, page 28
- NMR Nuclear magnetic resonance, page 4
- PBS Polarizing beamsplitter, page 89
- PGC Polarization gradient cooling, page 31
- PSF Point spread function, page 29

QUIC Quadrupole-Ioffe configuration, page 60

RMS Root mean square, page 30

RSC Raman sideband-cooling, page 31

RVB Resonating valence bond, page 9

SIL Solid-immersion lens, page 29

SQUID Superconducting quantum interference device, page 4

TA Tapered amplifier, page 78

TML Total mass-loss, page 75

TSP Titanium sublimation pump, page 41

UHV Ultra-high vacuum, page 36

UV Ultraviolet, page 99

YBCO Yttrium barium copper oxide, page 9

Bibliography

- [1] R. P. Feynman, “Simulating physics with computers”, *Int. J. Theor. Phys.*, 21, 6-7, 467–488, 1982.
- [2] I. Bloch, J. Dalibard, and W. Zwerger, “Many-body physics with ultracold gases”, *Rev. Mod. Phys.*, 80, 3, 885, 2008.
- [3] J. I. Cirac and P. Zoller, “Goals and opportunities in quantum simulation”, *Nat. Phys.*, 8, 4, 264, 2012.
- [4] I. Bloch, J. Dalibard, and S. Nascimbene, “Quantum simulations with ultracold quantum gases”, *Nat. Phys.*, 8, 4, 267, 2012.
- [5] R. Blatt and C. F. Roos, “Quantum simulations with trapped ions”, *Nat. Phys.*, 8, 4, 277, 2012.
- [6] I. Georgescu, S. Ashhab, and F. Nori, “Quantum simulation”, *Rev. Mod. Phys.*, 86, 1, 153, 2014.
- [7] C. Gross and I. Bloch, “Quantum simulations with ultracold atoms in optical lattices”, *Science*, 357, 6355, 995–1001, 2017.
- [8] W. Ketterle and M. W. Zwierlein, “Making, probing and understanding ultracold fermi gases”, *Preprint arXiv:0801.2500*, 2008.
- [9] L. W. Cheuk, M. A. Nichols, M. Okan, T. Gersdorf, V. V. Ramasesh, W. S. Bakr, T. Lompe, and M. W. Zwierlein, “Quantum-gas microscope for fermionic atoms”, *Phys. Rev. Lett.*, 114, 19, 193001, 2015.
- [10] M. F. Parsons, F. Huber, A. Mazurenko, C. S. Chiu, W. Setiawan, K. Wooley-Brown, S. Blatt, and M. Greiner, “Site-resolved imaging of fermionic ${}^6\text{Li}$ in an optical lattice”, *Phys. Rev. Lett.*, 114, 21, 213002, 2015.
- [11] E. Haller, J. Hudson, A. Kelly, D. A. Cotta, B. Peaudecerf, G. D. Bruce, and S. Kuhr, “Single-atom imaging of fermions in a quantum-gas microscope”, *Nat. Phys.*, 11, 9, 738, 2015.

- [12] G. Edge, R. Anderson, D. Jervis, D. McKay, R. Day, S. Trotzky, and J. Thywissen, “Imaging and addressing of individual fermionic atoms in an optical lattice”, *Phys. Rev. A*, 92, 6, 063406, 2015.
- [13] A. Omran, M. Boll, T. A. Hilker, K. Kleinlein, G. Salomon, I. Bloch, and C. Gross, “Microscopic observation of pauli blocking in degenerate fermionic lattice gases”, *Phys. Rev. Lett.*, 115, 26, 263001, 2015.
- [14] A. M. Kaufman, B. J. Lester, and C. A. Regal, “Cooling a single atom in an optical tweezer to its quantum ground state”, *Phys. Rev. X*, 2, 4, 041014, 2012.
- [15] B. J. Lester, A. M. Kaufman, and C. A. Regal, “Raman cooling imaging: Detecting single atoms near their ground state of motion”, *Phys. Rev. A*, 90, 1, 011804, 2014.
- [16] A. Kaufman, B. Lester, C. Reynolds, M. Wall, M. Foss-Feig, K. Hazzard, A. Rey, and C. Regal, “Two-particle quantum interference in tunnel-coupled optical tweezers”, *Science*, 345, 6194, 306–309, 2014.
- [17] B. J. Lester, N. Luick, A. M. Kaufman, C. M. Reynolds, and C. A. Regal, “Rapid production of uniformly filled arrays of neutral atoms”, *Phys. Rev. Lett.*, 115, 7, 073003, 2015.
- [18] A. Kaufman, B. Lester, M. Foss-Feig, M. Wall, A. Rey, and C. Regal, “Entangling two transportable neutral atoms via local spin exchange”, *Nature*, 527, 7577, 208, 2015.
- [19] A. Kaufman, *Laser cooling atoms to indistinguishability: Atomic Hong-Ou-Mandel interference and entanglement through spin exchange*. PhD thesis, University of Colorado, 2015.
- [20] J. D. Thompson, T. Tiecke, A. S. Zibrov, V. Vuletić, and M. D. Lukin, “Coherence and Raman sideband cooling of a single atom in an optical tweezer”, *Phys. Rev. Lett.*, 110, 13, 133001, 2013.
- [21] M. A. Norcia, A. W. Young, and A. M. Kaufman, “Microscopic control and detection of ultracold strontium in optical-tweezer arrays”, *Preprint arXiv:1810.06626*, 2018.
- [22] A. Cooper, J. P. Covey, I. S. Madjarov, S. G. Porsev, M. S. Safronova, and M. Endres, “Alkaline earth atoms in optical tweezers”, *Preprint arXiv:1810.06537*, 2018.
- [23] T. Grünzweig, A. Hilliard, M. McGovern, and M. Andersen, “Near-deterministic preparation of a single atom in an optical microtrap”, *Nat. Phys.*, 6, 12, 951, 2010.

- [24] M. Brown, T. Thiele, C. Kiehl, T.-W. Hsu, and C. Regal, “Scaling atom array assembly with grey molasses”, *Preprint arXiv:1811.01448*, 2018.
- [25] M. Endres, H. Bernien, A. Keesling, H. Levine, E. R. Anschuetz, A. Krajenbrink, C. Senko, V. Vuletić, M. Greiner, and M. D. Lukin, “Atom-by-atom assembly of defect-free one-dimensional cold atom arrays”, *Science*, aah3752, 2016.
- [26] D. Barredo, S. De Léséleuc, V. Lienhard, T. Lahaye, and A. Browaeys, “An atom-by-atom assembler of defect-free arbitrary 2d atomic arrays”, *Science*, aah3778, 2016.
- [27] S. Stellmer, B. Pasquiou, R. Grimm, and F. Schreck, “Laser cooling to quantum degeneracy”, *Phys. Rev. Lett.*, 110, 26, 263003, 2013.
- [28] J. Hu, A. Urvoy, Z. Vendeiro, V. Crépel, W. Chen, and V. Vuletić, “Creation of a bose-condensed gas of ^{87}Rb by laser cooling”, *Science*, 358, 6366, 1078–1080, 2017.
- [29] F. Bloch, “Nuclear induction”, *Phys. Rev.*, 70, 7-8, 460, 1946.
- [30] P. Mansfield and I. Pykett, “Biological and medical imaging by NMR”, *Journal of Magnetic Resonance*, 29, 2, 355–373, 1978.
- [31] T. F. Budinger and P. C. Lauterbur, “Nuclear magnetic resonance technology for medical studies”, *Science*, 226, 4672, 288–298, 1984.
- [32] L. Evans and P. Bryant, “LHC machine”, *J. Instrum.*, 3, 08, S08001, 2008.
- [33] N. Mitchell, D. Bessette, R. Gallix, C. Jong, J. Knaster, P. Libeyre, C. Sborchia, and F. Simon, “The ITER magnet system”, *IEEE Transactions on applied superconductivity*, 18, 2, 435–440, 2008.
- [34] N. E. Booth and D. J. Goldie, “Superconducting particle detectors”, *Superconductor Science and Technology*, 9, 7, 493, 1996.
- [35] A. Silver and J. Zimmerman, “Quantum states and transitions in weakly connected superconducting rings”, *Phys. Rev.*, 157, 2, 317, 1967.
- [36] B. S. Deaver Jr and W. S. Goree, “Some techniques for sensitive magnetic measurements using superconducting circuits and magnetic shields”, *Rev. Sci. Instrum.*, 38, 3, 311–318, 1967.
- [37] R. Webb, R. P. Giffard, and J. Wheatley, “Noise thermometry at ultralow temperatures”, *J. Low Temp. Phys.*, 13, 3-4, 383–429, 1973.

- [38] R. W. Simon, R. B. Hammond, S. J. Berkowitz, and B. A. Willemsen, “Superconducting microwave filter systems for cellular telephone base stations”, *Proc. IEEE*, 92, 10, 1585–1596, 2004.
- [39] M. Stemmler, F. Merschel, M. Noe, and A. Hobl, “AmpaCity-Installation of advanced superconducting 10 kV system in city center replaces conventional 110 kV cables”, in *Applied Superconductivity and Electromagnetic Devices*, 323–326, IEEE, 2013.
- [40] J. G. Bednorz and K. A. Müller, “Possible high T_c superconductivity in the Ba-La-Cu-O system”, *Zeitschrift für Physik B*, 64, 2, 189–193, 1986.
- [41] M.-K. Wu, J. R. Ashburn, C. Torng, P. H. Hor, R. L. Meng, L. Gao, Z. J. Huang, Y. Wang, and a. Chu, “Superconductivity at 93 K in a new mixed-phase Y-Ba-Cu-O compound system at ambient pressure”, *Phys. Rev. Lett.*, 58, 9, 908, 1987.
- [42] J. Bardeen, L. Cooper, and J. Schrieffer, “Theory of superconductivity”, *Phys. Rev.*, 108, 1175, 1957.
- [43] D. Estève, J. M. Martinis, C. Urbina, M. Devoret, G. Collin, P. Monod, M. Ribault, and A. Revcolevschi, “Observation of the AC Josephson effect inside copper-oxide-based superconductors”, *EPL*, 3, 11, 1237, 1987.
- [44] P. Gammel, D. Bishop, G. Dolan, G. Kwo, C. Murray, L. Schneemeyer, and J. Waszczak, “Observation of hexagonally correlated flux quanta in $YBa_2Cu_3O_7$ ”, *Phys. Rev. Lett.*, 59, 2592, 1987.
- [45] I. Giaever, “Energy gap in superconductors measured by electron tunneling”, *Phys. Rev. Lett.*, 5, 147, 1960.
- [46] M. W. Zwierlein, *High-temperature superfluidity in an ultracold Fermi gas*. PhD thesis, Massachusetts Institute of Technology, 2006.
- [47] H. Hosono and K. Kuroki, “Iron-based superconductors: Current status of materials and pairing mechanism”, *Physica C: Superconductivity and its Applications*, 514, 399–422, 2015.
- [48] W. T. Grandy Jr, *Foundations of statistical mechanics: Equilibrium theory*, 19. Springer Science & Business Media, 2012.
- [49] S. Jochim, M. Bartenstein, A. Altmeyer, G. Hendl, S. Riedl, C. Chin, J. H. Denschlag, and R. Grimm, “Bose-Einstein condensation of molecules”, *Science*, 302, 5653, 2101–2103, 2003.

- [50] C. Regal, M. Greiner, and D. S. Jin, “Observation of resonance condensation of fermionic atom pairs”, *Phys. Rev. Lett.*, 92, 4, 040403, 2004.
- [51] M. Bartenstein, A. Altmeyer, S. Riedl, S. Jochim, C. Chin, J. H. Denschlag, and R. Grimm, “Crossover from a molecular Bose-Einstein condensate to a degenerate Fermi gas”, *Phys. Rev. Lett.*, 92, 12, 120401, 2004.
- [52] M. Zwierlein, C. Stan, C. Schunck, S. Raupach, A. Kerman, and W. Ketterle, “Condensation of pairs of fermionic atoms near a Feshbach resonance”, *Phys. Rev. Lett.*, 92, 12, 120403, 2004.
- [53] C. Chin, M. Bartenstein, A. Altmeyer, S. Riedl, S. Jochim, J. H. Denschlag, and R. Grimm, “Observation of the pairing gap in a strongly interacting Fermi gas”, *Science*, 305, 5687, 1128–1130, 2004.
- [54] J. Stewart, J. Gaebler, and D. Jin, “Using photoemission spectroscopy to probe a strongly interacting Fermi gas”, *Nature*, 454, 7205, 744, 2008.
- [55] M. W. Zwierlein, A. Schirotzek, C. H. Schunck, and W. Ketterle, “Fermionic superfluidity with imbalanced spin populations”, *Science*, 311, 5760, 492–496, 2006.
- [56] G. B. Partridge, W. Li, R. I. Kamar, Y.-A. Liao, and R. G. Hulet, “Pairing and phase separation in a polarized Fermi gas”, *Science*, 311, 5760, 503–505, 2006.
- [57] P. W. Anderson, “The resonating valence bond state in La_2CuO_4 and superconductivity”, *Science*, 235, 4793, 1196–1198, 1987.
- [58] G. Baskaran, Z. Zou, and P. Anderson, “The resonating valence bond state and high- T_c superconductivity”, *Solid State Commun.*, 63, 11, 973–976, 1987.
- [59] N. Plakida, V. Y. Yushankhai, and I. Stasyuk, “On d-wave pairing in one band Hubbard model”, *Physica C*, 162, 787–788, 1989.
- [60] D. Scalapino, E. Loh Jr, and J. Hirsch, “D-wave pairing near a spin-density-wave instability”, *Phys. Rev. B*, 34, 11, 8190, 1986.
- [61] D. Scalapino, E. Loh Jr, and J. Hirsch, “Fermi-surface instabilities and superconducting d-wave pairing”, *Phys. Rev. B*, 35, 13, 6694, 1987.
- [62] M. Harland, M. I. Katsnelson, and A. I. Lichtenstein, “Plaquette valence bond theory of high-temperature superconductivity”, *Phys. Rev. B*, 94, 12, 125133, 2016.

- [63] D. J. Scalapino, “A common thread: The pairing interaction for unconventional superconductors”, *Rev. Mod. Phys.*, 84, 4, 1383, 2012.
- [64] M. Norman and C. Pepin, “The electronic nature of high temperature cuprate superconductors”, *Rep. Prog. Phys.*, 66, 10, 1547, 2003.
- [65] C. Tsuei and J. Kirtley, “Pairing symmetry in cuprate superconductors”, *Rev. Mod. Phys.*, 72, 4, 969, 2000.
- [66] D. J. Scalapino, “The case for $d_{x^2-y^2}$ pairing in the cuprate superconductors”, *Phys. Rep.*, 250, 6, 329–365, 1995.
- [67] P. W. Anderson, “Personal history of my engagement with cuprate superconductivity”, *Int. J. Mod. Phys. B*, 25, 01, 1–39, 2011.
- [68] F. Zhang and T. Rice, “Effective hamiltonian for the superconducting Cu oxides”, *Phys. Rev. B*, 37, 7, 3759, 1988.
- [69] J. Hubbard, “Electron correlations in narrow energy bands”, *Proc. R. Soc. Lond. A*, 276, 1365, 238–257, 1963.
- [70] M. Köhl, H. Moritz, T. Stöferle, K. Günter, and T. Esslinger, “Fermionic atoms in a three dimensional optical lattice: Observing Fermi surfaces, dynamics, and interactions”, *Phys. Rev. Lett.*, 94, 8, 080403, 2005.
- [71] R. Jördens, N. Strohmaier, K. Günter, H. Moritz, and T. Esslinger, “A Mott insulator of fermionic atoms in an optical lattice”, *Nature*, 455, 7210, 204, 2008.
- [72] U. Schneider, L. Hackermüller, S. Will, T. Best, I. Bloch, T. Costi, R. Helmes, D. Rasch, and A. Rosch, “Metallic and insulating phases of repulsively interacting fermions in a 3D optical lattice”, *Science*, 322, 5907, 1520–1525, 2008.
- [73] D. Greif, M. F. Parsons, A. Mazurenko, C. S. Chiu, S. Blatt, F. Huber, G. Ji, and M. Greiner, “Site-resolved imaging of a fermionic Mott insulator”, *Science*, 351, 6276, 953–957, 2016.
- [74] A. Mazurenko, C. S. Chiu, G. Ji, M. F. Parsons, M. Kanász-Nagy, R. Schmidt, F. Grusdt, E. Demler, D. Greif, and M. Greiner, “A cold-atom Fermi-Hubbard antiferromagnet”, *Nature*, 545, 7655, 462, 2017.
- [75] K. Chao, J. Spałek, and A. Oles, “Kinetic exchange interaction in a narrow s-band”, *J. Phys. C*, 10, 10, L271, 1977.
- [76] J. Spałek, “tJ model then and now: a personal perspective from the pioneering times”, *Preprint arXiv:0706.4236*, 2007.

- [77] P. W. Anderson, “Resonating valence bonds: A new kind of insulator?”, *Materials Research Bulletin*, 8, 2, 153–160, 1973.
- [78] P. W. Anderson, P. Lee, M. Randeria, T. Rice, N. Trivedi, and F. Zhang, “The physics behind high-temperature superconducting cuprates: the plain vanilla version of RVB”, *J. Phys. Condens. Matter*, 16, 24, R755, 2004.
- [79] G. Kotliar, “Resonating valence bonds and d-wave superconductivity”, *Phys. Rev. B*, 37, 7, 3664, 1988.
- [80] G. Kotliar and J. Liu, “Superexchange mechanism and d-wave superconductivity”, *Phys. Rev. B*, 38, 7, 5142, 1988.
- [81] Y. Kitaoka, S. Hiramatsu, T. Kondo, and K. Asayama, “Nuclear relaxation and Knight shift studies of copper in $YBa_2Cu_3O_{7-y}$ ”, *J. Phys. Soc. Jpn.*, 57, 1, 30–33, 1988.
- [82] S. Barrett, D. Durand, C. Pennington, C. Slichter, T. Friedmann, J. Rice, and D. Ginsberg, “ ^{63}Cu knight shifts in the superconducting state of $YBa_2Cu_3O_{7-\delta}$ ($T_c = 90\text{K}$)”, *Phys. Rev. B*, 41, 10, 6283, 1990.
- [83] M. Takigawa, A. Reyes, P. Hammel, J. Thompson, R. Heffner, Z. Fisk, and K. Ott, “Cu and O NMR studies of the magnetic properties of $YBa_2Cu_3O_{6.63}$ ($T_c=62\text{K}$)”, *Phys. Rev. B*, 43, 1, 247, 1991.
- [84] K. A. Kuns, A. M. Rey, and A. V. Gorshkov, “d-wave superfluidity in optical lattices of ultracold polar molecules”, *Phys. Rev. A*, 84, 6, 063639, 2011.
- [85] O. Dutta, M. Gajda, P. Hauke, M. Lewenstein, D.-S. Lühmann, B. A. Malomed, T. Sowiński, and J. Zakrzewski, “Non-standard hubbard models in optical lattices: a review”, *Reports on Progress in Physics*, 78, 6, 066001, 2015.
- [86] T. Timusk and B. Statt, “The pseudogap in high-temperature superconductors: an experimental survey”, *Rep. Prog. Phys.*, 62, 61, 1999.
- [87] M. Vershinin, S. Misra, S. Ono, Y. Abe, Y. Ando, and A. Yazdani, “Local ordering in the pseudogap state of the high- T_c superconductor $Bi_2Sr_2CaCu_2O_{8+\delta}$ ”, *Science*, 303, 1995, 2004.
- [88] H.-D. Chen, O. Vafek, A. Yazdani, and S.-C. Zhang, “Pair density wave in the pseudogap state of high temperature superconductors”, *Phys. Rev. Lett.*, 93, 18, 187002, 2004.

- [89] E. Altman, E. Demler, and M. D. Lukin, “Probing many-body states of ultracold atoms via noise correlations”, *Phys. Rev. A*, 70, 1, 013603, 2004.
- [90] M. Greiner, C. Regal, J. Stewart, and D. Jin, “Probing pair-correlated fermionic atoms through correlations in atom shot noise”, *Phys. Rev. Lett.*, 94, 11, 110401, 2005.
- [91] P. M. Preiss, J. H. Becher, R. Klemt, V. Klinkhamer, A. Bergschneider, and S. Jochim, “High-contrast interference of ultracold fermions”, *Preprint arXiv:1811.12939*, 2018.
- [92] Z. Shen, D. Dessau, B. Wells, D. King, W. Spicer, A. Arko, D. Marshall, A. Lombardo, A. Kapitulnik, P. Dickinson, S. Doniach, J. DiCarlo, T. Loeser, and C. Park, “Anomalously large gap anisotropy in the a-b plane of $Bi_2Sr_2CaCu_2O_{8+\delta}$ ”, *Phys. Rev. Lett.*, 70, 1553, 1993.
- [93] H. Ding, M. Norman, J. Campuzano, M. Randeria, A. Bellman, T. Yokoya, T. Takahashi, T. Mochiku, and K. Kadowaki, “Angle-resolved photoemission spectroscopy study of the superconducting gap anisotropy in $Bi_2Sr_2CaCu_2O_{8+x}$ ”, *Phys. Rev. B*, 54, 14, R9678, 1996.
- [94] D. Van Harlingen, “Phase-sensitive tests of the symmetry of the pairing state in the high-temperature superconductors”, *Rev. Mod. Phys.*, 67, 2, 515, 1995.
- [95] D. Wollman, D. Van Harlingen, W. Lee, D. Ginsberg, and A. Leggett, “Experimental determination of the superconducting pairing state in YBCO from the phase coherence of YBCO-Pb dc SQUIDS”, *Phys. Rev. Lett.*, 71, 13, 2134, 1993.
- [96] M. Sgrist and T. M. Rice, “Paramagnetic effect in high T_c superconductors - a hint for d-wave superconductivity”, *J. Phys. Soc. Jpn.*, 61, 12, 4283–4286, 1992.
- [97] B. D. Josephson, “Possible new effects in superconductive tunnelling”, *Phys. Lett.*, 1, 7, 251–253, 1962.
- [98] P. W. Anderson and J. M. Rowell, “Probable observation of the Josephson superconducting tunneling effect”, *Phys. Rev. Lett.*, 10, 6, 230, 1963.
- [99] I. Giaever, “Electron tunneling between two superconductors”, *Phys. Rev. Lett.*, 5, 10, 464, 1960.
- [100] B. D. Josephson, “The discovery of tunnelling supercurrents - Nobel Lecture, 12 December 1973”, *Europhysics News*, 5, 3, 1–5, 1974.

- [101] I. Giaever, “Electron tunneling and superconductivity”, *Rev. Mod. Phys.*, 46, 2, 245, 1974.
- [102] Y. Aharonov and D. Bohm, “Significance of electromagnetic potentials in the quantum theory”, *Phys. Rev.*, 115, 3, 485, 1959.
- [103] C. Tsuei, J. R. Kirtley, C. Chi, L. S. Yu-Jahnes, A. Gupta, T. Shaw, J. Sun, and M. Ketchen, “Pairing symmetry and flux quantization in a tricrystal superconducting ring of $YBa_2Cu_3O_{7-\delta}$ ”, *Phys. Rev. Lett.*, 73, 4, 593, 1994.
- [104] J. Kirtley, C. Tsuei, J. Sun, C. Chi, L. S. Yu-Jahnes, A. Gupta, M. Rupp, and M. Ketchen, “Symmetry of the order parameter in the high- T_c superconductor $YBa_2Cu_3O_{7-\delta}$ ”, *Nature*, 373, 6511, 225, 1995.
- [105] D. Scalapino, “Numerical studies of the 2D Hubbard model”, in *Handbook of High-Temperature Superconductivity*, 495–526, Springer, 2007.
- [106] A. Rey, R. Sensarma, S. Fölling, M. Greiner, E. Demler, and M. D. Lukin, “Controlled preparation and detection of d-wave superfluidity in two-dimensional optical superlattices”, *EPL*, 87, 6, 60001, 2009.
- [107] S. Nascimbène, Y.-A. Chen, M. Atala, M. Aidelsburger, S. Trotzky, B. Paredes, and I. Bloch, “Experimental realization of plaquette resonating valence-bond states with ultracold atoms in optical superlattices”, *Phys. Rev. Lett.*, 108, 20, 205301, 2012.
- [108] W. S. Bakr, J. I. Gillen, A. Peng, S. Fölling, and M. Greiner, “A quantum gas microscope for detecting single atoms in a Hubbard-regime optical lattice”, *Nature*, 462, 7269, 74, 2009.
- [109] W. S. Bakr, *Microscopic Studies of Quantum Phase Transitions in Optical Lattices*. Harvard University, 2011.
- [110] J. F. Sherson, C. Weitenberg, M. Endres, M. Cheneau, I. Bloch, and S. Kuhr, “Single-atom-resolved fluorescence imaging of an atomic Mott insulator”, *Nature*, 467, 7311, 68, 2010.
- [111] C. Weitenberg, *Single-atom resolved imaging and manipulation in an atomic Mott insulator*. PhD thesis, LMU, 2011.
- [112] M. Miranda, R. Inoue, Y. Okuyama, A. Nakamoto, and M. Kozuma, “Site-resolved imaging of ytterbium atoms in a two-dimensional optical lattice”, *Phys. Rev. A*, 91, 6, 063414, 2015.
- [113] M. S. Miranda, *Quantum gas microscope for ytterbium atoms*. PhD thesis, Tokyo Institute of Technology, 2016.

- [114] L. W. Cheuk, *Quantum gas microscopy of strongly correlated fermions*. PhD thesis, Massachusetts Institute of Technology, 2017.
- [115] D. A. Cotta, *A single-site resolution fermionic quantum-gas microscope*. PhD thesis, University of Strathclyde, 2018.
- [116] G. Edge, *Imaging Fermionic Atoms in a Quantum Gas Microscope*. PhD thesis, University of Toronto, 2017.
- [117] A. Omran, *A microscope for Fermi gases*. PhD thesis, LMU, 2016.
- [118] R. Yamamoto, J. Kobayashi, T. Kuno, K. Kato, and Y. Takahashi, “An ytterbium quantum gas microscope with narrow-line laser cooling”, *N. J. Phys.*, 18, 2, 023016, 2016.
- [119] R. Yamamoto, *A Quantum Gas Microscope of Two-electron Atoms with Fluorescence and Faraday Imaging*. PhD thesis, Kyoto University, 2016.
- [120] C. Robens, S. Brakhane, W. Alt, F. Kleiβler, D. Meschede, G. Moon, G. Ramola, and A. Alberti, “High numerical aperture (NA=0.92) objective lens for imaging and addressing of cold atoms”, *Opt. Lett.*, 42, 6, 1043–1046, 2017.
- [121] C. Robens, “Testing the quantumness of atom trajectories”, 2017.
- [122] S. Murmann, A. Bergschneider, V. M. Klinkhamer, G. Zürn, T. Lompe, and S. Jochim, “Two fermions in a double well: Exploring a fundamental building block of the hubbard model”, *Phys. Rev. Lett.*, 114, 8, 080402, 2015.
- [123] F. Serwane, G. Zürn, T. Lompe, T. Ottenstein, A. Wenz, and S. Jochim, “Deterministic preparation of a tunable few-fermion system”, *Science*, 332, 6027, 336–338, 2011.
- [124] S. Murmann, *Few-particle quantum magnetism with ultracold atoms*. PhD thesis, Ruperto-Carola-University of Heidelberg, 2015.
- [125] J. D. Thompson, T. Tiecke, N. P. de Leon, J. Feist, A. Akimov, M. Gullans, A. S. Zibrov, V. Vuletić, and M. D. Lukin, “Coupling a single trapped atom to a nanoscale optical cavity”, *Science*, 340, 6137, 1202–1205, 2013.
- [126] P. Sompet, Y. H. Fung, E. Schwartz, M. D. Hunter, J. Phrompao, and M. F. Andersen, “Zeeman-insensitive cooling of a single atom to its two-dimensional motional ground state in tightly focused optical tweezers”, *Phys. Rev. A*, 95, 3, 031403, 2017.

- [127] D. Frese, B. Ueberholz, S. Kuhr, W. Alt, D. Schrader, V. Gomer, and D. Meschede, “Single atoms in an optical dipole trap: Towards a deterministic source of cold atoms”, *Phys. Rev. Lett.*, 85, 18, 3777, 2000.
- [128] N. Schlosser, G. Reymond, I. Protsenko, and P. Grangier, “Subpoissonian loading of single atoms in a microscopic dipole trap”, *Nature*, 411, 6841, 1024, 2001.
- [129] N. Schlosser, G. Reymond, and P. Grangier, “Collisional blockade in microscopic optical dipole traps”, *Phys. Rev. Lett.*, 89, 2, 023005, 2002.
- [130] G. Reymond, N. Schlosser, I. Protsenko, and P. Grangier, “Single-atom manipulations in a microscopic dipole trap”, *Philos. Trans. Royal Soc. A*, 361, 1808, 1527–1536, 2003.
- [131] N. Schlosser, *Etude et réalisation de micro-pièges dipolaires optiques pour atomes neutres*. PhD thesis, Université Paris Sud-Paris XI, 2001.
- [132] T. Grünzweig, M. McGovern, A. J. Hilliard, and M. F. Andersen, “Using light-assisted collisions to consistently isolate individual atoms for quantum information processing”, *Quantum Inf. Process.*, 10, 6, 925, 2011.
- [133] M. McGovern, A. J. Hilliard, T. Grünzweig, and M. F. Andersen, “Counting atoms in a deep optical microtrap”, *Opt. Lett.*, 36, 7, 1041–1043, 2011.
- [134] A. Hilliard, Y. Fung, P. Sompet, A. Carpentier, and M. Andersen, “In-trap fluorescence detection of atoms in a microscopic dipole trap”, *Phys. Rev. A*, 91, 5, 053414, 2015.
- [135] T. Uehlinger, *A 2D Magneto-Optical Trap as a High-Flux Source of Cold Potassium Atoms*. Diploma thesis, Swiss Federal Institute of Technology Zurich, 2008.
- [136] B. Shirinzadeh and C. C. Wang, “Accurate determination of the vapor pressure of potassium using optical absorption”, *Appl. Opt.*, 22, 20, 3265–3270, 1983.
- [137] B. Zimmermann, *Microscopy of ultra-cold fermionic lithium*. PhD thesis, ETH Zurich, 2010.
- [138] W. Weimer, *Probing superfluid properties in strongly correlated Fermi gases with high spatial resolution*. PhD thesis, Universität Hamburg, 2014.

- [139] M. A. A. Mamun, A. A. Elmustafa, M. L. Stutzman, P. A. Adderley, and M. Poelker, “Effect of heat treatments and coatings on the outgassing rate of stainless steel chambers”, *Journal of Vacuum Science & Technology A*, 32, 2, 021604, 2014.
- [140] T. G. Petelski, *Atom interferometers for precision gravity measurements*. PhD thesis, Paris 6, 2005.
- [141] R. Vollmer, *Aufbau und Charakterisierung eines RF-Setups zur Spinmanipulation ultrakalter Quantengase*. Bachelor’s thesis, Universität Hamburg, 2016.
- [142] B. DeMarco, *Quantum behavior of an atomic Fermi gas*. PhD thesis, University of Colorado, 2001.
- [143] C. Darsow-Fromm, *Laserkühlung von ^{39}K und ^{40}K Atomen mit einer Kombination aus zwei- und dreidimensionaler magneto-optischer Falle*. Master’s thesis, Universität Hamburg, 2016.
- [144] M. Greiner, I. Bloch, T. W. Hänsch, and T. Esslinger, “Magnetic transport of trapped cold atoms over a large distance”, *Phys. Rev. A*, 63, 3, 031401, 2001.
- [145] H. Moritz, *One-dimensional atomic gases*. PhD thesis, ETH Zurich, 2006.
- [146] H. Lewandowski, D. Harber, D. Whitaker, and E. Cornell, “Simplified system for creating a Bose-Einstein condensate”, *J. Low Temp. Phys.*, 132, 309, 2003.
- [147] K. Nakagawa, Y. Suzuki, M. Horikoshi, and J. Kim, “Simple and efficient magnetic transport of cold atoms using moving coils for the production of Bose-Einstein condensation”, *Appl. Phys. B*, 81, 6, 791–794, 2005.
- [148] T. Esslinger, I. Bloch, and T. W. Hänsch, “Bose-Einstein condensation in a quadrupole-Ioffe-configuration trap”, *Phys. Rev. A*, 58, 4, R2664, 1998.
- [149] D. O. Sabulsky, C. V. Parker, N. D. Gemelke, and C. Chin, “Efficient continuous-duty bitter-type electromagnets for cold atom experiments”, *Rev. Sci. Instrum.*, 84, 10, 104706, 2013.
- [150] B. Höltekemeier, *2D MOT as a source of a cold atom target*. Diploma thesis, University of Heidelberg, 2011.
- [151] “Outgassing data for selecting spacecraft materials”. <https://outgassing.nasa.gov/>. Accessed: 2018-07-16.

- [152] L. Ricci, M. Weidemüller, T. Esslinger, A. Hemmerich, C. Zimmermann, V. Vuletić, W. König, and T. Hänsch, “A compact grating-stabilized diode laser system for atomic physics”, *Opt. Comm.*, 117, 5-6, 541–549, 1995.
- [153] J. Zander, *Aufbau eines Lasersystems zur Laserkühlung von fermionischen Kaliumatomen*. Master’s thesis, 2015.
- [154] K. Jarvis, J. Devlin, T. Wall, B. Sauer, and M. Tarbutt, “Blue-detuned magneto-optical trap”, *Phys. Rev. Lett.*, 120, 8, 083201, 2018.
- [155] R. Grimm, M. Weidemüller, and Y. B. Ovchinnikov, “Optical dipole traps for neutral atoms”, in *Advances in atomic, molecular, and optical physics*, 42, 95–170, Elsevier, 2000.
- [156] K. Hueck, N. Luick, L. Sobirey, J. Siegl, T. Lompe, H. Moritz, L. W. Clark, and C. Chin, “Calibrating high intensity absorption imaging of ultracold atoms”, *Opt. Express*, 25, 8, 8670–8679, 2017.
- [157] G. Salomon, L. Fouché, P. Wang, A. Aspect, P. Bouyer, and T. Bourdel, “Gray-molasses cooling of ^{39}K to a high phase-space density”, *EPL*, 104, 6, 63002, 2014.
- [158] C. Klempt, T. Van Zoest, T. Henninger, E. Rasel, W. Ertmer, J. Arlt, *et al.*, “Ultraviolet light-induced atom desorption for large rubidium and potassium magneto-optical traps”, *Phys. Rev. A*, 73, 1, 013410, 2006.
- [159] M. Tarnowski, *Implementation and Characterization of a Gray Molasses and of Tunable Hexagonal Optical Lattices for 40K*. PhD thesis, Universität Hamburg, 2015.
- [160] C. Regal and D. Jin, “Measurement of positive and negative scattering lengths in a fermi gas of atoms”, *Phys. Rev. Lett.*, 90, 23, 230404, 2003.
- [161] C. Monroe, D. Meekhof, B. King, S. R. Jefferts, W. M. Itano, D. J. Wineland, and P. Gould, “Resolved-sideband raman cooling of a bound atom to the 3D zero-point energy”, *Phys. Rev. Lett.*, 75, 22, 4011, 1995.
- [162] A. Mozdzen, *Entwicklung eines optischen Aufbaus zur Realisierung von kleinen Fermi-Hubbard Systemen*. Master’s thesis, Universität Hamburg, 2018.

Eidesstattliche Versicherung / Declaration on oath

Hiermit versichere ich an Eides statt, die vorliegende Dissertationsschrift selbst verfasst und keine anderen als die angegebenen Hilfsmittel und Quellen benutzt zu haben.

Die eingereichte schriftliche Fassung entspricht der auf dem elektronischen Speichermedium.

Die Dissertation wurde in der vorgelegten oder einer ähnlichen Form nicht schon einmal in einem früheren Promotionsverfahren angenommen oder als ungenügend beurteilt.

Hamburg, den 11.01.2019

Phillip Wieburg